Microwave plasma synthesis of graphene and its laser-optical in situ characterization

by
Stanislav Musikhin

A thesis
presented to the University of Waterloo
and the University of Duisburg-Essen
in fulfillment of the
thesis requirement for the degree of
Doctor of Philosophy
in
Mechanical and Mechatronics Engineering

Waterloo, Ontario, Canada/Duisburg, Germany, 2022

Examining committee membership

The following served on the Examining Committee for this thesis. The decision of the Examining Committee is by majority vote.

External examiner	Stefan Will Professor, Friedrich-Alexander-Universität Erlangen-Nürnberg
Supervisor	Christof Schulz Professor, University of Duisburg-Essen
Supervisor	Kyle J. Daun Professor, University of Waterloo
Internal member	Kevin Musselman Associate Professor, University of Waterloo
Internal member	Sebastian Kaiser Professor, University of Duisburg-Essen

Author’s declaration

This thesis consists of material all of which I authored or co-authored: see Statement of Contributions included in the thesis. This is a true copy of the thesis, including any required final revisions, as accepted by my examiners.

I understand that my thesis may be made electronically available to the public.

Statement of contributions

Stanislav Musikhin is the sole author of Chapters 1, 2, 7, and 8, which were written for this thesis and not for publication. The research results presented in Chapters 3-6 have been obtained at the University of Duisburg-Essen (UDE), University of Waterloo (UW), and the National Research Council Canada (NRC) in a collaborative effort and disseminated in four manuscripts written in co-authorship with colleagues. The original manuscripts have been edited for this monograph: Abstracts, acknowledgments, and funding sections were removed; references, figures, and results were rearranged to fit the logical reading sequence of this thesis; where necessary, text was expanded with additional detail or updated with new information that became available after the publication of original manuscripts; any repetitions among the manuscripts were removed.

In all chapters (manuscripts), unless stated otherwise, I conceptualized and conducted the study, analyzed the data, and wrote the draft manuscripts with further editing and submission. All co-authors participated in the study conceptualization, contributed to the interpretation of the results, reviewed, and edited the manuscripts.

Research presented in Chapter 3 was published and submitted for publication as:

- S. Musikhin, P. Fortugno, T. Endres, T. Dreier, K.J. Daun, C. Schulz, Elemental carbon concentration as the main factor in gas-phase graphene synthesis: Quantitative Fourier-transform infrared spectroscopy study, Carbon, submitted (2022);
- S. Musikhin, S. Talebi-Moghaddam, J.C. Corbin, G.J. Smallwood, C. Schulz, K.J. Daun, Crumpled few-layer graphene: Connection between morphology and optical properties, Carbon 182 (2021) 677–690.

Technical support was provided by a number of colleagues: TEM imaging was performed by C.-F. López Cámara and M. Heidelmann (both UDE), SEM imaging by X. Medvedeva (UW), XPS by A. Tarasov (UDE), Raman spectroscopy by P. Fortugno (UDE), and the tomographic TEM imaging was ordered at the Canadian Center for Electron Microscopy. The reactor blueprints were done by L. Jerig (UDE) in consultation with S. Musikhin.

Research presented in Chapter 4 was published as:

- S. Musikhin, S. Talebi-Moghaddam, J.C. Corbin, G.J. Smallwood, C. Schulz, K.J. Daun, Crumpled few-layer graphene: Connection between morphology and optical properties, Carbon 182 (2021) 677–690.

The RDG and DDA simulations were done by Dr. Talebi-Moghaddam (UW), who also drafted the corresponding section of the manuscript. Technical support in the aerosol equipment was provided from S.-A. Lussier, B. Smith, and D. Clavel (all NRC). M. Heidelmann (UDE) assisted in tomographic 3D reconstructions.

Research presented in Chapter 5 was published and submitted for publication as:

- S. Musikhin, P. Fortugno, J.C. Corbin, G.J. Smallwood, T. Dreier, K.J. Daun, C. Schulz, Characterization of few-layer graphene aerosols by laser-induced incandescence, Carbon 167 (2020) 870–880;
- C.-F. López Cámara, P. Fortugno, M. Asif, S. Musikhin, C. Prindler, H. Wiggers, T. Endres, N. Eaves, K.J. Daun, C. Schulz, Evolution of particle size and morphology in plasma synthesis of few-layer graphene and soot, Combustion and Flame, submitted (2022).

C.-F. López Cámara (UDE) was the lead author in the latter manuscript. I contributed to the study conceptualization, results interpretation, review, and editing of the manuscript. I analyzed the data on laser-induced incandescence and wrote the corresponding part of the manuscript, which was used in this chapter of the thesis. TEM sampling and imaging was done by C.-F. López Cámara and P. Fortugno (both UDE). BET measurements by B. Endres (UDE).

Research presented in Chapter 6 was submitted for publication as:

- S. Musikhin, P. Fortugno, T. Endres, T. Dreier, K.J. Daun, C. Schulz, Elemental carbon concentration as the main factor in gas-phase graphene synthesis: Quantitative Fourier-transform infrared spectroscopy study, Carbon, submitted (2022).

Consultations were provided by P. Fjodorow (UDE) on the HITRAN database and S. Peukert (UDE) on CHEMKIN-Pro software.

Abstract

Graphene and its derivatives possess exceptional electrical, mechanical, and thermal properties, which enable the use of these materials in numerous existing and emerging applications. Accordingly, large-scale graphene production is needed to fulfill the expected demand for this material. However, the current examples of graphene mass fabrication through top-down scalable approaches, e.g., liquid-phase exfoliation and chemical graphene oxide reduction, are incapable of consistently producing graphene at the quality levels needed to exploit its unique properties in applications.

Gas-phase microwave-assisted synthesis of free-standing few-layer graphene is a promising technique for the economical production of high-quality material. The gas-phase approach makes the method continuous, scalable, and highly tunable. However, little is known about the underlying physical and chemical processes, e.g., the kinetics of graphene formation and growth or the flakes morphology in the aerosol phase. This information is required to characterize and optimize production. Currently, the synthesis parameters are usually found empirically, through a combination of trial-and-error parametric studies and *ex situ* materials characterization, which is time-consuming and often intrusive. There is a corresponding need to develop measurement tools that can help to build a fundamental understanding of the synthesis process, monitor the quality of produced graphene *in situ*, and ultimately find ways to increase yield while maintaining graphene high quality. On the other hand, the increasing production rates of graphene aerosols lead to occupational exposure and potential adverse health effects. Hence, reliable aerosol morphology characterization is critical to the regulation of graphene aerosol production and handling.

This thesis seeks to deploy laser-optical *in situ* diagnostics to assess the aforementioned challenges. Time-resolved laser-induced incandescence (TiRe-LII) technique is applied to graphene aerosols for the first time to measure the graphene volume fraction and specific surface area *in situ*. Moreover, the TiRe-LII enables distinguishing between graphene flakes and soot particles, which are often formed during the synthesis as the undesired by-product. Fourier-transform infrared (FTIR) absorption spectroscopy is used as an *in situ* line-of-sight technique to measure gaseous species involved in graphene synthesis. The laser-optical diagnostics were complemented with chemical kinetics simulations and mass spectrometry measurements to reveal the factors playing a major role in graphene formation kinetics. Additionally, the optical properties and morphology of synthesized graphene flakes were characterized using aerosol diagnostics and numerical simulations. Consequently, the connection between the graphene morphology and optical properties was established, and the spectroscopic model of crumpled graphene flakes was developed.

Zusammenfassung

Graphen und seine Derivate verfügen über außergewöhnliche elektrische, mechanische und thermische Eigenschaften, die den Einsatz dieser Materialien in zahlreichen bestehenden und neuen Anwendungen ermöglichen. Um die erwartet steigende Nachfrage nach diesen Materialien zu decken, werden Verfahren für die Graphenproduktion in großem Maßstab benötigt. Die derzeitigen Beispiele für die Massenherstellung von Graphen durch skalierbare Top-Down-Verfahren, z. B. Flüssigphasen-Exfoliation und chemische Graphenoxid-Reduktion, sind momentan nicht in der Lage Graphen durchgängig in der benötigten Qualität herzustellen, um seine einzigartigen Eigenschaften in Anwendungen zu nutzen.

Die mikrowellenunterstützte Gasphasensynthese von freistehendem mehrlagigem Graphen ist ein vielversprechendes Verfahren für die wirtschaftliche Herstellung von hochwertigem Material. Der Gasphasenansatz erlaubt es die Synthese kontinuierlich, skalierbar und einfach adaptierbar zu betreiben. Über die zugrundeliegenden physikalischen und chemischen Prozesse, z. B. die Kinetik der Graphenbildung und des Wachstums oder die Morphologie der Flocken in der Aerosolphase, ist jedoch nur wenig bekannt. Diese Informationen werden benötigt, um die Herstellung zu charakterisieren und zu optimieren. Gegenwärtig werden die Syntheseparameter in der Regel empirisch anhand von parametrischen Studien und Ex-situ-Materialcharakterisierung ermittelt, was sehr zeitaufwändig ist und oft mit intrusiven Messverfahren erfolgt. Dementsprechend besteht ein Bedarf an der Entwicklung von alternativen Messtechniken, die dazu beitragen können, ein grundlegendes Verständnis des Syntheseprozesses zu entwickeln, die Qualität des hergestellten Graphens in situ zu überwachen und schließlich Wege zu finden, die Ausbeute zu erhöhen und gleichzeitig die hohe Qualität des Graphens zu erhalten. Andererseits führen die steigenden Produktionsraten von Graphen-Aerosolen zu einer Arbeitsplatzexposition mit potenziellen negativen Auswirkungen auf die Gesundheit. Daher ist eine zuverlässige Charakterisierung der Aerosolmorphologie von entscheidender Bedeutung für die Regulierung der Graphen-Aerosolproduktion und -handhabung.

In dieser Arbeit wird versucht, laseroptische In-situ-Diagnostik einzusetzen, um Teile der oben genannten Herausforderungen zu lösen Die zeitaufgelöste laserinduzierte Inkandeszenztechnik (TiRe-LII) wird zum ersten Mal auf Graphen-Aerosole angewandt, um den Graphen-Volumenanteil und die spezifische Oberfläche in situ zu messen. Darüber hinaus ermöglicht die TiRe-LII-Technik die Unterscheidung zwischen Graphenflocken und Rußpartikeln, die bei der Synthese häufig als unerwünschtes Nebenprodukt entstehen. Die Fourier-Transformations-Infrarot-Absorptionsspektroskopie (FTIR) wird als In-situ-Sichtlinienverfahren zur Messung der an der Graphen-Synthese beteiligten gasförmigen Spezies eingesetzt. Die laseroptische Diagnostik wurde durch chemisch-kinetische Simulationen und massenspektrometrische Messungen ergänzt, um die Faktoren aufzudecken, die bei der Kinetik der Graphenbildung eine wichtige Rolle spielen. Zusätzlich wurden die optischen Eigenschaften und die Morphologie der synthetisierten Graphenflocken durch Aerosoldiagnostik und numerische Simulationen charakterisiert. Infolgedessen wurde der Zusammenhang zwischen der

Graphenmorphologie und den optischen Eigenschaften hergestellt und das spektroskopische Modell der geknüllten Graphenflocken entwickelt.

Acknowledgements

The last 4.5 years have been an overwhelmingly positive experience in my life, for which I have so many people to thank.

First, my dream team of supervisors: Prof. Christof Schulz and Prof. Kyle James Daun. From our very first meeting in Duisburg, I was sold by your passion, kindness, and vision. Your immense knowledge and support helped me move forward and gave me strength when I needed it. Thank you for your patience and for giving me the freedom to pursue different ideas. In my eyes, you will forever be an example to follow, both as researchers and human beings!

I owe so much to the two group leaders I was lucky to work with, Prof. Thomas Dreier and Torsten Endres. You always kept your doors open (Thomas literally) and were there when I needed some advice. Thank you for sharing your knowledge, I sure learned a lot from you.

I want to thank Greg Smallwood for his contagious everlasting joy of conducting pure research and for my two incredible stays at the National Research Council Canada. Every single member of the Metrology Lab was a definition of "Canadian niceness", and I felt like I belonged there. In no particular order: Fengshan, Dan, Brett, Simon-Alexandre, Jalal, Prem, Stéphanie, thank you all! Hope you did not mind me playing with all your equipment at the same time. Special thanks go to my friend Joel who I bothered with my dumb questions the most. You are my continuous inspiration in how tranquil and yet efficient a researcher can be.

This work would not be possible without technical and administrative support. Erdal, Ludger, Sebastian, Beate, Barbara – without you the "IVG Titanic" and I would sink in no time. You guys are the real MVP.

My gratitude goes to absolutely every single colleague at the IVG diagnostics and nanoparticles groups and WatLIT group in Waterloo. To name only a couple of examples. Stephen and Sina, the 'SSS' team was a SucceSS. Raphael, I am forever grateful for your help during my first months in Duisburg, both in and out of work. I am honored to earn your support as a colleague and a friend. Paolo, whenever I had a question about graphene, you knew the answer. This journey would be so much harder and less fun without you. Steven, you were always there to help me with everything, and I cannot thank you enough. I admire your ability to juggle myriads of responsibilities and always stay positive. And thanks to everyone who I occasionally enjoyed beers with in Finkenkrug, which itself deserves a special shout-out.

Also, thanks to the IMPRS RECHARGE program and all my fellow students there. Looking back at it, we had so much fun together! Dear Rita Groever, your big heart made it an even more enjoyable experience.

For daring to pursue a Ph.D. I have to thank my former colleagues. Thank you, Ekaterina, for introducing me to science, Evgeny for being my mentor in work and life in general, Prof. Alexander Eremin for creating a working group where everyone feels valued and cared for. And thank you, Pavel, for being my friend all those years. How much time we spent together commuting!

For this clean document template, I must thank my friend Tim, who is a brilliant researcher and a talented designer.

To the families of Tarasov's and Fjodorow's – thank you for introducing me to the city, helping with the German bureaucracy, and letting me into your small but cozy community.

I want to thank my old hometown friends whose friendship I value so much and hope to carry throughout my life. I am fortunate to grow up with you in all senses.

To my partner, Anastasiia, you filled the last two years of my life with warmth and light. You teach and 'upgrade' me in so many ways, and I look forward to the future we share together.

Lastly, I am forever indebted to my family who believed in me and let me do my thing.

Table of contents

Nomenclature

This section lists the symbols and abbreviations used in the thesis. Where applicable, chapter restrictions are mentioned.

Symbols

Symbol	Description
A_{cond}	Surface area available for conductive heat transfer
A_v	Spectral absorbance
α	Thermal accommodation coefficient
B_{12}	Einstein coefficient
$b_{\mathrm{abs},\lambda}$	Aerosol spectral absorption coefficient
$b_{\mathrm{ext},\lambda}$	Aerosol spectral extinction coefficient
c_0	Speed of light in vacuum
$C_{\mathrm{abs},\lambda}$	Spectral absorption cross-section
$C_{\mathrm{ext},\lambda}$	Spectral extinction cross-section
c_{g}	Mean thermal speed of the gas molecules
c_p	Specific heat capacity
$C_{\mathrm{sca},\lambda}$	Spectral scattering cross-section
c_{V}	Mean thermal speed of the vapor
C-value	Multiple scattering correction factor
d_{ae}	Aerodynamic diameter
d_{m}	Mobility diameter
d_{p}	Particle diameter
$d_{\mathrm{p,eff}}$	Nanoparticle effective diameter
d_{V}	Volume equivalent diameter
ΔH_{V}	Molar heat of vaporization
e	Elementary charge
$E(\mathbf{m}_\lambda)$	Absorption function
E_1	Lower state energy
F_0	Laser fluence
f_V	Nanoparticle volume fraction
g_1	Lower-state statistical weight (degeneracy)

G_λ	Setup-specific parameter accounting for detector geometry and efficiency
h	Planck constant
I(Chapter 4)	Aerosol current
I_v (Chapter 6)	Transmitted light intensity
$I_{v,0}$ (Chapter 6)	Incident light intensity
J_λ	Spectral incandescence intensity
J_λ^{exp}	Experimental spectral incandescence intensity
$J_{\lambda,i}^{\mathrm{mod}}$	Modeled spectral incandescence intensity
k_{B}	Boltzmann constant
Kn	Knudsen number
κ_{v}	Spectral absorption coefficient
$<L>$	Mean flake lateral size
L (Chapter 5)	Flake characteristic length
L (Chapter 6)	Total absorption path
λ	Wavelength
λ_{g}	Mean free path in the gas
λ_{l}	Laser wavelength
M	CPMA mass setpoint
$\mathbf{m}_\lambda$	Complex refractive index
m^*	Particle mass concentration
m/z	Species mass-to-charge ratio
m_0	Mass concentration of the uncharged particles
m_{p}	Nanoparticle mass
M_{V}	Vapor molar mass
m_{V}	Vapor species mass
$<N>$	Mean layer number
N(Chapter 6)	Gas species concentration
N_g''	Incident number flux of gas molecules per elementary area
n_{g}	Molecular number density
n_{med}	Index of refraction
v	Wavenumber
p_{g}	Gas pressure
p_{V}	Vapor pressure
q_{abs}	Energy absorption rate
q_{cond}	Conduction cooling rate
q_{evap}	Evaporation cooling rate
q_{rad},	Radiation cooling rate
$Q_{\mathrm{ext},\lambda}$	Spectral extinction efficiency
$Q_{\mathrm{abs},\lambda}$	Spectral absorption efficiency

$Q_{\mathrm{sca},\lambda}$	Spectral scattering efficiency
Q_{sample}	Sample gas flow
Q_{sheath}	Sheath gas flow
R_{d}	Mobility diameter resolution
R_{s}	Aerodynamic diameter resolution
ρ	Nanoparticle material density
σ	Standard deviation or standard deviation of the mean
t	Time
T_{g}	Gas temperature
T_{p}	Nanoparticle temperature
T_{peak}	Nanoparticle peak temperature
U_{int}	Internal energy of the particle
ζ_{rot}	Number of rotational degrees of freedom

Abbreviations

Abbreviation	Description
2D	Two-dimensional
AAC	Aerodynamic aerosol classifier
AAE	Absorption Ångström exponent
AL	Alveolar region
BET	Brunauer-Emmett-Teller
CAPS $\mathrm{PM}_{\mathrm{SSA}}$	Cavity attenuation phase-shift particulate matter single scattering albedo monitor
CCD	Charge-coupled device
CEM	Controlled evaporation and mixing
CERMS	CPMA-electrometer reference mass system
CMD	Count median diameter
CPC	Condensation particle counter
CPMA	Centrifugal particle mass analyzer
CVD	Chemical vapor deposition
DDA	Discrete dipole approximation
DF	Deposition fraction
DMA	Differential mobility analyzer
EM	Electromagnetic
FCAE	Faraday-cup aerosol electrometer

FLG	Few-layer graphene
FTIR	Fourier-transform infrared (spectroscopy)
FWHM	Full-width at half of maximum
GSD	Geometric standard deviation
HA	Head airways
HAN	Height above the nozzle
HEPA	High efficiency particulate air
IR	Infrared
ISO	International organization for standardization
IVG	Institute for combustion and gas dynamics
LB, UB	Lower bound, Upper bound
LDLS	Laser-driven light source
LIBS	Laser-induced breakdown spectroscopy
LOSA	Line-of-sight attenuation
MA	Multi-alkali photocathode
MAC	Mass absorption cross-section
MCP	Micro-channel plate
MEC	Mass extinction cross-section
ND	Neutral density
Nd:YAG	Neodymium-doped yttrium aluminium garnet
NRC	National Research Council Canada
OES	Optical emission spectroscopy
PAH	Polycyclic aromatic hydrocarbons
PDF	Probability density function
PMT	Photomultiplier tube
ppm	Parts per million
QMS	Quadrupole mass spectrometer
RDG	Rayleigh-Debye-Gans
RDG-FA	Rayleigh-Debye-Gans fractal-aggregate
rGO	Reduced graphene oxide
SBA	Super bi-alkali photocathode
sccm	Standard cubic centimeter
SEM	Scanning electron microscope
slm	Standard liters per minute
SMPS	Scanning mobility particle sizer
SSA (Chapter 4)	Single scattering albedo
SSA (Chapter 5)	Specific surface area
TAC	Thermal accommodation coefficient
TB	Tracheobronchial region

TEM	Transmission electron microscopy
TiRe-LII	Time-resolved laser-induced incandescence
UDAC	Unipolar diffusion aerosol charger
UDE	University of Duisburg-Essen
UV-Vis	Ultraviolet-visible
UW	University of Waterloo
XPS	X-ray photoelectron spectroscopy

Chapter 1
Introduction

Graphene, the carbon-based two-dimensional (2D) material, has gained a lot of attention in the last two decades, mainly after the study of Novoselov and Geim in 2004 [1], who derived the freestanding single-layer graphene and experimentally described its unique electrical properties, for which they received the Nobel prize in 2010. Since then, it has been demonstrated that graphene and its derivatives, e.g., few-layer graphene (FLG), also possess exceptional optical, mechanical, and thermal properties that can be utilized in numerous applications [2–9]. Accordingly, to fulfill the quickly growing demand for graphene materials, large-scale production is needed [10].

The current examples of graphene mass fabrication typically exploit traditional top-down approaches, e.g., liquid-phase exfoliation and graphene oxide reduction, which are scalable but incapable of consistently producing graphene at the quality levels needed to exploit its unique properties in applications [6,10,11]. A different approach is the bottom-up gas-phase synthesis. Gas-phase synthesis is a continuous process, which makes it easily scalable and reduces quality variability from batch to batch. Moreover, the bottom-up approach allows thorough control of the synthesis parameters, such as the choice and concentration of a precursor, temperature history, and bath-gas conditions. Hence, the process can be tuned to achieve desired product characteristics.

This dissertation focuses on the gas-phase microwave-assisted synthesis of graphene. In it, microwave radiation is used to induce plasma, which dissociates the gaseous carbon-containing precursor into fragments. These fragments then experience rapid cooling downstream of the hot plasma region and re-assemble into graphene flakes. The method was shown to consistently produce high-quality FLG flakes [12].

Complex physical and chemical processes underly the gas-phase synthesis of graphene, which are not fully understood yet: precursor decomposition, initial graphene formation from the gas-phase building blocks, consequent flakes growth, and changes of morphology in the aerosol phase. Understanding these processes would allow for more precise production control and process optimization, e.g., increased yield. A traditional way to investigate the gas-phase synthesis of graphene is through a trial-and-error approach, when certain process parameters are varied and the produced materials are collected and characterized *ex situ,* for example, using electron microscopy or Raman spectroscopy. Such an approach, however, is time-consuming and disregards the intermediate synthesis steps, which define the final graphene morphology and properties.

There is a corresponding need to develop *in situ* diagnostics that can provide spatially- and temporally-resolved data on graphene gas-phase synthesis, e.g., temperature history, stable and intermediate species distributions, and physicochemical properties of graphene. Advanced understanding of graphene gas-phase formation and availability of *in situ* diagnostic tools are vital to enhancing production rates and will lead to the improved commercial viability of graphene-related materials. This thesis deploys two laser-optical *in situ* diagnostics that can fulfill the aforementioned needs: time-resolved laser-induced incandescence (TiRe-LII) and Fourier-transform infrared (FTIR) absorption spectroscopy.

TiRe-LII technique is commonly used to measure nanoparticle aerosol volume fraction, size distribution, and several thermophysical parameters. This method typically deploys nanosecond laser pulses to heat the aerosol, so the nanoparticles start to emit thermal radiation, i.e., incandesce. The time-resolved incandescence signals at a single or at multiple wavelengths are detected using photomultiplier tubes or a streak camera and analyzed to yield the quantities of interest. Interpreting the TiRe-LII signals requires a theoretical description of the nanoparticle heating by laser energy absorption and subsequent cooling mechanisms. No TiRe-LII theoretical models and experiments on graphene aerosols were reported before this work.

FTIR absorption spectroscopy allows for identifying and quantifying of IR-absorbing species. The method involves an IR-light source that shines radiation through a sample at multiple frequencies simultaneously using a Michelsen interferometer. Different functional groups that are present in the sample absorb IR radiation at frequencies that induce their characteristic rovibrational states and hence, different transmission spectra are produced, which are recorded with an IR detector. In this work, FTIR absorption is applied *in situ* as a line-of-sight technique. That is, the IR beam is guided through the reactor, where graphene and multiple intermediate and stable gaseous by-products are formed, thus providing information on the process kinetics.

The goal of this work is to advance the fundamental understanding of graphene gas-phase microwave-plasma synthesis and reveal factors playing a major role in graphene formation kinetics. This is approached by developing diagnostics that can monitor graphene quality and measure various graphene properties and process parameters *in situ*. Chapter 2 provides background for the study and outlines the research objectives. Chapter 3 describes the gas-phase microwave-plasma synthesis of freestanding graphene aerosols and provides details on the *ex situ* characterization of the produced graphene powders. Chapter 4 experimentally and numerically investigates the morphology and optical properties of graphene aerosols, which are required to build the theoretical TiRe-LII model of graphene and predict its adverse health effects in the case of exposure. Chapter 5 introduces the TiRe-LII technique and demonstrates its application to measure graphene volume fraction and specific surface area. Chapter 6 moves on with the line-of-sight FTIR absorption, which is used to measure the evolution of gaseous by-products during graphene synthesis. Additionally, chemical kinetics simulations and mass spectrometry measurements are presented to support the *in situ* diagnostics. Chapter 8 summarizes the main findings of this work, discusses the remaining questions, and provides directions for future studies.

Chapter 2
Background and motivation

Single-layer graphite, i.e., graphene, has been an object of research for more than 70 years [13,14], long before the famous study by Novoselov and Geim in 2004 [1]. Some of the electrical and optical properties of a single hexagonal plane of graphite were theoretically predicted and explicitly described several decades ago [15]. Most of these studies were considered purely theoretical because graphene was assumed to be too unstable to exist in the free state. In particular, surface energy calculations indicated that the graphene monolayer should break into isolated islands, or bend into nanotubes and fullerenes. Arguably, the first experimental evidence of graphene (oxide) flakes was presented by Hanns-Peter Boehm at the Carbon Conference at Penn State University in 1961 [16] and later published in Germany in 1962 [17]. However, at the time, his work did not arouse much interest. In 1986, together with his colleagues Ralph Setton and Eberhard Stumpp, Boehm introduced the term “graphene” for single-layer graphite [18].

However, only after the Nobel prize-winning work by Novoselov and Geim [1] in 2004, the number of papers on graphene synthesis, diagnostics, and applications in various fields started to grow exponentially [19,20]. In their study, Novoselov and Game experimentally proved the freestanding stability of the single-layer graphene in ambient conditions and showcased its unique electrical properties. That work shifted the perspective from graphene considered to be a purely theoretical material to the applied one, thus drastically boosting further research. What started with single-layer graphene, has since expanded into a large family of graphene-related materials, such as bilayer and few-layer graphene, graphene nanoplatelets and nanoribbons, graphene quantum dots, graphene oxide, reduced graphene oxide, multiple variants of functionalized graphene and graphene composites, etc. A comprehensive review of the current variety of graphene-related materials is provided in Ref. [21]. This dissertation focuses exclusively on the gas-phase synthesis of few-layer graphene (FLG). What is arguably an even more important consequence of the popularity of graphene, is that it paved the way for the experimental discovery and applications of multiple other families of 2D materials, e.g., elemental layered materials from groups III–VI (silicene, phosphorene, etc.) [22,23], transition metal dichalcogenide monolayers (MoS2, WSe_2, etc.) [24], hundreds of MXenes [25], halide perovskites [26], and thousands of theoretically predicted layered materials [27]. The rise of numerous new 2D materials, often with unique properties, however, does not imply the end of the graphene era, rather that the field of 2D materials thrives and expands in multiple directions simultaneously. *There's still plenty of room at the bottom*, be it graphene or any other layered material.

Graphene and its derivatives possess exceptional electrical, mechanical, and thermal properties, which enable the use of these materials in numerous existing and emerging applications. Defect-free single-layer graphene has a theoretical surface area of 2630 m^2/g, which makes it promising candidate support material for the flexible embedding of heterogeneous catalysts [2]. Moreover, surface functionalization makes graphene a highly efficient material for energy conversion and storage [3,4]. Suspended single-layer graphene has been reported to have a very high thermal conductivity (4840–5300 W/mK) [4], which is similar to [5] or exceeding that of single-wall carbon nanotubes [6]. The outstanding thermal conductivity of graphene suggests its use in multiple applications, e.g., heat sinks and heat pipes in electronics [7], and graphene-coated heating fabrics [28]. Graphene also exhibits exceptional mechanical properties, including an intrinsic strength up to 42 Nm^{-1} and Young's modulus of 2.4 TPa [8,9]. Its mechanical stability, combined with its high surface-to-volume ratio and electronic properties, makes graphene practical for strain, magnetic, chemical, and nanoelectromechanical sensors [29]. The unique electrical properties of graphene make it a promising material for lithium-ion/sulfur batteries, fuel and solar cells, and supercapacitors [19,30]. Overall, more than 40 distinct application areas of graphene were identified in the 2020 Graphene Council Survey based on 800+ respondents from commercial and academic organizations [10]. Although there is a consensus on the superior features of graphene, the values of the electrical, thermal, optical, and mechanical properties reported in the literature vary widely, possibly due to the strong influence of impurities and defects, which highlights the importance of robust characterization of graphene materials.

As a result of plentiful existing and potential graphene applications, the demand for high-quality graphene is rapidly growing. Today, at least 14 different synthesis methods exist through which graphene and its derivatives, e.g., graphene oxide [31], reduced graphene oxide [32], silicon-doped [33,34], and nitrogen-doped graphene [35], can be produced [36]. The fabrication techniques can generally be categorized into two groups: top-down (exfoliation [37], ball-milling [38], etc.); and bottom-up approaches (chemical vapor deposition (CVD) [39], epitaxial growth [40], thermolysis [41], microwave plasma treatment [34,42]). Different material systems in all states of matter have been used for graphene production: gases [34], liquids [43], and solids [44]. The most common graphene production methods and their evaluation in terms of quality, cost, scalability, chemical purity, and product yield are shown in Figure 2.1.

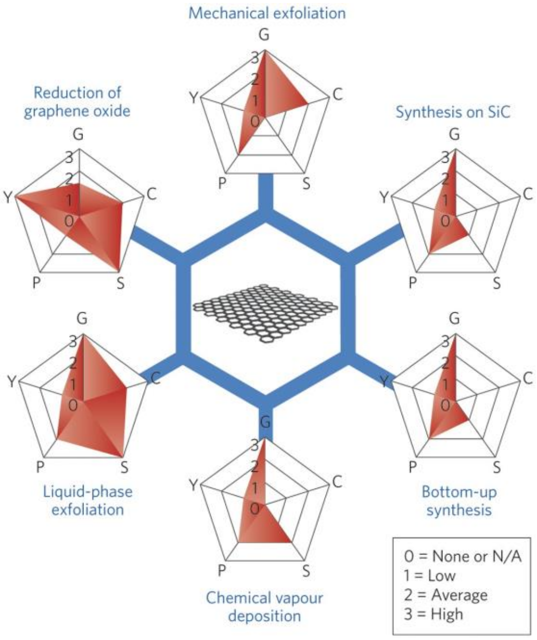

Figure 2.1 Common graphene production methods. Each method has been evaluated in terms of graphene quality (G), cost aspect (C; a low value corresponds to high cost of production), scalability (S), purity (P), and yield (Y) of the overall production process. Reprinted from [6] with permission from "Springer Nature".

2.1 Commercial adoption of graphene

As of 2022, there are multiple examples of successful mass fabrication of graphene, mostly via traditional top-down synthesis routes, e.g., graphite exfoliation and graphite oxidation-reduction. A handful of manufacturers even report production capacities of at least a few tons per year. Some examples are NanoXplore Inc (Canada), NeoGraf Solutions LLC (US), First Graphene Ltd (Australia), and SuperC Technology Ltd (China), which deploy graphite exfoliation; Levidian Nanosystems Ltd (UK), which utilizes gas-phase methane cracking; and Sixth Element Materials Technology Co Ltd (China) that uses graphite oxidation-reduction. However, Figure 2.1 shows that the most scalable approaches, e.g., liquid-phase exfoliation and reduction of graphene oxide, are currently incapable of producing the levels of purity needed to exploit the unique properties of graphene in many emerging applications. A 2018 study by Kauling et al. [11] assessed commercially-available graphene samples from more than 60 companies using a systematic reliable protocol. They found that most of the graphene samples were, in fact, graphite microplatelets, and unsuitable for many applications due to their poor quality. The study concluded that "there is almost no high-quality graphene, as defined by ISO, in the market yet". Another benchmarking study from 2019 by Kovtun et al. [45] analyzed 11 graphene samples produced by exfoliation and available on the European market on at least at kilograms scale. They found that the samples demonstrated either a high degree of surface quality (high carbon sp^2 content) or high specific surface area (small number of layers), but not both. The authors concluded that "production of high-quality graphene, even if possible at lab scale, still represent a major industrial challenge".

According to the 2020 Graphene Council Survey [10], the top three obstacles to graphene commercial adoption are high cost (or rather the perception of such by non-experts), lack of industrial-scale production, and inconsistency in material quality from batch to batch. The definition of "graphene quality" is not strict, as the graphene material that is inappropriate for one application may be sufficient for another. Thus, it is not graphene "low quality" *per se,* but rather the lack of or deviation from the characteristics stated on a batch, which leads to graphene's poor performance in a specific application and intimidates potential end-users. Therefore, to facilitate commercial adoption of graphene and encourage the development of new graphene applications, first, scalable and low-cost synthesis approaches must be developed. Second, given the range of graphene materials with different characteristics and reproducibility issues, international standards on definitions and properties characterization for graphene and related materials must be established.

Regarding graphene regulations and standardization, although still lagging, significant efforts have been undergoing in the last five years. Only recently, in 2017, the International Organization for Standardization (ISO) launched the first nomenclature for graphene and related 2D materials [46]. According to ISO's definitions, graphene is a single layer of carbon atoms, bilayer graphene is a stack of two well-defined layers, and few-layer graphene is a stack of 3–10 graphene layers at room temperature. The procedure of structural characterization of graphene from powders and liquid dispersions was standardized by ISO only in 2021 [47]. Furthermore, in 2021, the Graphene Council (the global community for graphene professionals and companies) developed the Graphene Classification Framework, which builds on the existing ISO standards and suggests a method of classifying and comparing any form of graphene through the use of 19 main graphene characteristics [36]. Currently, the Graphene Flagship initiative runs 35 projects in the combined European Union's effort to standardize the characterization of graphene materials' structural and electrical properties [48,49]. The graphene materials produced in the context of this thesis are extensively characterized following the procedures as defined by ISO. Moreover, the crumpled graphene aerosol morphology presented in Chapter 4 is comprehensively classified for the first time, thus contributing to the development of new standards and health and safety regulations.

Health and safety regulations for graphene and related materials must be established to understand their potential adverse health effects and mitigate the risks. The large-scale production, use of graphene in various products, and their consequent disposal will inevitably lead to occupational exposure and accumulation of graphene materials in the environment [50]. Human contact with graphene is possible through several routes: airway exposure, dermal adsorption, oral administration, intravenous, and intraperitoneal injection. The most abundant unintentional exposure to graphene is inhalation, while intravenous administration is an important case of intentional use of graphene in biomedical applications. Apart from human-related health risks, the environmental hazard of graphene-related materials must also be assessed, such as their impact on radiative forcing and interaction with flora and fauna.

To date, it is well established that multiple physicochemical parameters determine graphene toxicity: concentration, lateral size, shape, functionalization state, purity, aggregation state, and surface charge [50]. However, due to a wide range of graphene materials having different characteristics, there is little consensus on the corresponding toxicity effects [51–54]. Contrasting opinions appear in the literature, with some results suggesting biocompatibility of certain graphene materials, while others report toxic effects [52]. Rather, the devil is in the details, and every material making it to the market must currently undergo time-consuming and costly toxicological studies. This highlights the need for the extensive physicochemical characterization of graphene products so that their characteristics could be distinctly linked to their respective health effects. This approach would mean the transition from descriptive to predictive toxicology [50].

This dissertation does not seek to assess the toxicological effects of graphene aerosols synthesized throughout the study. Instead, the set of laser-optical and aerosol diagnostics was deployed to comprehensively characterize the morphology and measure concentrations of crumpled graphene aerosols *in situ* for the first time. The obtained material characteristics could be used to predict the exposure and environmental risks once the corresponding models are developed.

2.2 Brief history of gas-phase microwave-assisted graphene synthesis

The focus of this dissertation is the gas-phase microwave-assisted graphene synthesis, which was first conceived and implemented by Dato et al. in 2008 [42]. This approach amounts to a substrate-free synthesis of few-layer graphene (FLG) flakes at atmospheric pressure in a microwave plasma reactor. In their study, Dato et al. introduced ethanol droplets into the reactor through a nozzle, where it was evaporated in an argon plasma. The reaction products underwent rapid cooling and condensed into few-layer graphene sheets downstream of the plasma.

Since then, gas-phase plasma synthesis of pristine and functionalized graphene has been investigated by several groups, both experimentally and numerically, and has been shown capable of producing crumpled but high-purity and low-defect FLG flakes from common alcohols and hydrocarbons with product yield up to 50 wt.% on a lab-scale [55–60]. In 2010, Dato et al. extended their initial work to other precursor materials and investigated the effects of precursor composition, plasma gas flow rate, and amount of applied microwave power on graphene production [61]. That work provided the first insights into the kinetics of the process and gave indications on parameters of significant importance, such as the C/H/O atomic ratio in the precursor and precursor residence time in the plasma zone. In 2013–2016, Tsyganov et al. developed the detailed kinetic scheme of ethanol decomposition during plasma treatment down to diatomic and atomic carbon [62,63]. The authors validated their model by comparing predicted H2 and CO concentrations in the products with experimental values obtained by mass-spectrometry. However, the kinetics of graphene formation from the atomic carbon was not addressed.

Considerable efforts have been invested into improving both graphene quality and yields. The precursor delivery method of injecting liquid droplets through a nozzle originally proposed by Dato et al. [42] was changed to vaporized precursor injection [64], which improved graphene yield. Tatarova et al. [64] controlled the product morphology by adjusting the gas temperature spatial profile in the post-plasma region of the reactor, thereby shifting the reaction toward graphene. Toman et al. [59] introduced a dual-channel nozzle design that allowed them to control product morphology and reduce the required microwave powers while maintaining graphene quality. Tsyganov et al. [57] optimized the reactor geometry to increase the graphene yield by enlarging the nucleation and assembling zones. Moreover, multiple parametric studies investigated the influence of reactant flow rates, delivered microwave powers, and precursor chemical composition on product morphology [55,56,61,63,65].

Gas-phase microwave-plasma production of graphene has been a research focus at the Institute for Combustion and Gas Dynamics of the University of Duisburg-Essen from 2014–2018 by Münzer et al. [34], and currently by Fortugno et al. [55]. The authors were able to produce freestanding and chemically pure FLG from multiple carbonaceous precursors with different levels of crystallinity and yield. Münzer et al. also successfully demonstrated the application of produced FLG flakes in silicon-based lithium-ion batteries, which enhanced their long-term stability and Coulomb efficiency [34].

2.3 Motivation and overview of contents

Notwithstanding the large body of research on gas-phase graphene synthesis, the transport and kinetics mechanisms that underlie FLG nucleation and growth are still largely unknown. Further advancement in production rates and yields requires a comprehensive understanding of gas-phase kinetics (Figure 2.2). Moreover, tuning of the process parameters is usually done empirically, through a combination of parametric studies and trial-and-error, which is a time-consuming process. The time-intensive nature of this procedure is compounded by the fact that reactor performance is usually assessed using *ex situ* materials characterization that is also cost-ineffective and often intrusive. This presents a need to develop measurement tools that can monitor the synthesis process and quality of produced graphene *in situ* without relying exclusively on *ex situ* characterization. Laser-optical diagnostics presented in this thesis can fulfill this need. However, graphene aerosol optical and physical properties must be critically examined first, and the theoretical models for the subsequent laser-optical *in situ* diagnostics should be built.

Figure 2.2 “From research towards applications”, graphene diagram. Physical and optical properties must be known for *in situ* diagnostics to be applied, which might lead to a better understanding of the graphene formation kinetics, and consequently to the improved production efficiency with the eventual synthesis upscaling.

Hence, this work pursues both practical and fundamental goals. The former is to develop laser-optical tools that can monitor the formation, growth, and quality of graphene during its gas-phase synthesis and transfer. The latter is to advance a fundamental understanding of the processes underlying gas-phase graphene formation, and hence, ultimately help find ways to increase yield while maintaining graphene's high quality. The prerequisites for these tasks include designing and manufacturing the gas-phase synthesis reactor; detailed morphology characterization of produced graphene materials, *ex situ* in the powder form and online in the aerosol phase; and finally, modeling and experimental investigation of graphene-light interaction. The versatility of numerical tools and experimental diagnostics used throughout this research was possible as the result of a cotutelle agreement between the University of Duisburg-Essen and the University of Waterloo in close collaboration with the National Research Council Canada.

This thesis begins with Chapter 3, where the microwave-assisted gas-phase synthesis of freestanding graphene aerosols is introduced. The chapter describes the design and operation of the microwave-plasma reactor and presents the *ex situ* characterization of the produced powders.

Chapter 4 moves on to the online analysis of crumpled graphene morphology in the aerosol phase. Furthermore, the graphene-light interaction is probed for colloids and aerosols experimentally through the spectrally-resolved extinction and absorption measurements and theoretically through the first-principle modeling. Consequently, the crumpled FLG spectroscopic model required for the TiRe-LII analysis is established.

Chapter 5 describes the main concepts of TiRe-LII and demonstrates its application for the first time on crumpled FLG flakes. The graphene aerosol characteristics, including flake volume fraction and specific surface area, are probed.

Chapter 6 progresses with Fourier transform infrared spectroscopy deployed as an *in situ* line-of-sight absorption measurement. While TiRe-LII focuses on the particle phase, FTIR spectroscopy allows for identifying and quantifying gaseous species involved in the synthesis, thus providing insight into the process kinetics. The FTIR results are complemented with chemical kinetics simulations and mass spectrometry measurements to yield a comprehensive understanding of the flakes formation mechanism.

Finally, Chapters 7 and 8 conclude the thesis by summarizing the main findings, discussing their importance, and suggesting directions for future research.

Chapter 3

Graphene synthesis and *ex situ* materials characterization

This chapter discusses the gas-phase synthesis of freestanding graphene and other carbonaceous aerosols. Special attention is given to the design of a microwave-plasma reactor, which was manufactured specifically for this project to investigate graphene formation and growth *in situ*. The synthesis parameters and the *ex situ* characterization of the produced materials are presented.

3.1 Microwave plasma reactor

Graphene and other carbonaceous aerosols were synthesized in a microwave plasma reactor, which consists of several parts: the microwave generation and propagation system, shown in Figure 3.1; and the reactor part, shown in Figure 3.2. A water-cooled magnetron (Fricke und Mallah GmbH) generates microwave radiation (2.45 GHz, maximum power 2 kW), which is first propagated through a circulator, where the back-reflected part of the microwave radiation is directed into a water trap. The amount of back-reflected microwave power is measured with a microwave diode and read as a voltage on a multimeter. The circulator is connected to a three-stub tuner (Muegge GmbH) that allows impedance adjustment to minimize the return losses, and hence, maximize the amount of power delivered into a water- and air-cooled cylindrical resonator (Cyrannus, iplas GmbH). The reactant gases are fed through a 4-mm diameter nozzle to a transparent to microwave radiation fused silica tube (23 cm in length, 7 cm inner diameter) installed at the center of the resonator (Figure 3.2). The microwave radiation is focused along

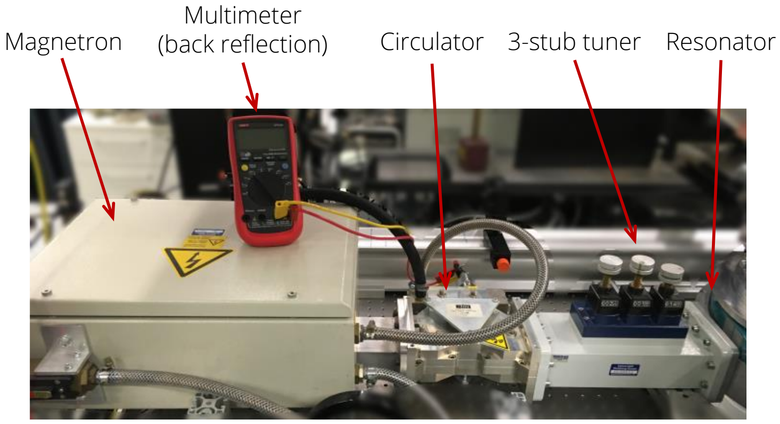

Figure 3.1 Photo of the microwave plasma generation and propagation system.

the center of the fused silica tube to generate a standing wave that ignites and supports the plasma. The microwave-induced plasma dissociates the precursor molecules into smaller fragments that re-assemble downstream into carbonaceous particles, e.g., graphene. Particles are then collected on a membrane filter at the reactor exit for further characterization.

The reactor used in this work was designed to investigate graphene gas-phase synthesis *in situ*. To avoid particle deposition on the windows, the windows were nitrogen-flushed, and the extended cross-piece parts were shielded from the inner tube with a metal plate, leaving a 5 cm×1.5 cm open rectangle for the optical beam passage (A—A cutting plane in Figure 3.2). In addition, the reactor was manufactured in a modular fashion, enabling optical measurements between 200 and 400 mm above the nozzle, thereby providing optical access to graphene aerosols at different stages of their formation, growth, and aggregation. To achieve stable reactor operation at high temperatures of atmospheric pressure plasmas, several parts required modifications, as established in the prior experiments conducted at IVG. In particular, the resonator cooling system was improved, and the nozzle tip was changed from a flat to a conical design, which is shown in red color in Figure 3.2. After the implemented updates, the reactor could be operated at atmospheric pressure while keeping the housing temperature below 170 °C, which is lower than the 200 °C damage threshold for the silicone O-rings used in the reactor. Under these conditions, the limiting factor for operating the reactor was the time before the windows become fouled with particles making *in situ* optical diagnostics impossible, which could be up to several hours depending on the synthesis parameters.

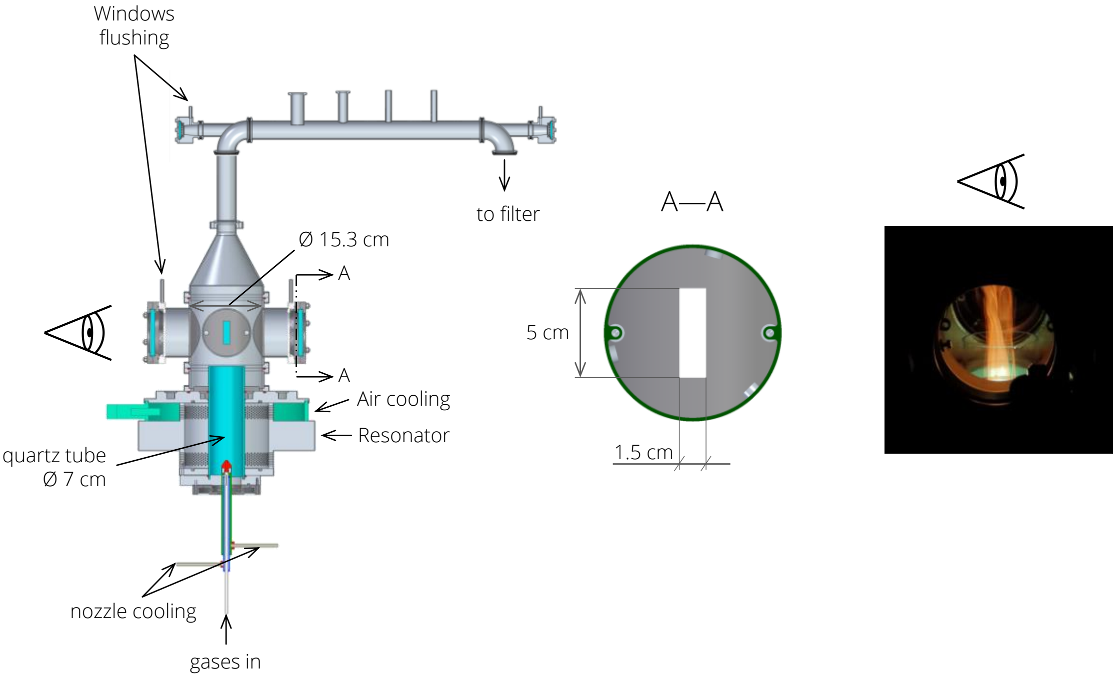

Figure 3.2 Half-section of the microwave plasma reactor. The cutting plane A-A shows the metal shielding designed to minimize the particle deposition on windows with a rectangular slit for optical beam propagation. The photo on the right illustrates the torch of hot graphene flakes synthesized from ethanol at 700 mbar, which exit the fused silica tube (courtesy of M. Asif, IVG). The metal shielding was disassembled for taking the photo.

Safe reactor operation in terms of temperature and pressure was ensured with several automated measures. When the pre-set threshold pressure of 1.15 bar is exceeded, two electric pressure gauges send the signal to switch off pneumatic valves and stop any additional gases flowing into the reactor, and a mechanical valve opens a bypass to divert the gas flow from the reactor to a pump. The temperatures of the reactor outer walls at three locations and nozzle cooling water are continuously measured with thermocouples, and the readings are shown in a LabVIEW program. When the wall temperature at any location is above 170 °C or cooling water temperature is above 40 °C, the signal is sent to switch off pneumatic valves and stop gas flows. That leads to absence of gases absorbing microwave radiation in the reactor and hence prevents it from further heating.

3.2 Graphene synthesis and process parameters

Graphene and other carbonaceous aerosols were synthesized using various precursors, known to produce either pure few-layer graphene (FLG) flakes, spherical soot-like particles, or mixtures of both [55], as summarized in Table 3.1. Crumpled FLG flakes were produced in Case 1 from vaporized ethanol (C_2H_5OH, ≥99.8 % purity). Spherical aggregated particles that resemble typical soot were synthesized in Case 2 from vaporized toluene (C_7H_8, ≥99.5 %). The term soot or black carbon is defined by the Intergovernmental Panel on Climate Change as a form of carbon arising from the incomplete combustion of fuels. However, high-temperature pyrolysis of carbonaceous materials, such as the one in this work, also leads to the formation of aggregates consisting of spherical particles that are commonly named “soot”. Therefore, the spherical aggregated particles synthesized throughout this thesis are referred as soot particles. In Cases 3–6, precursor mixtures of ethylene (C_2H_4, ≥99.9 %) and deionized water (milli-Q, 18.2 MU) led to the formation of either pure FLG flakes (Case 6) or FLG/soot particle mixtures (Cases 3–5). Precursor flow rates were adjusted so that, if the precursor is fully decomposed to the atomic level, the atomic carbon concentration equals approximately 6800 parts per million (ppm). That is the carbon-atom concentration of fully decomposed 190 standard cubic centimeters per minute (sccm) of ethanol, the case, which is known to produce high-quality crumpled FLG [55,66]. Flowrates of ethanol were additionally varied between 120–400 sccm (4332–14368 ppm of atomic carbon) to investigate how carbon atom concentrations influenced the formation of aerosols. The yield analysis was carried out in the previous study using similar reactor and synthesis parameters [55]. The yield was calculated as the mass of the produced powder divided by the total carbon mass introduced into the reactor as a precursor.

Table 3.1 Precursors used in the study and produced materials.

Case	Precursor	Flow rate / sccm	H_2O flow rate / sccm	C:O:H ratio	Product	Yield / wt.% [55]
1	Ethanol	190	0	2:1:6	Few-layer graphene (FLG)	1.8
2	Toluene	54.3	0	7:0:8	soot	36
3	Ethylene	190	0	2:0:4	(less) FLG / (more) soot	6.5
4	Ethylene	190	95	2:0.5:5	FLG / soot	4
5	Ethylene	190	190	2:1:6	(more) FLG / (less) soot	2.5
6	Ethylene	190	285	2:1.5:7	FLG	1.5

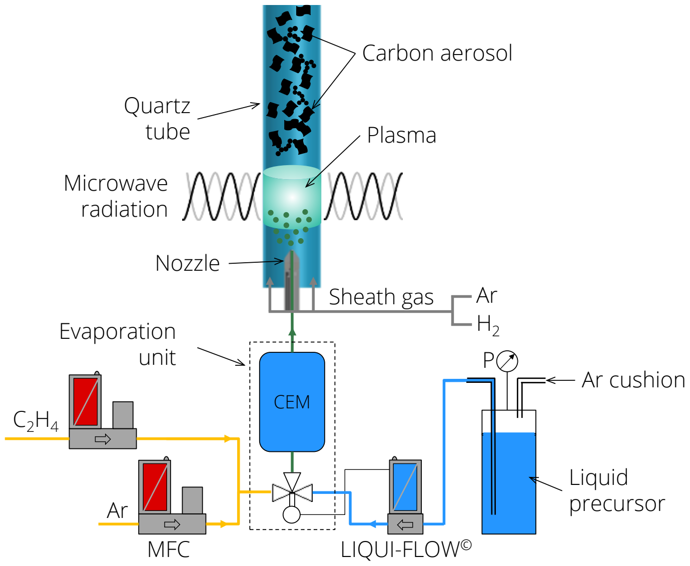

Figure 3.3 Schematics of the gas-phase plasma synthesis used to produce few-layer graphene (FLG) and other carbonaceous aerosols. Liquid precursor is atomized in argon and evaporated at 453 K. The precursor is dissociated in a microwave-induced plasma, and forms FLG (or soot) nanoparticles downstream of the plasma region.

The synthesis principle is summarized in Figure 3.3. The precursor is combined with 5 standard liters per minute (slm) of Ar (5.0 purity) and evaporated at 453 K in a controlled evaporation and mixing unit (CEM W-202A, Bronkhorst). Liquid reactants were metered with a liquid mass flow controller (mini CORI-FLOW ML120V00, Bronkhorst). The diluted gas stream exits a 4-mm diameter nozzle surrounded by a tangential sheath flow of 40 slm of Ar (5.0) and 1 slm of H_2 (5.0), all contained within a 7-cm diameter fused silica tube. The sheath flow of Ar and H_2 suppresses particles deposition on the reactor and fused silica tube walls and provides homogeneous temperature distribution within the reacting volume. The microwave-induced plasma dissociates the precursor molecules into fragments, which re-assemble into carbonaceous particles downstream. The generated microwave power can be varied between 1–2 kW. The default power value of 1.4 kW was used throughout this thesis unless stated otherwise. Particles were sampled on a membrane filter at the reactor exit for further characterization. An additional flow of 10 slm N_2 (5.0) was used to flush the reactor windows. All gas flows were controlled by calibrated mass flow controllers (Bronkhorst) and the reactor was checked for leaks before every set of experiments. The reactor pressure was maintained at 1 bar using a PID controller, which regulated the amount of additional N_2 flow directed to the pump.

3.3 *Ex situ* characterization

To provide a comprehensive understanding of particle morphology and chemical composition, synthesized particles were extensively analyzed *ex situ* using electron microscopy, Raman spectroscopy, and X-ray photoelectron spectroscopy. The samples were collected in two ways: harvested from a membrane filter as a powder or sampled from the reactor directly on a grid using an electrostatic precipitator.

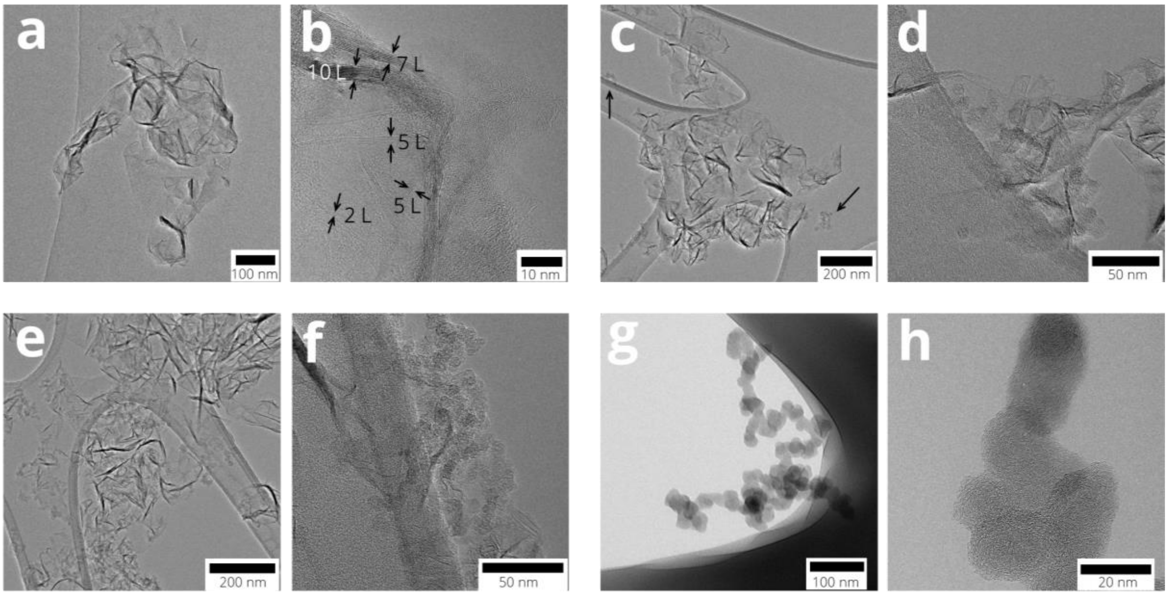

Figure 3.4 TEM images of synthesized carbonaceous particles using various precursor flow rates and microwave powers: (a,b) FLG flakes, 190 sccm of ethanol, 1.4 kW; (c,d) FLG flakes/soot particles, 190 sccm of ethanol, 1.0 kW; (e,f) FLG flakes/soot particles, 400 sccm of ethanol, 1.4 kW; (g,h) soot particles, 54.3 sccm of toluene, microwave power: 1.4 kW.

3.3.1 Electron microscopy

The particle morphology was analyzed with transmission electron microscopy (TEM, Cs-corrected JEOL Ltd., JEM 2200FS, operated at 200 kV), scanning electron microscopy (Hitachi Inc., SEM, S-5200, operated at 30 kV), and tomographic TEM (FEI Titan 80-300 LB). Figure 3.4 shows TEM images of carbonaceous nanoparticles harvested from the filter. For the analysis, several milligrams of collected powder were diluted in ethanol (≥99.8 % purity) and ultrasonicated for 20 min. A few droplets of the obtained nanocolloid were drop-casted on a 300-mesh copper grid with a carbon support film and left drying for a few minutes before the analysis.

The effect of microwave power level on the particle morphology was investigated by comparing two samples synthesized from 190 sccm of ethanol (Case 1), using either 1.4 kW (Figure 3.4 a,b) or 1.0 kW microwave power (Figure 3.4 c,d). Figure 3.4 a,b shows crumpled FLG flakes with lateral sizes of 200–400 nm and thicknesses of less than ten graphene layers, which is consistent with the ISO definition of few-layer graphene [46]. No amorphous structures were observed in the sample. Figure 3.4 c,d shows a mixture of FLG flakes/soot particles. Here, the low microwave power likely caused lower temperatures in the post-plasma zone of the reactor, known to have a strong effect on particle morphology [64], resulting in the formation of some amount of amorphous soot nanoaggregates (indicated with arrows) along with the FLG flakes. The aggregates consisted of primary spherical particles with diameters of 20–40 nm.

Several studies showed that higher total carbon concentration in the post-plasma region, which is achieved by a higher precursor flow rate, shifts the reaction toward soot formation [55,61,67]. Hence, the morphology of two samples obtained using different ethanol flow rates was analyzed here: 190 sccm (Figure 3.4 a,b) and 400 sccm of ethanol at 1.4 kW (Figure 3.4 e,f). Figure 3.4 e,f shows that along with the FLG flakes a significant amount of soot particles with diameters of 20–40 nm was produced. Hence, the TEM analysis confirms that at least two conditions

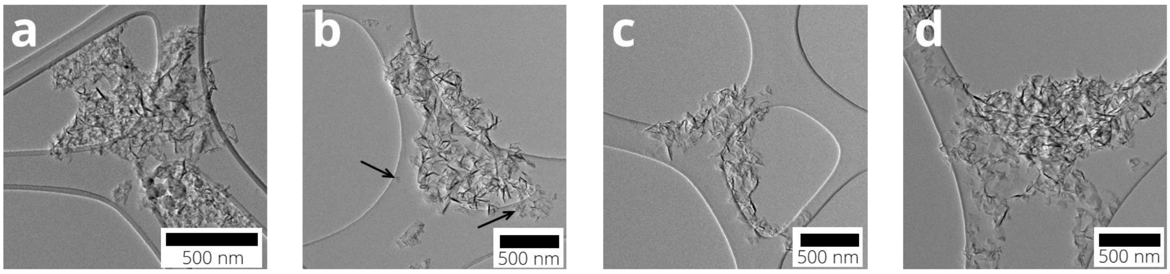

Figure 3.5 TEM images of carbonaceous particles synthesized from mixtures of C_2H_4/H_2O at different ratios (Cases 3–6): (a) Case 3, 190 sccm of C_2H_4, FLG/soot mixture; (b) Case 4, 190 sccm of C_2H_4 and 95 sccm of H_2O, FLG/soot mixture, soot particles are shown with arrows; (c) Case 5, 190 sccm of C_2H_4 and 190 sccm of H_2O, mostly FLG; (d) Case 6, 190 sccm of C_2H_4 and 285 sccm of H_2O, pure FLG. All experiments were using 1.4 kW microwave power.

should be satisfied to produce pure FLG material: sufficient temperatures in the reaction zone (typically higher than 2500–3000 K), and an ambient elemental carbon concentration below a certain process-dependent threshold value.

Figure 3.4 g,h shows spherical 20–40-nm diameter soot particles obtained in Case 2 using 54.3 sccm toluene at 1.4 kW microwave power. Such a flow rate of toluene results in a similar carbon concentration in the reactor as 190 sccm of ethanol, ~6800 ppm. However, unlike in the case of ethanol, no graphene flakes were formed. Previously, it was showed that if the precursor molecule contains oxygen atoms, e.g., ethanol (C_2H_5OH), one of the dissociation by-products is CO [55]. Due to the formation of CO molecules, the total carbon concentration in the post-plasma region decreases, which shifts the reaction toward graphene formation. Here, the correlation between concentration of oxygen-containing precursor and particle morphology is examined by using precursor combinations of C_2H_4/H_2O, where the H_2O content was varied, as shown in Table 3.1.

The TEM images in Figure 3.5 show that with increasing amounts of water added to the reactant mixture, the reaction shifts toward pure FLG formation, or rather, the formation of soot particles is suppressed. However, these investigations are qualitative, while the goal of this work is to quantify the effect of gaseous species formation, e.g., CO and others, on particle morphology, using *in situ* diagnostics, such as the FTIR spectroscopy discussed in Chapter 6.

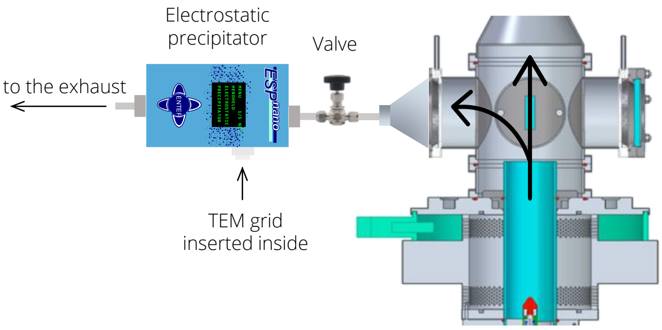

Figure 3.6 Flakes sampling scheme when using an electrostatic precipitator. Arrows inside the reactor denote the aerosol flow directions.

Additional aerosol samples were collected directly from the reactor using an electrostatic precipitator (Dash Connector Technology Inc., ESPnano model 100), which was connected to the reactor's cross-piece with an adapter, as shown in Figure 3.6. The ESPnano consists of a compact pump that sustains the aerosol flow through the device, two electrodes, which create a strong electric field to charge the flowing flakes, and a TEM grid substrate to sample the flakes [68]. Hence, no sample preparation steps, such as dispersing flakes in a solvent, sonication, and drop-casting on a TEM grid were necessary. The flakes were collected onto a 300-mesh copper grid with a carbon support film and analyzed with SEM.

Figure 3.7 a–d shows low- and high-resolution SEM images of FLG flakes produced from 190 sccm of ethanol (Case 1) and collected from the reactor using the electrostatic precipitator. Most of the flakes appear to be crumpled FLG with no apparent morphological differences from the flakes harvested as a powder from the filter (Figure 3.4 a,b). Figure 3.7 e shows the corresponding lateral size distribution, i.e., maximum Feret diameter. The histogram was fit using log-normal distribution to yield count median diameter (CMD) of 292 nm and geometric standard deviation (GSD) of 1.52. Almost no micrometer-size flakes were detected. The aspect ratio of the flake was also measured, defined as the ratio of major to minor axes of the closest-fitting ellipse that circumscribes the flake. The geometric mean aspect ratio was found to be 1.31 with a GSD = 1.14 (Figure 3.7 f).

Since TEM and SEM images indicated the crumpled nature of the FLG flakes, it was decided to analyze one sample directly collected from the reactor with tomographic TEM in collaboration with the Canadian Centre for Electron Microscopy at McMaster University and visualize the three-dimensional morphology of the flake. The typical graphene sample synthesized from 190 sccm of ethanol (Case 1) was chosen for the analysis. The TEM grid holder was tilted by step-angles of 2° between −60° to +70° relative to the normal. Figure 3.8 shows TEM micrographs

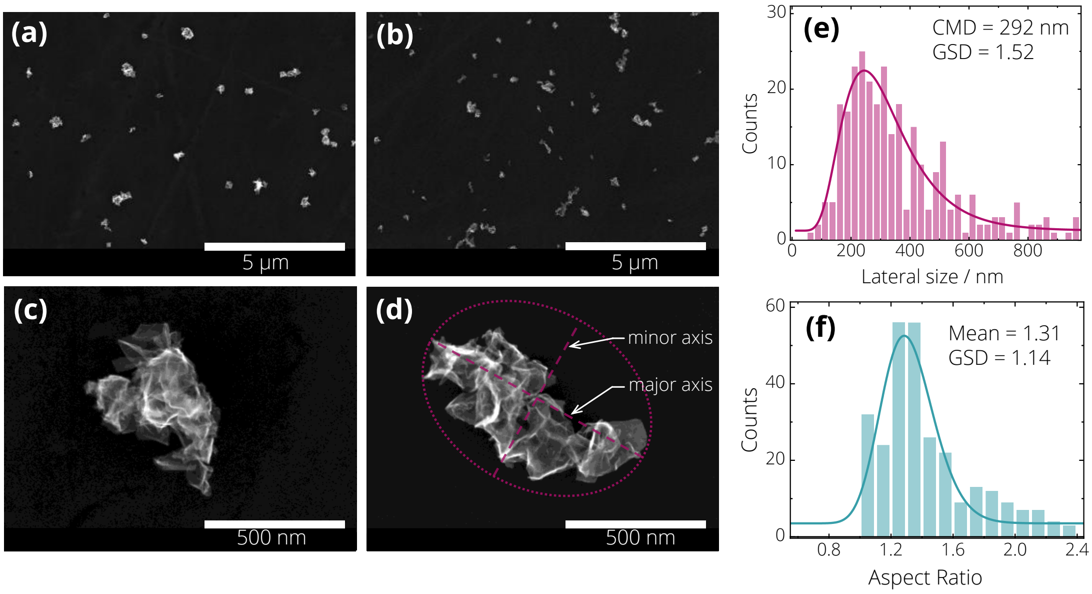

Figure 3.7 (a–d) SEM micrographs of FLG flakes (Case 1) sampled from the reactor with an electrostatic precipitator (no sample preparation); (e) corresponding lateral size histogram; (f) corresponding aspect-ratio histogram. The lateral size was measured as the major axis of an ellipse circumscribing the flake (maximum Feret diameter). The aspect ratio was measured as the ratio of major to minor axes of the ellipse. The solid lines denote the log-normal fits to the histograms. CMD: count median diameter, GSD: geometric standard deviation.

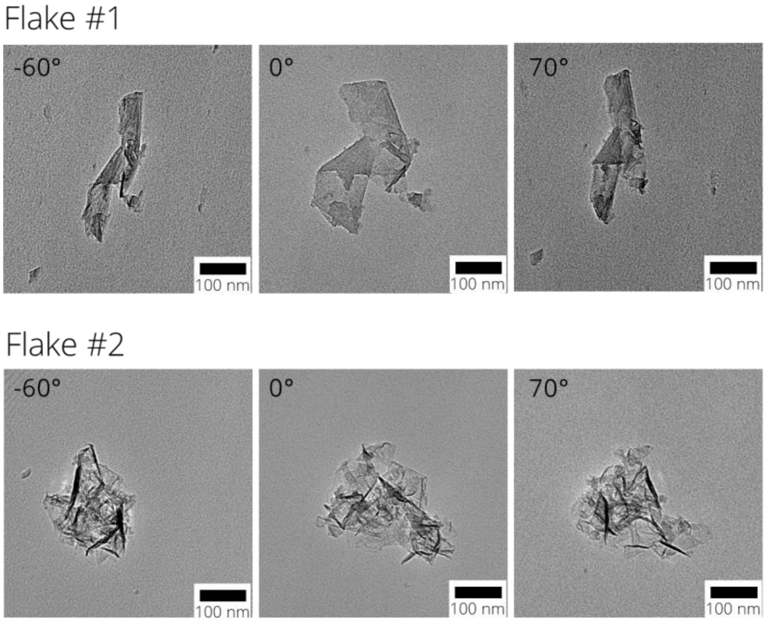

Figure 3.8 TEM micrographs of FLG flakes synthesized from 190 sccm of ethanol (Case 1) at three viewing angles. Most flakes were found to be crumpled thus having a 3D structure. The only flat (but folded) flake found during the analysis is labeled as Flake #1.

of two FLG flakes at three viewing angles. Flake #1 shows the single flat flake that was found during an hour of grid scanning, which confirms the initial observation that most of the flakes are crumpled. Flake #2 represents a typical for this type of synthesis crumpled FLG flake resembling a randomly folded pieces of paper.

3.3.2 Raman spectroscopy

Raman spectroscopy is an analytical technique used to measure vibrational energy modes of a sample. The sample is irradiated with monochromatic light, and the inelastically scattered light is then imaged into a spectrometer to obtain Raman spectra that give information about the vibrational modes in the sample. Raman spectroscopy is commonly used to identify molecules and materials, evaluate chemical and structural characteristics of a sample. In the case of graphene, Raman spectroscopy is used to determine doping levels, distinguish graphene from graphite and graphene oxide, identify the number of layers for AB Bernal stacked graphene, and assess the general quality of a sample in terms of defects [69,70].

The Raman spectra of graphene typically consist of three bands: D, G, and 2D. The G band (~1585 cm^{-1}) represents the stretching mode of the sp^2 carbon–carbon bond. The D band (~1350 cm^{-1}) is activated by defects and hence indicates the degree of structural disorder, such as the presence of amorphous material or functional groups in the sample, which can be estimated when used in combination with the G band [70]. The graphene sheet edges, if present in the area illuminated with the laser, will contribute to the D band as well. The 2D band (~2700 cm^{-1}) is the second-order of the D band, which is sensitive to the degree of graphitization.

Here, Raman spectroscopy (Renishaw inVia) was used to assess the quality of the synthesized graphene and other carbonaceous materials. A small amount of powder harvested from the filter was pressed on a glass slide and the Raman spectra were obtained for at least two spatial positions to probe the local variation across the sample. The measurements were performed at room temperature and in an ambient atmosphere between 300-3200 cm^{-1}.

The laser excitation wavelength was 532 nm, with a laser spot of 10 µm, and an 1800 line/mm grating was used in the spectrometer. The laser intensity was chosen to be smaller than 100 W/cm^2, corresponding to an incident power of 0.075 mW to prevent excessive sample heating.

Figure 3.9 shows Raman spectra of the synthesized powders. The D, G, and 2D bands are observed in all samples with additional features present, such as D′ and overtones D + D″ and D + D′. The samples were classified based on the peak positions, widths, and band area ratios that correlate with the degree of graphitization, structural disorder, and stacking order [69,71,72].

Figure 3.9 a highlights the influence of microwave power and the precursor's chemical composition on the final particle structure. The sample obtained from 190 sccm of ethanol at 1.4 kW produced the Raman spectrum (pink) typical for pure FLG [55,66]. The small $A_D/A_G = 0.83$ peak area ratio indicates a low degree of structural disorder and the large $A_{2D}/A_G = 2.03$ ratio suggests a high degree of graphitization [69]. Based on the position and the width of the 2D band signal (2696 cm^{-1}, FWHM 58 cm^{-1}) and its single-Lorentzian line shape, it can be concluded that the sample consists of turbostratic material, i.e., disorderly stacked graphene layers, which makes layer-counting difficult [69,71]. The spectrum of the sample produced from 190 sccm of ethanol at 1.0 kW (orange) corresponds to the FLG/soot particles mixture. The $A_D/A_G = 1.19$ ratio is higher than that of the pure FLG sample, which indicates a higher degree of structural disorder. The relatively low $A_{2D}/A_G = 1.07$ ratio shows a lower degree of graphitization compared to the pure FLG sample. Also, the broad overlapping D and G bands indicate the presence of soot particles in the powder. Finally, the sample produced from 54.3 sccm of toluene at 1.4 kW shows a typical Raman spectrum of soot (green) with overlapping D and G bands and no 2D peak [72]. The band positions and widths suggest the presence of amorphous structures with no graphene flakes.

Figure 3.9 b demonstrates the influence of ethanol flow rate, i.e., the elemental carbon concentration in the reactor, on the particle structure. The A_D/A_G ratios increase with ethanol flow rate, indicating the increasing degree of the structural disorder with higher carbon concentration. The A_{2D}/A_G ratios, on the other hand, decrease

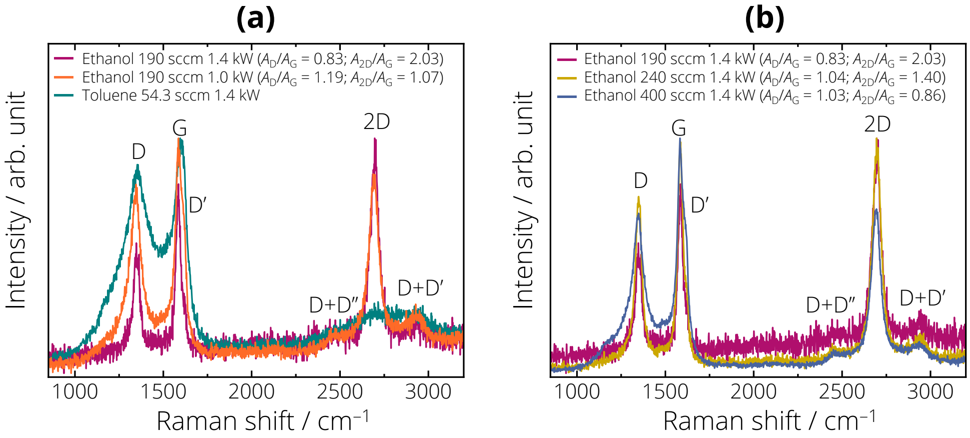

Figure 3.9 Raman spectra of synthesized powder samples. Samples were classified based on the peak positions, widths, and area ratios. (a) Ethanol 190 sccm at 1.4 kW: Highly structured turbostratic FLG; ethanol 190 sccm at 1.0 kW: Mixture of FLG flakes/soot particles; toluene 54.3 sccm at 1.4 kW: Soot particles. b) Ethanol 190 sccm at 1.4 kW: Highly structured FLG; ethanol 240 sccm at 1.4 kW: Mostly FLG flakes with small amounts of soot particles; ethanol 400 sccm at 1.4 kW: Mixture of FLG flakes/soot particles.

with the ethanol flow rate, which suggests the reducing degree of materials graphitization with increasing carbon concentrations. Moreover, in the case of 400 sccm of ethanol, the D and G bands overlap, which corresponds to the presence of amorphous soot structures in the sample. The spectra of samples produced from C_2H_4/H_2O can be found in the recent work [55]. In short, Raman spectroscopy confirmed the results derived from TEM observations (Figure 3.5) that the addition of H_2O to the reactant mixture suppresses the formation of soot particles, i.e., increases process selectivity towards graphene.

3.3.3 X-ray photoelectron spectroscopy

X-ray photoelectron spectroscopy (XPS) is a surface-sensitive analytical technique that deploys a photoelectric effect, i.e., a sample is irradiated with an X-ray beam, and the released photoelectrons are analyzed according to their kinetic energy. XPS is used to identify and measure the elemental composition of a sample surface down to a thickness of a few nanometers, assuming that all components are distributed homogeneously.

In the case of carbon nanomaterials, XPS can be used to determine the hybridization of carbon and presence of oxygen and other impurities. For example, pure graphene should show a single C1s peak of sp^2 carbon, which has a binding energy ~284 eV. Pure diamond sample, on the other hand, should demonstrate a C1s peak corresponding to sp^3 carbon with binding energy ~285 eV [73].

Here, XPS (PHI 5000 Versaprobe II, PHI Inc.) was used to assess the degree of the FLG flakes oxidation. Binding energies were measured at room temperature with a monochromatic Al-K_α source at $h\nu = 1486.6$ eV at a 45° incidence angle. The measured spectra were interpreted with the Casa XPS software.

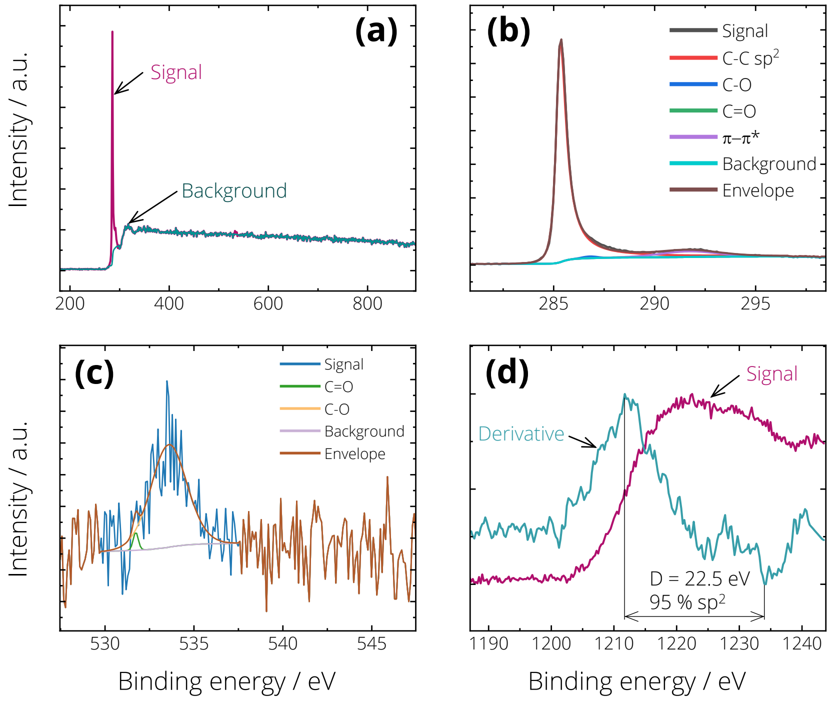

Figure 3.10 Typical XPS spectrum of FLG flakes synthesized from 190 sccm of ethanol at 1.6 kW microwave power. (a) low resolution scan; (b) high resolution O 1s region; (c) high-resolution C1s region; (d) C KLL Auger region and the D parameter calculation.

Figure 3.10 shows the low-resolution XPS spectrum of an FLG sample and high-resolution spectral regions of O 1s, C 1s, and C KLL. A Shirley-type background was calculated and subtracted before the fitting. The C 1s region was fitted with signals corresponding to C–C (~284 eV), C–O (C–C position + 1.2 eV), C=O (C–C position + 3.2 eV) bonds, and a peak for the π–π^* transition (~290 eV). The O 1s region was fitted with signals corresponding to C–O and C=O bonds. Peak positions were assigned following the data from Briggs et al. [73]. A line shape, which is a 70/30 ratio of Gaussian and Lorentzian functions convolution, was used to fit all peaks, except for the C–C sp^2 that is known to have an asymmetric line shape [74].

The C 1s signal (Figure 3.10 b) shows no indication of significant oxidation. The overall oxygen content in the sample was calculated using the "area" method, when the area of O 1s is divided by that of C 1s, accounting for the spectral sensitivity of the device. For all the FLG samples investigated in this thesis (see Table 3.1), the overall oxygen content was estimated to be less than 2 at.% with no evidence of nitrogen bonding, verifying the chemical purity of the produced flakes.

The carbon sp^2/sp^3 hybridization ratio in the sample was estimated through the measurement of the "D parameter" based on the method demonstrated by Lascovich et al. [75]. The derivative of the C KKL region of the Auger spectrum is calculated, where the D parameter is the width of the obtained signal, i.e., the distance between the maximum and minimum in eV. In his work, Lascovich et al. demonstrated that the D value linearly depends on the sp^2/sp^3 ratio in the sample. The authors carried out a series of measurements with highly-oriented pyrolytic graphite (100 % sp^2), diamond (100 % sp^3), and samples prepared with dual ion beam sputtering having various controlled C/H ratios (hence, different sp^2/sp^3 ratios). Here, the calculated D values were ranging between 21–22.5 eV corresponding to 80–95 % of all carbon in the sample having sp^2 hybridization, which indicates that the samples consisted almost entirely of graphitic carbon with minimum incorporation of diamond or amorphous carbon. However, the sp^2/sp^3 ratio estimated in this way should be treated with caution as it relies strongly on the calibration curve, which was taken from Lascovich et al. [75] and was not repeated here. Moreover, the D parameter has shown sensitivity to the smoothing procedure and the content of oxygen and hydrogen in the sample [76,77].

3.4 Summarizing notes

This chapter described the design of the gas-phase microwave-plasma reactor, explained how freestanding FLG and other carbonaceous aerosols were synthesized, and provided detail on their *ex situ* characterization.

Raman spectroscopy confirmed that the powder was turbostratic graphene with a low degree of structural disorder, XPS showed that the FLG consisted of more than 98 atom% of carbon, over 80 % of which was sp^2 carbon, and electron microscopy revealed the crumpled flakes consisting of less than ten layers.

A parametric *ex situ* study was conducted to investigate how microwave power, type, and concentration of precursor affect particle morphology. Overall, the results indicate that insufficient temperature and excessive carbon concentration in the system result in the formation of non-structured and less-graphitized materials, e.g., soot particles. Increasing temperatures by increasing microwave power and reducing the elemental carbon concentration suppress particle formation and shift the reaction toward planar graphene structures.

It should be added that the FLG samples fabricated during this work were compared to other samples produced under similar conditions in the study by Münzer et al. [34]. The results of the TEM, XPS, and Raman analyses showed that the flakes morphology and chemical composition were consistent among the samples. The authors also deployed Fourier-transform infrared spectroscopy and X-ray diffraction to confirm the high purity and crystallinity of the gas-phase synthesized graphene.

Chapter 4
Aerosol flake morphology and optical properties

Many applications exploit the mechanical, electrical, and optical properties of graphene [20,30]. However, recent studies show that the morphology of mass-produced graphene powders and suspensions, and therefore their functionality, often differ considerably from those claimed by the manufacturer [11,45,78]. The problem of reliable characterization is even more pronounced for crumpled graphene materials, e.g., crumpled FLG aerosols, one of the most prevalent graphene products [12,79], the properties of which depend strongly on flake morphology [80–82].

Knowledge of crumpled graphene aerosol morphology is also required to understand its adverse health effects due to occupational and environmental exposure. Currently, there is little consensus on the potential hazards of graphene materials [51–54], in part due to a lack of information about its morphology [52]. Several morphological parameters must be known to predict graphene toxicity and lung deposition efficiency, including the flake lateral dimension, aerodynamic diameter, surface area, and thickness. To date, most studies that report these parameters are limited to flat graphene materials, with comparatively little information available on crumpled graphene [52,54].

Apart from the under-investigated morphology of crumpled FLG flakes, there is a lack of data on their optical properties. Knowledge of the particle optical properties, such as absorption efficiency and the single scattering albedo, is required for the interpretation of aerosol-phase measurements, e.g., laser-induced incandescence or laser absorption spectroscopy. Besides, the increasing large-scale production and use of crumpled graphene will inevitably lead to its release and accumulation in the environment. Hence, the light-absorbing characteristics of crumpled graphene should be investigated to learn if these materials might play a role in the radiative forcing, similar to highly-absorbing black carbon or soot [83]. Further complications to the matter adds the recent evidence that the optical properties of graphene flakes are size- and shape-dependent [84]. The literature search shows that the only study published on the crumpled graphene aerosol optical properties is the one by Zangmeister et al. [85], who measured the mass absorption cross-sections (MAC) of crumpled few-layer graphene aerosols with a photoacoustic spectrometer. They compared the MACs of graphene with other light-absorbing carbon aerosols, but no possible morphology dependence was investigated.

This chapter presents experimental and modeling efforts to characterize the interplay between morphology and optical properties for crumpled FLG flakes. The analysis builds up on the *ex situ* powder characterization presented in Chapter 3 and extends towards graphene in aerosol and suspension phases. It is of great importance to probe graphene properties *in situ* to avoid possible altering effects of sample collection and preparation when using *ex situ* analyses.

The chapter is organized as follows. First, the morphology of crumpled FLG aerosols is described: flake lateral size and aspect ratio, mobility and aerodynamic diameters, shape, and layer number. Next, the optical properties of crumpled FLG suspensions and aerosols are presented: wavelength-resolved extinction and absorption coefficients, mass absorption and extinction cross-sections, and the single scattering albedo. Finally, the optical properties of crumpled FLG aerosols and suspensions are modeled through Rayleigh–Debye–Gans theory and numeric discrete dipole approximation simulations based on flake geometries derived from tomographic transmission electron microscopy. The data presented in this chapter will be useful when modeling graphene health effects and interpreting optical measurements on graphene suspensions and aerosols.

4.1 Morphology measurements

The morphology of crumpled FLG flakes in the aerosol phase was measured in terms of lateral size, mobility diameter, and aerodynamic diameter. All three parameters are vital to defining the possible link between morphology and optical properties, as well as to understanding crumpled graphene aerosol toxicity and lung deposition efficiency. The particle mobility diameter (d_m) is equivalent to the diameter of a sphere having the same electrical mobility as a particle/flake of interest and is measured by the balance of electrical and drag forces. Particle aerodynamic diameter (d_{ae}) is the diameter of a sphere of density 1 g/cm^3 with the same terminal settling velocity as a particle of interest and is measured based on the balance between centrifugal and drag forces.

4.1.1 Experimental setup and methodology

Figure 4.1 shows the experimental configuration. A few milligrams of the crumpled FLG powder were dispersed in 1 liter of ethanol (≥ 99.5 % purity) and ultrasonicated for at least 15 minutes. The suspension was then nebulized using a Collison nebulizer (TSI Inc., Model 3076) in recirculation mode, with filtered air at an absolute pressure of 308 kPa as the motive gas. The nebulized crumpled FLG-ethanol aerosol then passed through a dilution column equipped with a 0.071 cm impactor (TSI Inc., long DMA column). The dilution column serves two purposes: it controls the particle number concentration and evaporates some of the ethanol [86]. The sheath-to-sample flow rate

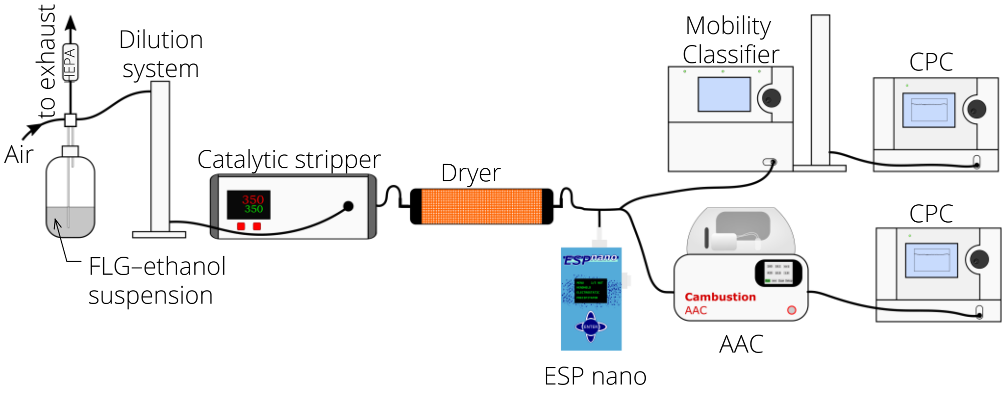

Figure 4.1 Experimental configuration used to characterize FLG aerosol flakes morphology. HEPA: high-efficiency particulate air filter, AAC: aerodynamic aerosol classifier, CPC: condensation particle counter.

ratio used in the dilution column was adjusted to 6.8 as a trade-off value to provide an acceptable signal-to-noise ratio while diluting the sample flow not to overflood the catalytic stripper.

The diluted aerosol then flowed through a catalytic stripper (Catalytic Instruments, CS10) operated at 350 °C to evaporate and oxidize semi-volatile impurities that could be present in ethanol. The oxidation reaction produces water vapor, which was removed by passing the aerosol through a diffusion dryer. The aerosol heating inside the catalytic stripper may not only remove the impurities but can potentially lead to a change in particle morphology. However, the d_m distributions measured with and without the catalytic stripper in the setup were not significantly different. Hence, the impact of heating on FLG flake morphology was negligible.

The mobility classifier in Figure 4.1 was equipped with an X-ray bipolar charger (TSI Inc., Model 3088) and consisted of an electrostatic classifier (TSI Inc., Model 3082) with a 0.071 cm impactor (D_{50} cut-point diameter 600 nm), a long differential mobility analyzer column (DMA, TSI Inc., Model 3081), and a condensation particle counter CPC (TSI Inc., Model 3776). The CPC measures particle number concentrations by condensing butanol vapors onto pre-existing particles to count them individually by laser-light scattering. The combination of a mobility classifier/CPC is known as a scanning mobility particle sizer (SMPS). The size measurement range was 15–700 nm with the sample flow of 0.32 standard liters per minute (slm) and the sheath-gas flow of 3.2 slm, resulting in a mobility-diameter resolution $R_\mathrm{d} = Q_\mathrm{sheath}/Q_\mathrm{sample} = 10$. The data were analyzed by the Aerosol Instrument Manager software (TSI Inc., AIM, ver. 10.1) that employs an inversion algorithm by Wiedensohler [87] accounting for the instrument function, diffusion losses, and multiple charging. The AAC (Cambustion Ltd.) aerodynamic size range was set to 23–570 nm with a resolution $R_\mathrm{s} = 6.7$. The AAC data were deconvoluted using the algorithm by Johnson et al. [88] implemented into the device's software.

Both the SMPS and AAC were calibrated using spherical polystyrene latex particles of known diameter prior to the experiments. To ensure the stability of the crumpled FLG–ethanol suspension, i.e., to exclude particle precipitation in the nebulizer, SMPS and AAC scans were performed multiple times before and after the measurements. The particle-number concentration and the particle-size distribution of the suspension remained stable for the several-hour duration of one day's experiments.

The devices were connected using electrically conductive carbon-impregnated silicone tubing to minimize size-dependent electrostatic particle losses that could otherwise bias the measured size distributions. Nevertheless, test measurements of particle losses were carried out by flowing the aerosol at the experimental flow rates and temperatures through tubes of different lengths and then measuring the particle number concentrations and d_m distributions with the scanning mobility particle sizer. Negligible losses were detected for particles larger than 50 nm, which pertain to crumpled FLG particles. All instrument flows were measured using a Gilibrator-2 flow standard (Sensidyne LP) and corrected for the lab temperature and pressure.

4.1.2 Results

The FLG flake-size distributions measured with SEM, SMPS, and AAC are plotted in Figure 4.2 as probability density functions along with log-normal fits to the data. It is important to keep in mind that these "diameters" incorporate information about distinct physical characteristics of a flake, according to the corresponding measurement principle, and therefore differ from each other. Furthermore, it is necessary to account for the size-dependent efficiencies of the instruments. The sampling efficiency of the ESPnano was largely size-independent [68]. The

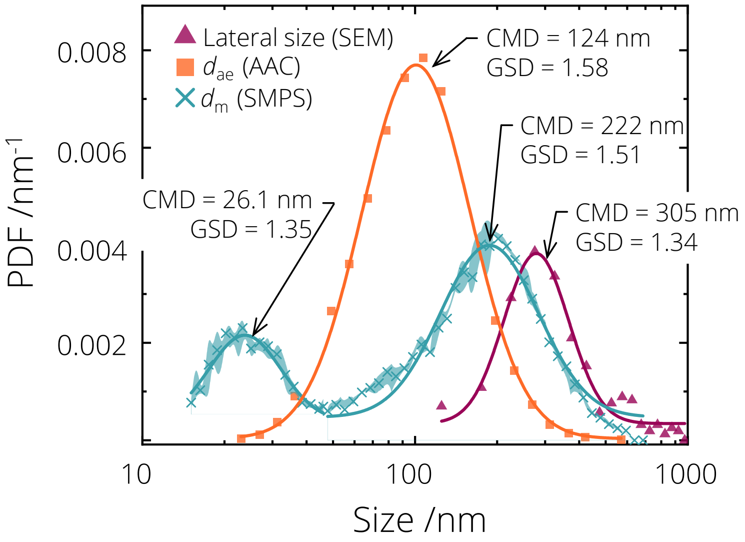

Figure 4.2 Probability density functions of the aerosolized FLG flake-size distributions: turquoise crosses: mobility diameter measured with SMPS (filled area corresponds to one standard deviation), orange squares: aerodynamic diameter measured with AAC, dark pink triangles: lateral particle size measured with SEM. Solid lines show the corresponding log-normal fits to the data. The mobility diameter data (SMPS) were split into two log-normal distributions. CMD: count median diameter, GSD: geometric standard deviation.

AAC and SMPS size-dependent corrections are included in the built-in device's software and were applied automatically during data collection [87,88].

Figure 4.2 shows that the d_m distribution is bimodal with the smaller mode having a CMD = 26.1 nm, and the larger mode having a CMD = 222 nm. The small mode likely represents the residues from organic impurities in the ethanol and not the solid graphene flakes. These impurities may have penetrated through the catalytic stripper due to the very high concentration of ethanol at its inlet (well above the suggested instrument operation range). In general, it is hard to fully avoid residues in the aerosol, as they are universally observed when nebulizing solid particles, although they correspond to a very small mass fraction in the original solution [89]. For example, assuming spherical particles of equal density and a median nebulizer droplet size of 300 nm (as per the nebulizer manual [90]), the observed 26.1 nm particles would represent an impurity of only 660 ppm in the solution.

The d_{ae} distribution (orange squares) is unimodal and does not show the volatile particle mode. That could be explained when considering different physical principles underlying the AAC and SMPS operation. For non-spherical particles, $d_m = d_{ae} \times const$, where $const > 1$ and depends on particle shape and density [91]. Assuming that both devices measure the FLG flakes without altering their morphology, the corresponding size distributions should be proportional to each other. When the d_m density distribution is limited to the larger mode only (solid FLG flakes), d_{ae} is multiplied by a constant so that its density peak matches the d_m density peak (here, ~1.8), and both density distributions are re-normalized so that their areas equal unity, they match exactly, which proves the assumption. Hence, the AAC detection range of 23-570 nm corresponds to the d_m range of approximately 40-1040 nm, and therefore, only the larger solid flakes mode was observable when using the AAC.

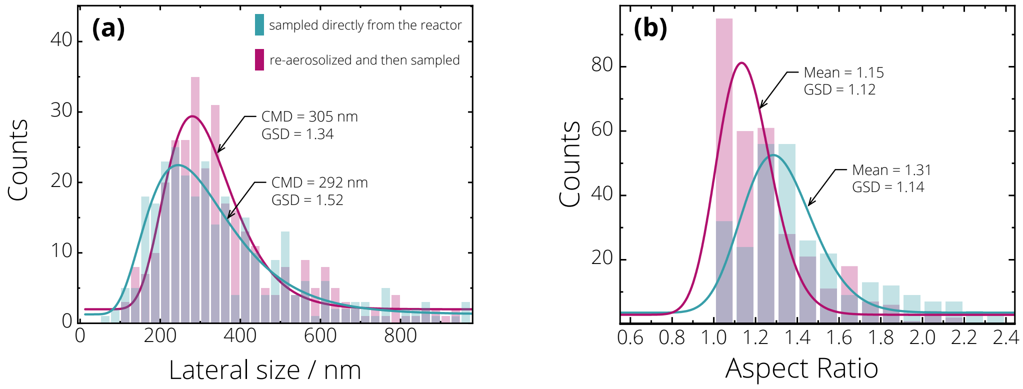

Figure 4.3 (a) Lateral size and (b) aspect-ratio histograms of FLG flakes sampled from the reactor and after re-aerosolization. The solid lines denote the log-normal fits to the histograms. CMD: count median diameter, GSD: geometric standard deviation. The aerosolization procedure did not cause changes in flake size but slightly decreased the flake aspect ratio.

To ensure that the aerosolization procedure (nebulizing, heating, and drying) does not impact the flake morphology, an aerosol sample was collected on a TEM grid using an electrostatic precipitator (ESP nano model 100) that was installed inline after the diffusion dryer using a T-piece as shown in Figure 4.1. The collected sample was then analyzed in terms of flake lateral size and aspect ratio derived from SEM measurements (Hitachi Inc., S-5200, operated at 30 kV). The results were compared with the sample collected from the reactor (Section 3.3.1). Figure 4.3 a shows that the flake lateral size, i.e., the maximum Feret diameter, did not change significantly during aerosolization. However, the aspect ratio was slightly reduced (Figure 4.3 b), i.e., the flakes became a bit more compact. That could be explained by the effect of the surface tension of ethanol during droplet evaporation. It should be also noted that these aspect ratios are not large enough to result in preferential orientation of the FLG flakes inside the electrostatic classifier [92,93], which would influence their mobility diameter measurements.

The graphene aerosol size distributions can be translated into the respiratory deposition fractions following the simplified equations by Hinds [94]. The Equations (4.1)-(4.3) were fitted to the semi-empirical models by the International Commission on Radiological Protection [95] for monodisperse spheres of standard density (1000 kg/m^3) at standard conditions, and averaged for males/females at three exercise levels. For non-spherical particles of arbitrary density, such as crumpled FLG flakes, d_{ae} is used instead of physical particle diameter to reproduce the aerodynamic behavior of standard aerosols. In that case, the equations are the following:

$$\mathrm{DF_{HA}} = 1 - 0.5\left(1 - \frac{1}{1 + 0.00076 d_{\mathrm{ae}}^{2.8}}\right)\left(\frac{1}{1 + \exp\left(6.84 + 1.183 \ln d_{\mathrm{ae}}\right)} + \frac{1}{1 + \exp\left(0.924 - 1.885 \ln d_{\mathrm{ae}}\right)}\right) \tag{4.1}$$

$$\mathrm{DF_{TB}} = \left(\frac{0.00352}{d_{\mathrm{ae}}}\right)\left[\exp\left(-0.234\left(\ln d_{\mathrm{ae}} + 3.4\right)^2\right) + 63.9 \exp\left(-0.819\left(\ln d_{\mathrm{ae}} - 1.61\right)^2\right)\right] \tag{4.2}$$

$$\mathrm{DF_{AL}} = \left(\frac{0.0155}{d_{\mathrm{ae}}}\right)\left[\exp\left(-0.416\left(\ln d_{\mathrm{ae}} + 2.84\right)^2\right) + 19.11 \exp\left(-0.482\left(\ln d_{\mathrm{ae}} - 1.362\right)^2\right)\right], \tag{4.3}$$

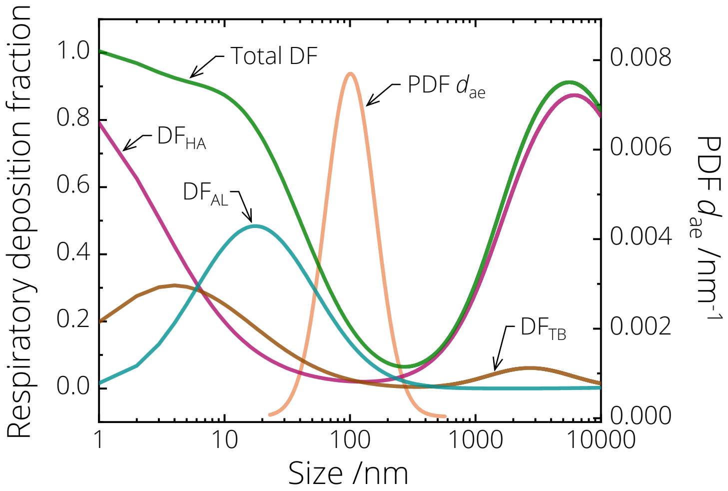

Figure 4.4 Respiratory deposition fractions, total and regional, versus particle size. Curves were calculcated using simplified equations by Hinds [94]. DF: deposition fraction; HA: head airway; TB: tracheobronchial region; AL: alveolar region. PDF d_{ae} is probability density function of crumpled FLG aerodynamic diameter. Between 10-40 % of crumpled FLG flakes are predicted to deposit in respiratory ways, most of the flakes reaching alveolar region.

where DF stands for deposition fraction, i.e., a fraction of inhaled particles that is deposited in a certain respiratory region; HA is head airways, which includes the nose, mouth, pharynx, and larynx; TB is the tracheobronchial region, which includes the airways from the trachea to the terminal bronchioles; AL is the lowest part of the lungs or alveolar region.

The calculated respiratory deposition fractions and the d_{ae} probability density function are shown in Figure 4.4. The "Total DF" curve corresponds to the sum of all three deposition fractions. Hence, when "Total DF" < 1, part of the inhaled particles is exhaled without depositing inside the respiratory ways. For crumpled FLG flakes investigated here, 68% of the flakes have d_{ae} between 60 and 170 nm. In that size region, between 10–40 % of inhaled particles are predicted to deposit in respiratory ways, mostly reaching the alveolar region. Nanoparticles accumulated in the deep lung might penetrate the bloodstream and cause adverse health effects [96]. It should be noted that the analysis presented here is overly simplified and averaged for various conditions. Nevertheless, a thorough experimental study on graphene aerosol deposition in the human upper respiratory ways (here denoted as HA and TB) reported similar low deposition fractions for graphene flakes with d_{ae} = 50–150 nm [97]. Authors concluded that graphene flakes, when inhaled, are likely to reach low regions of lungs and accumulate. However, the understanding of toxic effects is incomplete without long-term studies on toxicity and biodegradability of crumpled FLG flakes, which is beyond the scope of this thesis but has been addressed in recent reviews [52,53].

4.2 Optical properties measurements

The optical properties measured and reported in this section describe the interaction of crumpled FLG flakes with light. The following optical properties of FLG flakes in the aerosol phase were measured: wavelength-resolved extinction and absorption coefficients, wavelength-resolved mass absorption cross-section, absorption Ångström exponent, and the single scattering albedo. These quantities are commonly used in aerosol research for characterizing carbonaceous aerosols. The extinction ($b_{\mathrm{ext},\lambda}$) and absorption ($b_{\mathrm{abs},\lambda}$) coefficients are used to describe the absolute magnitude of light extinction and absorption by an aerosol. The mass absorption cross-section (MAC_{λ}) is the particle absorption cross-section per unit mass of a material, which is widely used in atmospheric research to calculate the effect of soot on the climate. The absorption Ångström exponent (AAE) was first introduced by Ångström in 1929 [98] to describe the spectral variation of the light extinction by aerosols. Since then, the AAE has been shown to be sensitive to particle morphology and chemical composition, i.e., molecular structure [99–101]. Thus, it is commonly used to characterize an aerosol type. For example, the AAE of small soot particles is usually close to unity while the AAE of light-absorbing organic aerosols usually exceeds unity [102]. The single scattering albedo (SSA) is the ratio of scattering to extinction, which shows what fraction of extinction is due to scattering. Values close to unity would suggest strong aerosol scattering and consequently low absorption.

The measurement results presented in this section were compared with optical properties of other carbonaceous aerosols, and obtained spectroscopic data were additionally used to extract morphological parameters of graphene flakes based on the existing metrics.

4.2.1 Experimental setup and methodology

Figure 4.5 shows experimental configurations used to characterize FLG aerosol optical properties. The setup in Figure 4.5 a was used to measure the aerosol $b_{\mathrm{abs},\lambda}$ using an aethalometer (Magee Scientific, Model AE33). The setup

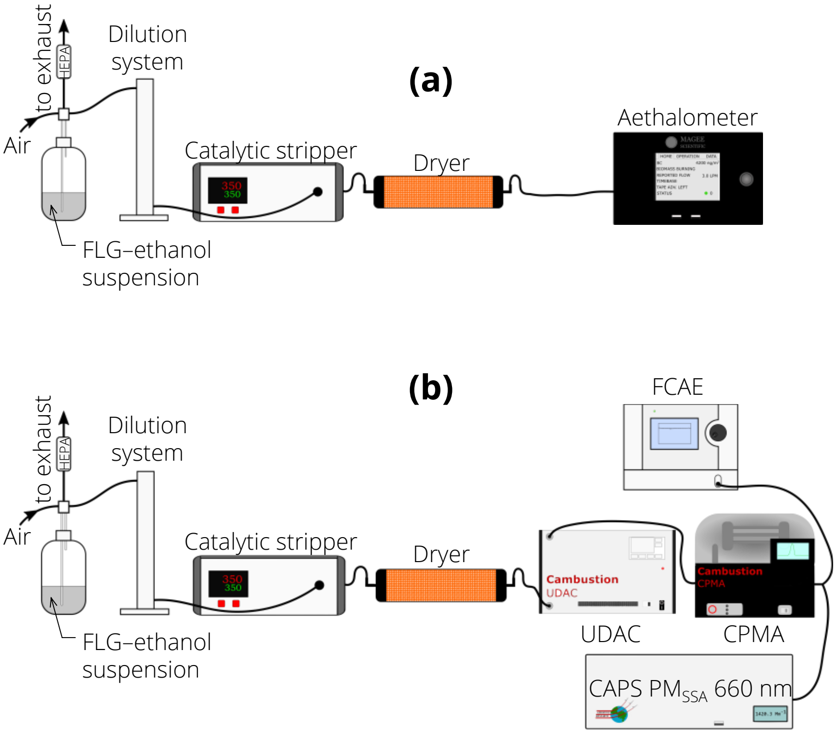

Figure 4.5 Experimental configurations used to characterize FLG aerosol optical properties. HEPA: high-efficiency particulate air filter, UDAC: unipolar diffusion aerosol charger, CPMA: centrifugal particle mass analyzer, FCAE: Faraday-cup aerosol electrometer, CAPS $\mathrm{PM}_{\mathrm{SSA}}$: cavity-attenuated phase-shift particulate matter SSA monitor.

in Figure 4.5 b was used to measure the aerosol absorption coefficient at 660 nm, $b_{\mathrm{abs},660}$, using a cavity attenuation phase-shift particulate matter single-scattering-albedo monitor (CAPS $\mathrm{PM_{SSA}}$, Aerodyne Inc., Model 660 nm) and the FLG mass absorption cross-section at 660 nm (MAC_{660}). Additionally, the $b_{\mathrm{ext},\lambda}$ was measured with a UV-Vis spectrophotometer (Varian Inc., Cary 4000) for the 0.0005 wt.% FLG–ethanol suspension (4 mg FLG per 1 liter ethanol).

The CAPS $\mathrm{PM_{SSA}}$ is an optical extinction and scattering monitor that measures the phase shift in a modulated light beam due to scattering and extinction. The CAPS $\mathrm{PM_{SSA}}$ is a well-characterized tool for the measurement of aerosol light absorption [103,104] but it does not provide spectral information. The CAPS $\mathrm{PM_{SSA}}$ monitor used in this thesis utilizes a light-emitting diode centered at 660 nm, a sample cell with an integrating-sphere nephelometer, and a vacuum photodiode detector. The particulate extinction coefficient is determined by subtracting the aerosol signal from a filtered (gas-only) signal. The extinction measurement is calibration-free, with a manufacturer-estimated accuracy of 5 % [103]. Aerosol light scattering is measured simultaneously in the integrating sphere and was calibrated before and after the experiments using an aerosol of 200 nm diameter ammonium sulfate particles. The absorption coefficient is found from the difference between extinction and scattering coefficients.

In the aethalometer, the aerosol sample is deposited on a filter tape and irradiated. In contrast to the single-wavelength CAPS $\mathrm{PM_{SSA}}$, the aethalometer utilizes seven LEDs centered at wavelengths ranging from 370 to 950 nm and can be calibrated in real-time using the CAPS $\mathrm{PM_{SSA}}$. The light transmitted through the particle-laden filter relative to the clean filter is measured and used to calculate the light extinction coefficient of the sample via the Beer-Lambert law.

The extinction coefficient measured with the aethalometer, $b_{\mathrm{ext},\lambda}$, represents the light absorption by a thin layer of particles deposited near the filter surface, multiple scattering by the fibers within the filter, and light scattering by the particles on the tape. However, the calculated $b_{\mathrm{ext},\lambda}$ can be corrected to the $b_{\mathrm{abs},\lambda}$. Light scattering by the particles is considered to be negligible compared to light absorption, as shown for purely scattering aerosols sampled on filters [105–107]. Hence, the $b_{\mathrm{ext},\lambda}$ can be converted to an absorption coefficient $b_{\mathrm{abs},\lambda}$ by accounting for multiple scattering with a correction factor, the C-value [106] that should be calibrated for each new sample and filter [108]. In this work, the C-value was calibrated using the aethalometer-measured $b_{\mathrm{ext},660}$ and CAPS $\mathrm{PM_{SSA}}$-measured $b_{\mathrm{abs},660}$, as $C = b_{\mathrm{ext},660} / b_{\mathrm{abs},660} = 2.17 \pm 0.23$, slightly smaller than the manufacturer's default value of 2.56 [108]. The C-value has been extensively studied in the literature and shown to be largely wavelength-independent [105,106,108]. Apart from multiple scattering, a "filter loading effect" can affect the $b_{\mathrm{ext},\lambda}/b_{\mathrm{abs},\lambda}$ relationship. With the continuous accumulation of aerosol particles on the filter tape, the particles absorb a higher fraction of scattered light, which leads to underestimated extinction coefficients for filters with higher particle loading compared to filters with low loading [106] or a so-called the "filter loading effect" [109]. The AE33 aethalometer used here corrects for this effect in real time by using a dual-spot technique, in which the extinction is continuously measured in two spots on the filter tape, with the aerosol sampled at different sample flows [109]. Hence, the aethalometer-measured $b_{\mathrm{ext},\lambda}$ is proportional to $b_{\mathrm{abs},\lambda}$.

The wavelength-resolved $b_{\mathrm{abs},\lambda}$ data allow calculating the AAE, which defines the wavelength power-law dependence of the $b_{\mathrm{abs},\lambda}$:

$$b_{\mathrm{abs},\lambda} \propto \lambda^{-\mathrm{AAE}}. \tag{4.4}$$

In the case of particles that absorb and emit in the Rayleigh regime, i.e., $\pi d_\mathrm{p} << \lambda$ and $\mathbf{m}_\lambda d_\mathrm{p} << \lambda$, the spectral dependence of the aerosol absorption is usually expressed as

$$b_{\mathrm{abs},\lambda} \propto \frac{E(\mathbf{m}_\lambda)}{\lambda}, \tag{4.5}$$

where

$$E(\mathbf{m}_\lambda) = \mathrm{Im}\left[\frac{\mathbf{m}_\lambda - 1}{\mathbf{m}_\lambda + 2}\right] \tag{4.6}$$

is the absorption function, d_p is the particle diameter, and $\mathbf{m}_\lambda$ is the complex refractive index of the material.

4.2.2 Results

Figure 4.6 shows $b_{\mathrm{ext},\lambda}$ measurements of the FLG–ethanol suspension and $b_{\mathrm{abs},\lambda}$ of the filter-deposited FLG aerosol, as measured by UV-Vis spectroscopy and with the aethalometer, respectively. The data are normalized to 660 nm to enable the comparison.

The UV-Vis extinction peaks at 269 nm, which corresponds to π-π* electronic transitions of graphitic C=C bonds and is commonly observed for graphene [110,111]. In the case of graphene oxide, the extinction peak blue-shifts to ~230 nm [111]. The normalized UV-Vis and aethalometer data agree well in the visible part of the spectrum (although admittedly in part due to the normalization), while they considerably vary in the UV. This is

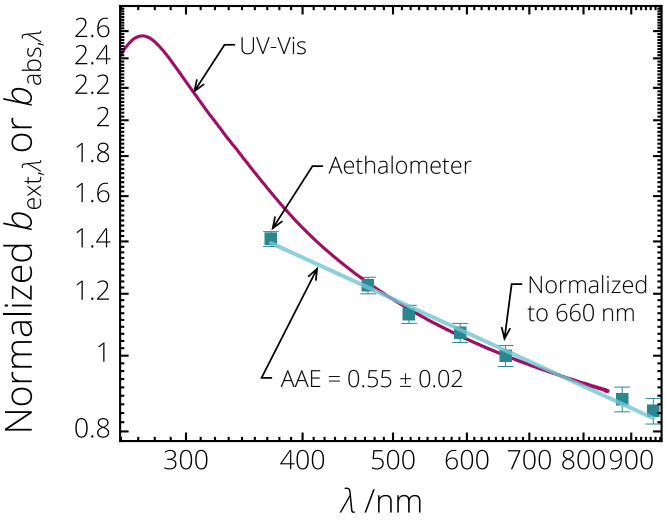

Figure 4.6 Wavelength-dependent extinction coefficient ($b_{\mathrm{ext},\lambda}$) of an FLG–ethanol suspension measured by UV-Vis spectroscopy, and absorption coefficient ($b_{\mathrm{abs},\lambda}$) of filter-deposited FLG aerosol measured with an aethalometer. The error bars denote one standard deviation of the mean. The blue straight line labeled as AAE is the linear fit to the aethalometer data. Both datasets are normalized to 660 nm.

likely due to the increasing contribution of particulate light scattering to the $b_{\mathrm{ext},\lambda}$ signal at shorter wavelengths, which was not compensated for in the UV-Vis measurements.

The wavelength-independent AAE = 0.55 ± 0.02 was calculated via a linear fit to the logarithmic aethalometer data shown in Figure 4.6. This is substantially different from the AAE = 1.0 ± 0.2 of mature soot particles [102,112], which, assuming the Rayleigh regime and according to Equations (4.4) and (4.5), would lead to the constant $E(\mathbf{m}_\lambda)$ over the measurement wavelength range. For crumpled FLG flakes in the Rayleigh regime, the AAE = 0.55 would indicate a strong wavelength dependence of $E(\mathbf{m}_\lambda) \propto \lambda^{0.45}$ in the λ range of 370–950 nm. Since the AAE parameter is sensitive to aerosol particle morphology and chemical composition, e.g., multiple particle-particle scattering within an aggregate and the presence of coatings [99,102,113], it is important to understand which changes to the flakes could be induced by the aerosolization procedure. In Section 3.1.2, it was demonstrated that the flakes are slightly more compact after aerosolization. Liu et al. [99] used numerical simulations to show that more compact soot aggregates have smaller AAE values. Here, the chemical composition of FLG flakes after the aerosolization was not analyzed albeit precautions were taken to minimize amounts of ethanol and potential impurities in the aerosol (catalytic oxidation and diffusion drying). Thus, it is unclear if the AAE of wet-aerosolized crumpled graphene can be considered in analogy to graphene aerosol inside the reactor. For that reason, until either chemical composition analysis of aerosolized flakes is available or *in situ* gas-phase measurements without aerosolization steps are done, we restrain from using wavelength-dependent $E(\mathbf{m}_\lambda)$ on crumpled FLG aerosols.

The obtained spectroscopic data also allows extracting several morphological parameters of graphene, following the established metrics from Backes et al [114]. The authors used a UV-Vis spectrometer equipped with an integrating sphere to measure wavelength-resolved extinction and scattering coefficients of size- and layer-number-selected graphene suspensions. They found that the extinction peak position and curvature of the spectra depend on the lateral size and graphene layer number. The correlations were found to be robust when tested against lab and commercial suspensions, different solvents and stabilizers, and sheets with different stacking orders. However, Backes et al. [114] worked with relatively stiff (and thus) flat graphene nanosheets produced from graphite exfoliation, while here, crumpled 3D-like FLG flakes are analyzed.

First, the mean graphene layer number is extracted from the extinction spectra. The metrics for layer number $\langle N \rangle$ was established by Backes et al. [114] using the ratio of the peak extinction coefficient to its asymptotic value in the long-wavelength region: $\langle N \rangle \pm 15\,\% = 25\ b_{\mathrm{ext},550}/b_{\mathrm{ext,peak}} - 4.2$, which in this case yields $\langle N \rangle = 6.55 \pm 0.98$. The graphene layer number can also be estimated using the extinction peak position: $\langle N \rangle = 0.81\ \lambda_{\mathrm{ext,peak}} - 213$, which results in $\langle N \rangle = 4.89$. Hence, the UV-Vis data analysis suggests a mean graphene layer number of 5–8, which is in good agreement with the TEM results. In particular, high-resolution TEM showed that most of the flakes are thinner than ten graphene layers, and Brunauer–Emmett–Teller (BET) analysis yielded the specific surface area (normalized to material's mass) of 300–400 m^2/g [66], which corresponds to 7–9-layer flat graphene nanosheets calculated as $N = 2/(\rho d S)$, where ρ is the graphite density (2.267×10^6 g/m^3), d is the interlayer spacing (0.34×10^{-9} m), and S is the specific surface area.

The UV-Vis extinction curve was also used to estimate the mean lateral size of the flakes. Although the UV-Vis measurement corresponds to the extinction (absorption + scattering) coefficient, Backes et al. [114] showed that for the exfoliated flat FLG, the absorbance in the region 650–800 nm was largely wavelength-independent and independent of flake size. Hence, any wavelength dependence of the extinction curve at wavelengths longer than

650 nm is mainly due to scattering, and the scattering exponent can be estimated from the extinction exponent, i.e., $b_{\mathrm{ext},\lambda} \propto \lambda^{-n}$, and the corresponding flake lateral size found as $\langle L \rangle = (n/2.466)^{-3.05}$. Following their proposed approach, we fit the extinction curve with a power law in the long-wavelength region, $\lambda^{-0.434}$, and estimated the FLG lateral size as $\langle L \rangle = (0.434/2.466)^{-3.05} \approx 200$ nm, which is within one standard deviation of the count-median lateral size measured by SEM (305 nm), as shown in Figure 4.2. This discrepancy may relate to the assumption of a wavelength-independent absorbance spectrum (the aethalometer data suggest that the absorbance in the longer wavelength region is not flat, Figure 4.6). This comparison shows that UV-Vis spectroscopy metrics established for FLG suspensions can give reasonable estimates of the flake mean layer number and lateral size.

MAC measurements were conducted using a setup configuration shown in Figure 4.5 b. The CAPS $\mathrm{PM_{SSA}}$ monitor was deployed to measure the $b_{\mathrm{abs},660}$ of the FLG aerosol, and a CPMA-Electrometer Reference Mass System (CERMS) designed at the Metrology Lab of the National Research Council Canada [115] was used to generate FLG aerosols of known mass concentrations. The CERMS system comprises a unipolar diffusion charger (UDAC, Cambustion Ltd.) [116], centrifugal particle-mass analyzer (CPMA, Cambustion Ltd.), and Faraday cup aerosol electrometer (FCAE, TSI Inc., Model 3068B). The UDAC was operated at the ion concentration–time product of $4{\times}10^{13}$ ions s/m^3 and a sample flow of 2.14 slm. The charged particles were measured with a CPMA, which classifies particles based on the balance between centrifugal and electrostatic forces [117]. The CPMA was operated at a flow rate of 2.14 slm and a resolution $R_\mathrm{m} = 10$. Measurements were carried out at CPMA setpoints (M) in the range of 0.1–0.5 fg per elementary charge. The soot charging model from Ref. [118] is extrapolated to the FLG flakes used here in order to predict the average charge per flake and thereby enabling calculating the average flake mass of 0.18–8 fg. This extrapolation is approximate as it assumes that an FLG flake has the same mobility and charging diameters as a soot particle of equal mass, resulting in an uncertainty of approximately 30 %. A more accurate calculation was not performed as no relationship of FLG properties with mass was observed during the analysis. For each CPMA setpoint, flakes of different mass-to-charge ratios can pass through the instrument, as defined by the instrument transfer function. The FWHM of the CPMA transfer function was calculated as $0.4M$ following the finite-difference approach by Sipkens et al. [119] assuming single-charged spherical particles of constant density and a flow with a parabolic velocity profile. After the CPMA, the classified aerosol was split between the CAPS $\mathrm{PM_{SSA}}$ monitor and the FCAE. Both instruments were operated with an aerosol flow rate of 1.07 slm. The FCAE measures the aerosol charge concentration, which enables absolute mass-concentration measurements according to [117]

$$m_{\mathrm{total}} = m_0 + \frac{M \cdot I}{Q \cdot e}, \tag{4.7}$$

where m_0 is the mass concentration of the uncharged particles, M is the mass setpoint of the CPMA, I is the detected aerosol current, Q is the sample flow, and e is the elementary charge. The FCAE only detects charged particles, thus the presence of uncharged particles will bias the mass concentration measurements and consequently the calculated MAC values [120]. Therefore, the concentration of uncharged particles was probed downstream of the UDAC prior to the experiments using an electric precipitator (ESP, Cambustion Inc.) combined with a CPC, and was found to be < 100 particles/cm^3, which is < 1 % of the total particle concentration, and thus considered negligible.

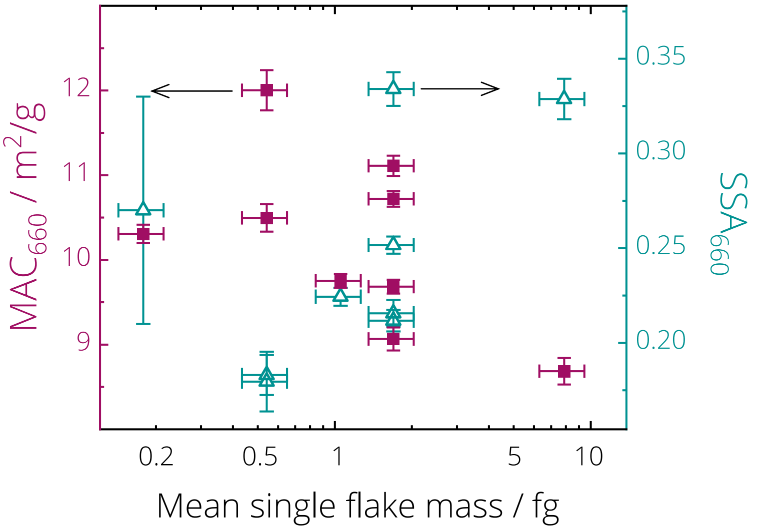

Figure 4.7 MAC and SSA for the crumpled FLG aerosol measured with the CAPS PM$_{SSA}$ at 660 nm versus mean single flake mass. Vertical error bars denote one standard deviation of the mean, horizontal error bars denote FWHM of the CPMA transfer function. The arithmetic mean MAC$_{FLG, 660}$ is 10.19 ± 1.10 m^2/g.

Figure 4.7 shows MAC and SSA for the crumpled FLG aerosol versus mean single flake mass in femtograms. The MAC was calculated at 660 nm as $MAC_{660} = b_{abs,660}/m^*$, where m^* is the particle-mass concentration measured with CPMA, and $b_{abs,660}$ is the aerosol absorption coefficient measured with CAPS PM$_{SSA}$ at 660 nm. The SSA was calculated as $SSA_{660} = b_{sca,660}/b_{ext,660}$. The calculated MAC arithmetic mean is MAC$_{FLG, 660}$ = 10.19 ± 1.10 m^2/g (± 11 %). The SSA$_{FLG, 660}$ values are scattered between 0.17–0.33. Both MAC$_{FLG, 660}$ and SSA$_{FLG, 660}$ demonstrate no apparent dependence on the flake mass. Recent studies on soot particles produced in flames and engines [118,121] reported mass-dependent MAC values and attributed the trend to differences in the degree of soot maturity or graphitization. For the FLG aerosol investigated here, the terms “maturity” and “graphitization” do not apply as graphene flakes were fully graphitized with a chemical structure consisting of > 98 % atomic carbon, as reported in Section 3.3. Therefore, it is not surprising that no size-dependence of MAC and SSA was observed for FLG flakes.

The UV-Vis data were additionally utilized to calculate the wavelength-resolved mass extinction coefficient of the FLG-ethanol suspension (MEC$_{FLG\text{-}ethanol,\lambda}$) using the Beer-Lambert law (Figure 4.8, blue curve). At λ = 660 nm, the MEC$_{FLG\text{-}ethanol, 660}$ = 5.75 m^2/g. This value is close to the MEC$_{660}$ = 5.8 m^2/g reported by Backes et al. [114] for an FLG-water suspension. However, this is almost half the aerosol MAC$_{FLG, 660}$ = 10.19 ± 1.10 m^2/g measured in this study. As the aerosol optical properties relate to particle morphology and chemical composition, there could be two reasons why the colloid MEC$_{FLG\text{-}ethanol, 660}$ is smaller than the aerosol MAC$_{FLG, 660}$, although neither of which can fully explain the twofold difference. First, a TEM comparison of aerosolized flakes with those sampled *in situ* reveals a small difference in flake aspect ratio (Figure 4.3). Second, the flakes in colloidal suspension and aerosol phases could have different chemical compositions. It is known that the presence of organic impurities in the aerosol enhances light absorption, and consequently, extinction [112,122]. Despite a significant effort being made to reduce amounts of ethanol and potential impurities in the aerosol, it is possible that some quantities of semi-volatile residues remained. A chemical composition analysis of aerosolized flakes is required to confirm or exclude that possibility and to conclude on the MEC$_{FLG\text{-}ethanol,}$ 660 vs MAC$_{FLG, 660}$ discrepancies.

The single-wavelength $\mathrm{MAC}_{\mathrm{FLG},660}$ value combined with knowledge on $\mathrm{AAE}_{\mathrm{FLG}}$ can be used to extrapolate $\mathrm{MAC}_{\mathrm{FLG}}$ to other wavelengths. Using the measured mean $\mathrm{MAC}_{\mathrm{FLG},660} = 10.19 \pm 1.10\ \mathrm{m}^2/\mathrm{g}$ and the $\mathrm{AAE}_{\mathrm{FLG}} = 0.55 \pm 0.02$:

$$\mathrm{MAC}_{\mathrm{FLG},\lambda} = \mathrm{MAC}_{\mathrm{FLG},660}\left(\frac{660}{\lambda}\right)^{\mathrm{AAE}_{\mathrm{FLG}}}. \tag{4.8}$$

Figure 4.8 compares the $\mathrm{MAC}_{\mathrm{FLG},\lambda}$ values reported here with available literature data on light-absorbing carbon aerosols. In terms of graphene, the most relevant work is by Zangmeister et al. [85], who measured the MAC_λ and AAE of two crumpled graphene aerosols with a broadband photoacoustic spectrometer: nanoplatelets (orange squares) and thermally reduced graphene oxide (rGO, blue squares). The authors generated the aerosols by nebulizing graphene–water suspensions. At 660 nm, they found the MAC_{660} of graphene and rGO to be 6.44 ± 0.09 and $6.85 \pm 0.13\ \mathrm{m}^2/\mathrm{g}$, respectively, while the corresponding AAE values were 0.74 ± 0.05 and 0.83 ± 0.07 [85]. The discrepancy between the MAC_λ and AAE reported by Zangmeister et al. and the results of the present study could be attributed to different measurement methods that employ different physical principles, and to different chemical compositions of graphene samples. The samples in the Zangmeister et al. study were dispersible in water, while chemically pure graphene is hydrophobic. The graphene sample used in this thesis could not be dispersed in water, which is why ethanol was used instead. No other optical properties data were available on graphene aerosols.

Figure 4.8 also shows the MAC_λ data for soot aerosols reported in the literature. Since most studies report MAC_λ at a single wavelength, such measurements were extrapolated across the visible spectrum using Equation (4.8) and either the reported AAE value or, when no wavelength-resolved data were available, an assumed $\mathrm{AAE} = 1$. Bond and Bergstrom [112] recommended $\mathrm{MAC}_{660} = 6.25 \pm 1\ \mathrm{m}^2/\mathrm{g}$ for soot based on 17 historical measurements. Another review by Zangmeister et al. assessed 199 MAC measurements for carbonaceous aerosols [85]. An

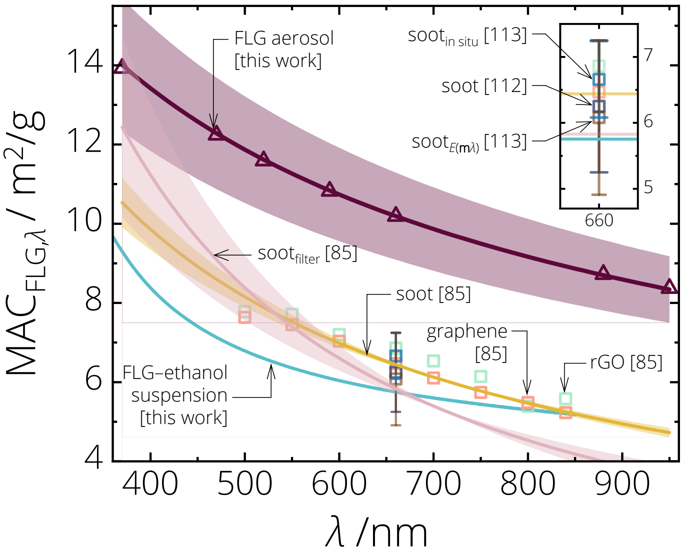

Figure 4.8 Wavelength-resolved MAC of a crumpled FLG aerosol (dark pink triangles) calculated from the $\mathrm{MAC}_{\mathrm{FLG},660} = 10.19 \pm 1.10\ \mathrm{m}^2/\mathrm{g}$ and the $\mathrm{AAE}_{\mathrm{FLG}} = 0.55 \pm 0.02$ (solid dark pink line). Shaded areas denote one standard deviation propagated from the MAC_λ and AAE uncertainties. Wavelength-resolved MEC of an FLG–ethanol suspension is shown as a solid aqua line. Other symbols and lines are the literature MAC data for carbonaceous aerosols. The inset shows the zoomed-in 660 nm part of the graph.

average of all measurements, removing the outliers with deviation from the mean $>5\sigma$, yielded $\mathrm{MAC}_{660} = 6.98 \pm 0.15$ m^2/g and AAE = 0.85 ± 0.09, while an average of only filter-based methods, again with $>5\sigma$ outliers removed, gave the $\mathrm{MAC}_{660} = 5.83 \pm 0.44$ m^2/g and AAE = 1.31 ± 0.28. A more recent review by Liu et al. [113] reported the $\mathrm{MAC}_{660} = 6.66 \pm 0.58$ m^2/g based on ten studies that measured both absorption and mass using *in situ* techniques. They also reviewed studies on mature soot $E(\mathbf{m}_\lambda)$ measurements and from that reported the average $\mathrm{MAC}_{660} = 6.08 \pm 1.17$ m^2/g. As one can see in Figure 4.8, the large body of literature on carbonaceous aerosols suggests MAC_{660} values between 5–7 m^2/g and the corresponding MAC_λ values that are smaller than those of crumpled FLG aerosols. That implies that crumpled FLG flakes absorb visible light more efficiently than mature soot particles. Hence, special care should be taken when producing and handling graphene aerosols, to prevent their release into the atmosphere in significant quantities, which could contribute to radiative forcing. The investigation of FLG and soot optical properties proceeds further using laser-induced incandescence in Chapter 5.

4.3 Optical properties modeling

Further insight into the connection between the morphology of crumpled FLG and its optical properties can be obtained through numerical simulations and comparison with the measurements. Here, two analyses were applied to FLG flakes with various morphologies: Rayleigh–Debye–Gans (RDG) theory and the discrete dipole approximation (DDA) [123,124]. The RDG and DDA simulations were done by Dr. Talebi-Moghaddam from the University of Waterloo.

4.3.1 Theory and methodology

In DDA, the matter is approximated as an ensemble of coupled “numerical” dipoles (each of which represents thousands of physical dipoles) that interact with each other in the presence of an oscillating electromagnetic field. The spectral cross-sections and the scattering phase function are then calculated by combining dipole fields and the field of the irradiation far away from the object. The result is a rigorous albeit computationally intensive simulation of how an incident electromagnetic (EM) wave interacts with matter.

RDG theory, in contrast, provides a more straightforward, analytically closed-form expression for the absorption and scattering cross-sections. The foundation of this approach is the electrostatic approximation, in which the phase variation of the electromagnetic field inside the particle is assumed to be negligible. Accordingly, each dipole interacts “in phase” with the EM wave, and thus their contribution to the overall absorption and scattering cross-sections can simply be superimposed. In particular, the spectral cross-sections approximated in RDG theory are [125]:

$$C_{\mathrm{abs},\lambda} = \frac{\pi^2 d_{\mathrm{V}}^3 n_{\mathrm{med}}}{\lambda} E\left(\mathbf{m}_\lambda\right), \tag{4.9}$$

and

$$C_{\mathrm{sca},\lambda} = \frac{2\pi^5 d_{\mathrm{V}}^6 n_{\mathrm{med}}^4}{3\lambda^4} F\left(\mathbf{m}_\lambda\right), \tag{4.10}$$

where d_V is the volume equivalent diameter of a crumpled FLG flake, n_{med} is the index of refraction of a dielectric medium, $E(\mathbf{m}_\lambda)$ is given by Equation (4.6), and

$$F\left(\mathbf{m}_\lambda\right)=\left|\frac{\mathbf{m}_\lambda-1}{\mathbf{m}_\lambda+2}\right|^2. \tag{4.11}$$

The spectral extinction efficiency is then

$$Q_{\text{ext},\lambda}=Q_{\text{sca},\lambda}+Q_{\text{abs},\lambda}=\frac{4\left(C_{\text{sca},\lambda}+C_{\text{abs},\lambda}\right)}{\pi d_{\text{V}}^2}. \tag{4.12}$$

The optoelectronic properties of graphene are highly anisotropic due to the two-dimensional confinement of electrons through π-bonds and the specific band structure of graphene [127]. This is reflected by distinct in-plane and off-plane refractive indices of graphene [126,128–131]. It is also possible that the optical properties of crumpled FLG flakes differ from a single- or few-layer plane graphene on a substrate due to their complex "non-flat" morphology. In the absence of data on crumpled graphene materials, the analysis was extended towards graphite refractive indices [132,133]. The refractive indices of graphene and graphite used in this study are shown

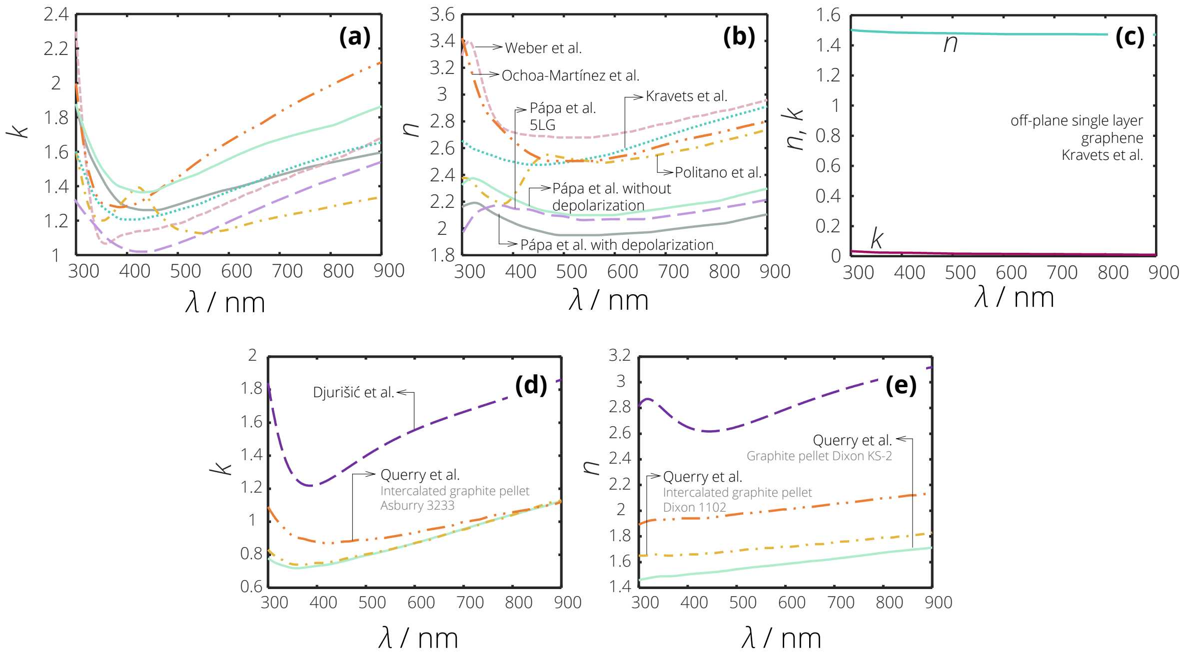

Figure 4.9 Refractive indices used in DDA and RDG simulations. (a), (b): in-plane refractive indices of graphene; (c): off-plane refractive index of graphene measured in Ref. [126]; (d), (e): in-plane refractive indices of graphite.

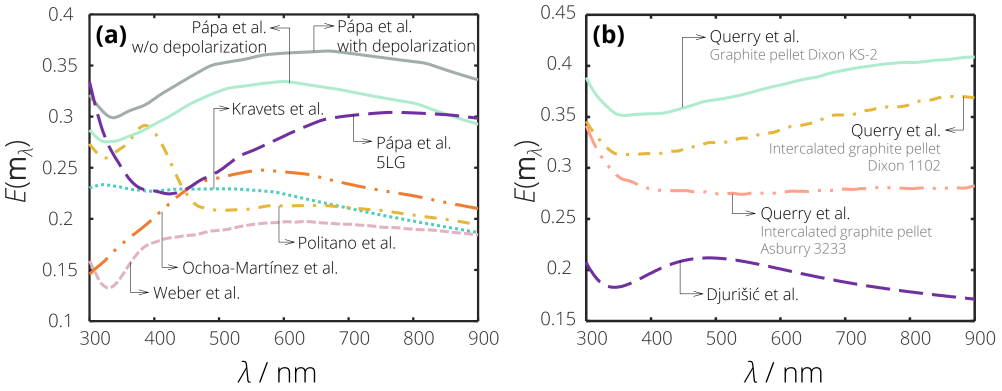

Figure 4.10 Graphene (a) and graphite (b) absorption functions as calculated from the refractive indices from the literature. The medium in all cases was air ($n_{med} = 1$). The summary of the studies is given in Table 4.1.

in Figure 4.9, and the corresponding $E(\mathbf{m}_\lambda)$ values are shown in Figure 4.10. The datasets summaries are given in Table 4.1.

DDA was applied to three FLG flakes shown in Figure 4.11. First, the flakes were volumetrically reconstructed from the tomographic TEM images using the open source Tomviz software [134], which utilizes the weighted back-projection algorithm. Next, the 3D-reconstructed flakes were meshed. The original volumetric shapes contained artifacts caused by the tomographic reconstruction algorithm. Therefore, the 3D objects were initially meshed with a uniform DDA mesh with a lattice size parameter of 0.35 nm, which is the approximate thickness of monolayer graphene. A cut-off radius of 30 nm was defined for each dipole, and all the dipoles inside

Table 4.1 Refractive indices of graphene and graphite used in the DDA calculations.

Author	Material	Methodology
Kravets et al. [126]	Single-layer graphene	Ellipsometry applied to a single-layer graphene placed on an amorphous quartz substrate
Weber et al. [128]	Single-layer graphene	Ellipsometry applied to a mechanically exfoliated graphene flake on a silicon wafer with SiO_2 on top
Politano et al. [129]	Bilayer graphene	Ellipsometry applied to a CVD-grown bilayer graphene produced by multiple transfers on SiO_2/Si and polyethylene terephthalate substrates
Ochoa-Martínez et al. [130]	Single-layer graphene	Ellipsometry applied to graphene films grown on copper substrates and transferred onto a SiO_2/Si substrate
Pápa et al. [131]	Single- and five-layer graphene	Ellipsometry applied to single- and five-layer graphene on a SiO_2 substrate. The influence of depolarization was investigated
Djurišić et al. [132]	Highly-oriented pyrolytic graphite	The optical properties of graphite modeled with a modified Lorentz–Drude model. Good agreement with ellipsometry measurements for highly-oriented pyrolytic graphite observed
Querry [133]	Various graphite pellets	Reflectance spectra of various disk-shaped graphite pellets acquired. The refractive index was inferred using the Kramers–Kronig method. Three refractive indices were used: (1) graphite pellet, Dixon KS-2; (2) intercalated graphite pellet, Dixon 1102; (3) intercalated graphite pellet, Asbury 3222

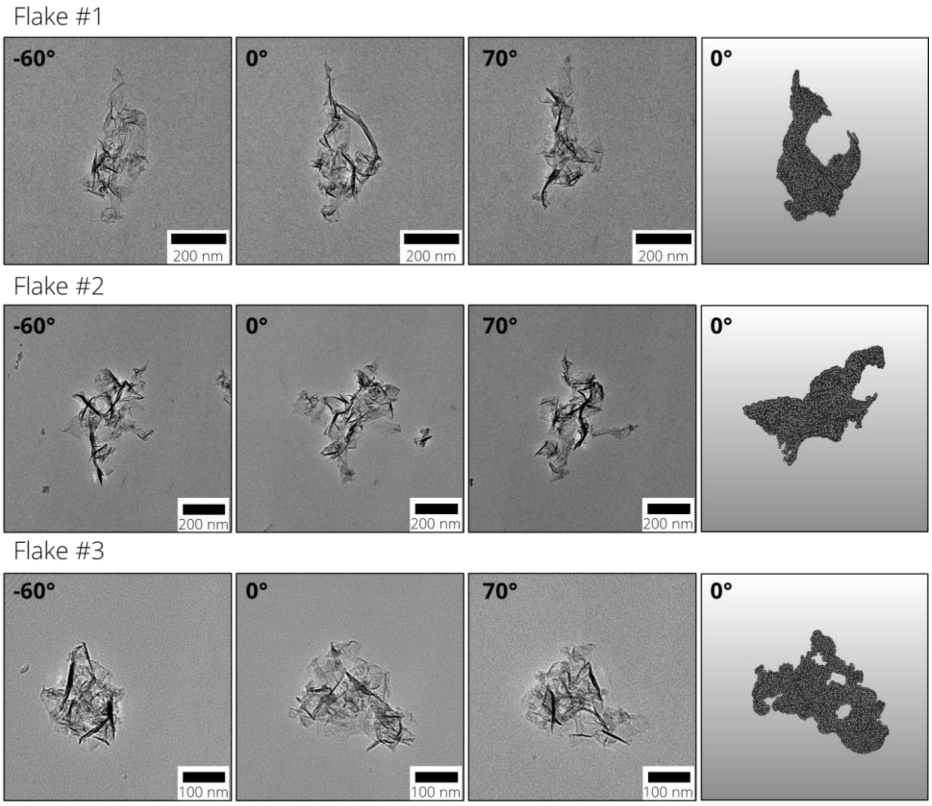

Figure 4.11 TEM micrographs of the aerosolized crumpled FLG flakes at three viewing angles and the volume-reconstructed flakes at 0°. Volume-reconstructed flakes were meshed and used in the DDA analysis.

this radius were counted. If the number of dipoles contained within this radius was less than 3200, the dipole is removed. This process was repeated for all the dipoles. The parameters for this algorithm were adjusted to make the final 3D mesh visually similar to the tomographic results and achieve a single dipole thickness in parts of a flake where single-layer graphene was detected.

To account for graphene optical anisotropy, three methods for assigning the polarizability tensor of each dipole were compared: (i) assuming random orientation for each dipole; (ii) assuming fixed orientation for all dipoles; and (iii) the plane fit approach described in the Appendix C. All three approaches produced identical normalized $Q_{\mathrm{abs},\lambda}$ spectra (Figure C.1), hence, the plane-fit approach was used for all subsequent DDA simulations and no model error is expected for the normalized $Q_{\mathrm{abs},\lambda}$ and $Q_{\mathrm{ext},\lambda}$.

The light scattering model under the RDG approximation was first developed for anisotropic spheres by Pecharroman et al. [135], but it does not strictly apply to the complex morphology of crumpled FLG flakes. However, negligible absorption and scattering contributions are expected from the off-plane refractive index (Figure 4.10 c), normalized FLG cross-sections could be approximated with RDG using particle volume equivalent diameters, d_V, and the in-plane refractive index of the scatterer only. The final FLG flakes #1, #2, and #3 (Figure 4.11) have d_V of 16.2, 13.8, and 17.6 nm, respectively.

4.3.2 Results

Figure 4.12 compares the extinction spectra derived using the RDG approximation against DDA simulations for the geometries of three investigated FLG flakes. The refractive index data of single-layer graphene from Kravets

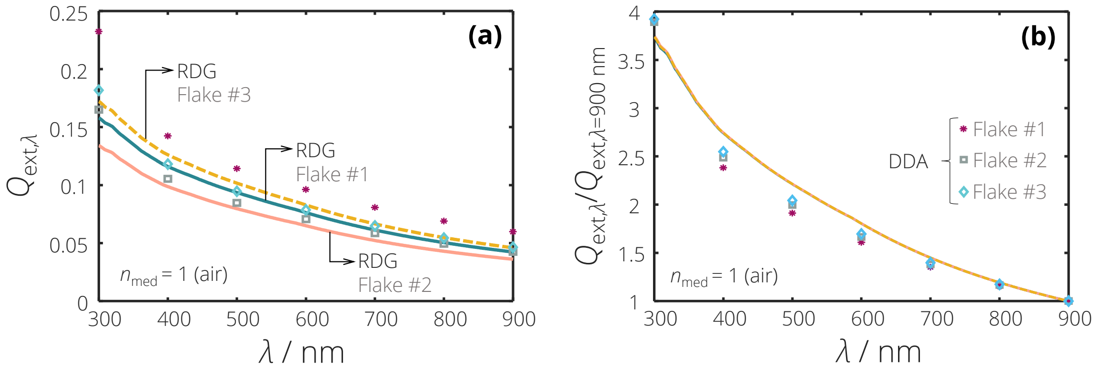

Figure 4.12 Verifying the RDG predictions of absolute (a) and normalized (b) extinction efficiencies for FLG flakes #1, #2, and #3 with DDA. The relative difference between RDG and DDA decreases from 33 % at λ = 300 nm to 9 % at λ = 900 nm. The normalized plot (b) shows that RDG is capable of predicting the averaged spectral cross-section of crumpled FLG flakes. Calculations were performed for n_{med} = 1.0 (air). The refractive index of graphene from Kravets et al. [126] was used.

et al. [126] and the refractive index of air as the surrounding medium (n_{med} = 1) were used. The RDG approximation by its nature is unable to account for the influence of particle orientation on the optical properties, so RDG predictions are compared with orientation-averaged DDA results. The relative difference between RDG and DDA decreases from 33 % at λ = 300 nm to 9 % at λ = 900 nm, which is caused by a decrease in the phase shift parameter $\rho = \pi d_V |\mathbf{m}_\lambda| / \lambda$. The normalized plot in Figure 4.12 b also shows that the RDG can predict the slope of the spectral cross-section. Therefore, RDG can be used as an approximation to evaluate averaged spectral cross-sections of crumpled FLG flakes, especially at near-infrared wavelengths, e.g., 1064 nm, which is often used in laser-induced incandescence [66].

The DDA simulations were repeated for Flake #1 using a refractive index independent of wavelength to assess whether the crumpled FLG absorbs and emits in the Rayleigh regime. Three complex refractive indices were chosen from Kravets et al. [126]: $\mathbf{m}_{300\mathrm{nm}}$ = 2.656 + 1.879i, $\mathbf{m}_{600\mathrm{nm}}$ = 2.566 + 1.382i, and $\mathbf{m}_{900\mathrm{nm}}$ = 2.912 + 1.596 i. If the RDG

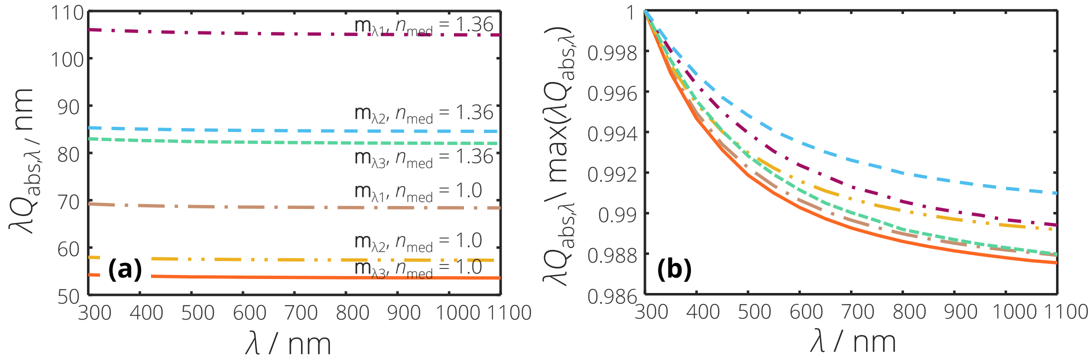

Figure 4.13 Absolute (a) and normalized (b) λ $Q_{\mathrm{abs},\lambda}$ values calculated using DDA with fixed refractive indices at λ_1 = 300 nm, λ_2 = 600 nm, and λ_3 = 900 nm from [126]. Refractive index of a medium: n_{med} = 1.36 (ethanol), n_{med} = 1.0 (air). $\lambda Q_{\mathrm{abs},\lambda}$ drops by only 1.2 % from 300 nm to 1100 nm, indicating that the RDG model could be a valid approximation to predict the slope of $Q_{\mathrm{abs},\lambda}$ for crumpled FLG particles.

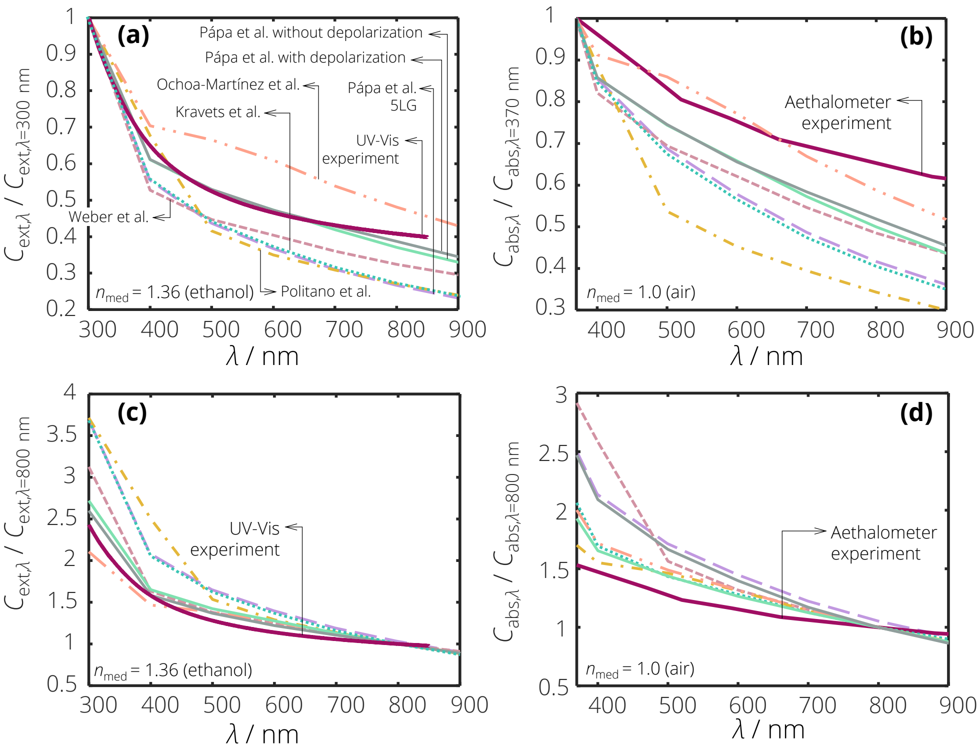

Figure 4.14 Comparing DDA simulations for different graphene refractive indices with: (a), (c): UV-Vis extinction measurements of the colloid; (b), (d): aethalometer measurements of the aerosol. The curves in (a), (b) are normalized to 300 nm, in (c), (d) to 800 nm. The refractive indices of the media are taken to be 1.36 (ethanol) and 1.0 (air). The refractive index from Pápa et al. [131] provides the closest fit to the UV-Vis data, while no literature refractive index can describe the aethalometer data.

model is valid, it is expected from Equations (4.9) and (4.12) that $\lambda Q_{\text{abs},\lambda}$ be wavelength independent. Figure 4.13 shows that $\lambda Q_{\text{abs},\lambda}$ drops by only 1.2 % from 300 to 1100 nm, indicating that the RDG model is indeed a valid approximation to predict the slope of $Q_{\text{abs},\lambda}$ for graphene in the visible and near-infrared.

Figure 4.14 compares the normalized values of experimentally measured extinction efficiencies of the FLG–ethanol suspension (UV-Vis) and the FLG aerosol (aethalometer) against DDA simulations using different graphene in-plane refractive indices. The off-plane refractive index from Kravets et al. [126] was adopted. There is a considerable variation in the results based on the chosen refractive index. The closest fit to the UV-Vis data was achieved using the single-layer graphene data from Pápa et al. [131] with no influence of depolarization observed. The DDA curve for five-layer graphene [131], though having a similar layer number as the FLG flakes in this study, did not improve the fit to the experimental data. Moreover, none of the DDA simulations resemble the aethalometer measurements carried out on FLG aerosols. This could indicate that the morphology of colloidal FLG flakes is closer to that of plane graphene sheets, while aerosolized FLG flakes have complex crumpled nature, which alters the graphene electronic structure [136,137], and thus, the optical properties. To determine the morphology of the flakes in suspensions, *in situ* measurements are necessary, such as multi-angle elastic light scattering [138,139].

The comparison of UV-Vis and aethalometer measurements with DDA predictions using graphite refractive indices is shown in Figure 4.15. The DDA simulations predict the experimental UV-Vis curve and reasonably

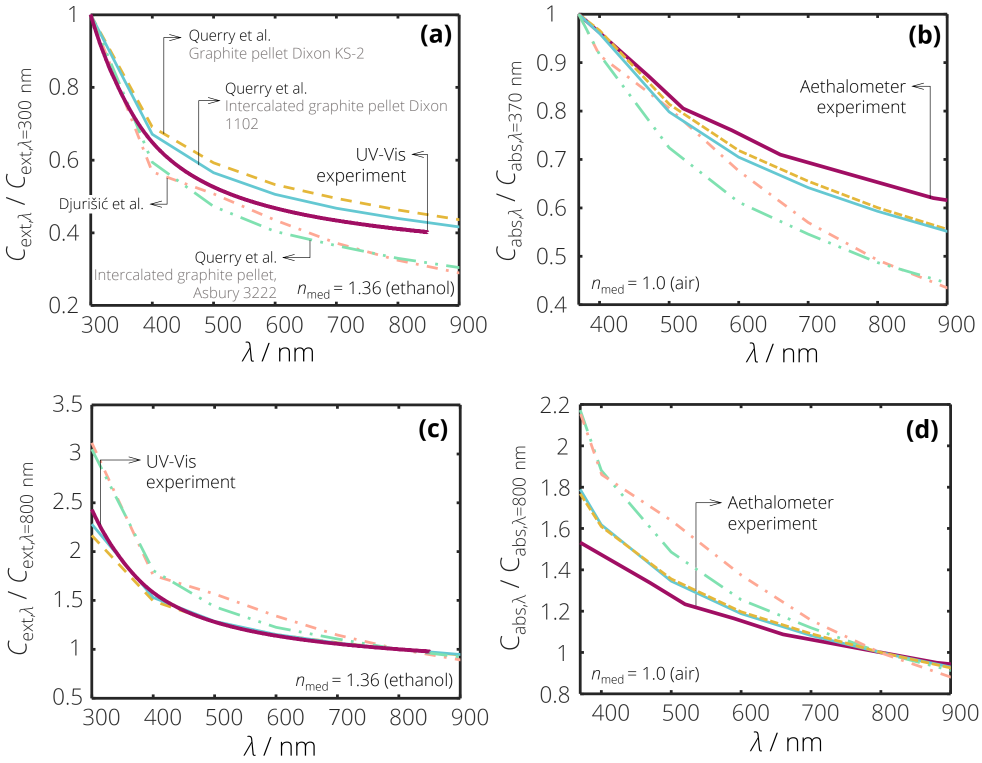

Figure 4.15 Comparing DDA results for different graphite refractive indices with: (a), (c): UV-Vis extinction measurements of the colloid; (b), (d): aethalometer measurements of the aerosol. The curves in (a), (b) are normalized to 300 nm, in (c), (d) to 800 nm. The refractive indices of the media are taken to be 1.36 (ethanol) and 1.0 (air). The graphite refractive indices for graphite pellets (Dixon KS-2) and intercalated graphite pellets (Dixon 1102) from Querry [133] provide the closest fit for experiments in both media.

well describe the experimental aethalometer curve. Overall, the difference between the graphite DDA predictions and the measurements is smaller compared to that of graphene DDA shown in Figure 4.14. The best-fitting simulations for FLG in both media provide the graphite refractive indices of Dixon KS-2 pellets and Dixon 1102 intercalated graphite pellets from Querry [133].

Overall, these results suggest that the absorption characteristics of crumpled FLG materials are more aligned with the optical properties of graphite rather than those of graphene. Note that TEM, Raman spectroscopy, and BET analysis verified that the sample in this study was indeed crumpled turbostratic few-layer graphene and not graphite [66]. Moreover, when using the refractive indices of the plane five-layer graphene sheet [131], the DDA fit to the experimental data did not improve compared to single- and double-layer graphene simulations, even though having a similar layer number to the FLG flakes investigated in this thesis. It is also known that the electronic structure of graphene depends on the sheet morphology [136,140]. In particular, graphene surface wrinkling was reported to introduce a finite optical band-gap [136] and enhance the optical anisotropy, as the charge-carrier transport along and across the folded parts is governed by distinct effects [141]. Hence, the speculation is that the crumpled and turbostratic nature of graphene flakes plays a more important role than the layer number in regard to optical properties. It is difficult to quantify a specific threshold level of crumpledness at which optical properties transition from those of graphene to those of graphite. Experiments aimed at measuring the FLG specific surface area, which correlates with crumpledness, may help to answer this question. This is addressed in Chapter 5 using laser-induced incandescence.

Given the close connection between optical properties and charge transport, this observation also raises the question as to whether the electrical properties of the crumpled FLG are closer to those of graphite or defect-free single-layer graphene. While no direct comparison is provided here, the crumpled FLG synthesized previously at the IVG with the same method as the one used in this study demonstrated excellent performance when used in Li-ion batteries because of its high electrical conductivity and surface area [34]. Moreover, the successful application of crumpled graphene in batteries, capacitors, and electrocatalysts [142–144] again demonstrates its unique electrical and morphological characteristics that are different from bulk graphite and flat single-layer graphene. It also has been shown, that the electrical properties of graphene converge to those of graphite only at 11+ layers at room temperature [11,140], however, these studies did not investigate crumpled turbostratic graphene.

To validate the experimentally-observed plasmonic response of graphene at UV wavelengths, further DDA simulations with a small wavelength increment (5 nm) were conducted for Flakes #1 and #2 (Figure 4.11) using different refractive indices. For these calculations, it was necessary to extrapolate the off-plane refractive index at $\lambda < 300$ nm by equating it to the value at $\lambda = 300$ nm, however, the off-plane part of the refractive index was shown to have a negligible effect on the results. Figure 4.16 a shows that the DDA simulations predicted a localized surface plasmonic resonance (LSPR) peak, although it was narrower and blue-shifted compared with the experimental one. These discrepancies could be caused by wide distributions of FLG flakes size, shape, and random orientation in the suspension, as well as by an inaccurate refractive index of graphene/graphite used in the DDA simulation. The complexity of the problem again highlights the necessity for further research on the optical properties of crumpled FLG flakes. Figure 4.16 b shows that the RDG approximation, as expected, cannot reproduce the LSPR peak, highlighting the fact that the electrostatic approximation is not valid for the UV region.

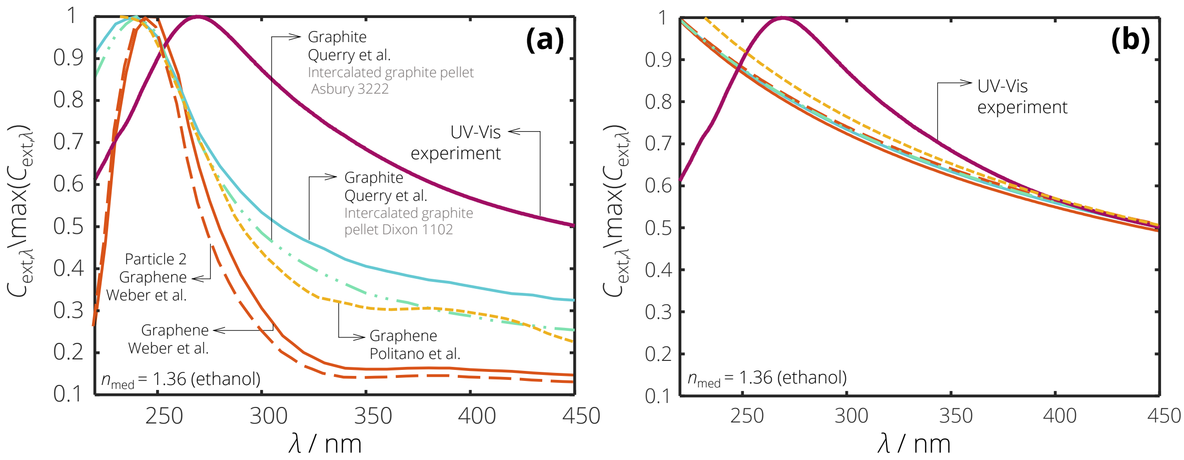

Figure 4.16 Comparing the experimentally determined UV-Vis extinction spectrum with spectra found using DDA (a) and RDG (b) simulations. The DDA predicted extinction peak is narrower and blue-shifted compared to the experimental one. The RDG approximation cannot reproduce the extinction peak.

4.4 Conclusions and future work

Crumpled FLG aerosol is one of the most prevalent mass-produced graphene materials, for which the electronic and optical properties, as well as toxicity, depend on flake morphology, which creates a need for reliable characterization.

In this chapter, a suite of complementary aerosol measurement techniques was deployed to analyze flake lateral size and aspect ratio, mobility, and aerodynamic diameters. Measured aerodynamic size distribution enabled the calculation of respiratory deposition of crumpled FLG aerosol following the established deposition model [94,95]. The results indicated that, when inhaled, crumpled FLG flakes are likely to reach and accumulate in the deep lung region, hence, potentially leading to adverse health effects.

The optical properties were assessed in terms of spectrally-resolved extinction and absorption coefficients, aerosol Ångström exponent, single-scattering albedo, and mass absorption cross-sections. The measurements suggested stronger visible light absorption for crumpled FLG aerosols compared to soot aerosols. Moreover, the spectroscopic data were correlated with the mean graphene layer number and mean lateral size using the established metrics by Backes et al [114].

DDA simulations were carried out on the tomography-reconstructed flakes to investigate the connection between the optical properties and the flake orientation and morphology. The flake orientation had no impact on the normalized absorption efficiency of the particles, and Rayleigh–Debye–Gans theory was proven to be a reasonable approximation when calculating the spectral cross-sections of crumpled FLG. Furthermore, simulated extinction and absorption cross-sections more closely resembled the experimentally measured ones when using the refractive indices of graphite, rather than refractive indices of single- or few-layer flat graphene.

A promising direction of future research lies in the morphological and optical characterization of suspensions of crumpled FLG and freshly-generated aerosols directly from the gas-phase reactor. Such studies would provide information on graphene formation and growth kinetics and elucidate how its morphology and chemical composition changes by aerosolization and interactions with solvents. This is partially approached in the next chapter using laser-induced incandescence diagnostics.

Chapter 5
TiRe-LII diagnostics

Laboratory-scale gas-phase plasma synthesis of crumpled FLG aerosols, employed throughout this thesis, produces highly-structured materials having purity equal to or exceeding other synthesis routes [12]. However, more must be known about the formation mechanism, the synthesis process, and graphene properties in order to improve yields and develop industrial-scale processes. Accordingly, there is a need for *in situ* optical diagnostics to obtain insight into graphene growth kinetics and morphology dynamics, to learn how to control synthesis and increase yield, as well as to monitor the graphene flakes *in situ* during the production.

Time-resolved laser-induced incandescence (TiRe-LII) is a promising tool to fulfill at least some of these needs. In TiRe-LII, the nanoparticles within an aerosol sample volume are heated by a laser pulse, and the resulting incandescence is measured as a function of time, typically at multiple wavelengths, as the particles return to the ambient gas temperature. In LII diagnostics, the nanoparticle volume fraction is inferred from the signal intensity, while the particle size distribution parameters (and other properties) are found by fitting a modeled particle temperature decay curve to a pyrometrically-inferred one. TiRe-LII is widely used in combustion-related applications to measure soot particle size and volume fraction [145,146], and it also has been successfully applied to many other types of nanoparticle aerosols, including metals [147–151], semiconductors [152,153], oxides [154,155], carbon nanotubes [156–159], and core-shell particles [160,161]. This thesis demonstrates the first use of TiRe-LII to probe FLG flakes.

This chapter presents three sets of TiRe-LII measurements on FLG aerosols. First, the general applicability of the method to FLG aerosols is investigated through experiments in a test cell. The TiRe-LII response of crumpled FLG flakes is compared to that of soot aerosols, and the differences are discussed in the context of aerosol properties. Second, the LII is used to measure flake concentrations (volume fraction) in a controlled experiment. Finally, the TiRe-LII is applied *in situ* in the microwave plasma reactor to probe the evolution of crumpled FLG morphology.

5.1 TiRe-LII theory

In TiRe-LII, nanoparticles in a probe volume are heated by a laser pulse and then return to the ambient gas temperature via various heat transfer mechanisms, shown schematically for an FLG flake in Figure 5.1. The probe volume is the intersection between the beam of the excitation laser and the solid angle of the detection optics. During the cooling process, the energy balance of an individual nanoparticle or flake is governed by

$$\frac{\mathrm{d}U_{\mathrm{int}}}{\mathrm{d}t} = \rho c_p \frac{\pi d_{\mathrm{p,eff}}^3}{6} \frac{\mathrm{d}T_{\mathrm{p}}}{\mathrm{d}t} = q_{\mathrm{abs}} + q_{\mathrm{rad}} + q_{\mathrm{cond}} + q_{\mathrm{evap}}\,, \tag{5.1}$$

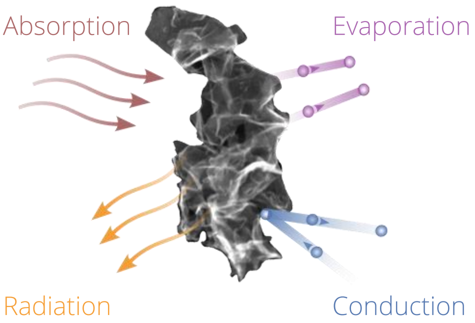

Figure 5.1 Schematic representation of the heat transfer mechanisms experienced by a laser-heated FLG flake. At atmospheric pressure, radiation is negligible compared to conduction and evaporation.

where U_{int} is the internal energy of the particle, t denotes time, ρ and c_p are the nanoparticle material density and specific heat capacity, $d_{\mathrm{p,eff}}$ is the nanoparticle effective diameter (e.g., d_{V}), T_{p} is the particle temperature, q_{abs} is the rate at which the laser energy is absorbed by the nanoparticle, and q_{rad}, q_{cond}, and q_{evap} are the cooling rates due to radiation, conduction, and evaporation, respectively. When time-resolved data are available, Equation (5.1) can be solved for d_{p}, or in the case of non-spherical particle, $d_{\mathrm{p,eff}}$.

In practice, a TiRe-LII experiment starts with heating an aerosol using a pulsed laser and detecting time-resolved LII signals at a single or at multiple wavelengths, then inferring the nanoparticle temperature trace, and finally simulating the nanoparticle cooling to derive the quantities of interest, e.g., the specific surface area. This section describes the theoretical part of the analysis, while the experimental part is given in the following section.

In the case of a monodisperse aerosol, the detected spectral incandescence intensity is given by:

$$J_\lambda(\lambda,T_{\mathrm{p}}) = f_V G_\lambda C_{\lambda,\mathrm{abs}} \frac{2hc_0^2}{\lambda^5}\left[\exp\left(\frac{hc_0}{k_{\mathrm{B}}\lambda T_{\mathrm{p}}}-1\right)\right]^{-1}, \tag{5.2}$$

where f_V is the volume fraction of the flakes, G_λ is a setup-specific parameter accounting for detector geometry and efficiency, k_{B} is the Boltzmann constant, h is the Planck constant, c_0 is the speed of light in vacuum, and $C_{\lambda,\mathrm{abs}}$ is the spectral absorption cross-section of FLG. The numerical simulations presented in Chapter 4 showed that the Rayleigh approximation to Mie theory adequately describes the crumpled FLG spectral cross-sections. Hence, $C_{\lambda,\mathrm{abs}}$ is calculated from Equation (4.9), where $n_{\mathrm{med}} = 1$ for argon and air used in the experiments presented in the next section. Notably, the consequence of the Rayleigh approximation is that both the absorption cross-section in Equation (4.9) and the sensible energy on the left-hand side of Equation (5.1) are proportional to volume, so materials having similar $E(\mathbf{m}_\lambda)$ but different volumes should nevertheless reach approximately the same peak temperature.

The parameter accounting for detector geometry and efficiency, G_λ, depends on multiple factors, e.g., the f-number and the spectral transmission of the collection optics, the detector gain, the laser sheet thickness, the transmissivity of bandpass filters and neutral density filters, the detector spectral efficiency, etc. For simplicity, all these factors are combined in a single parameter for each bandpass-filtered detection channel. The G_λ values for the two detection setups used in this thesis (described in Section 5.2) were found through measurements with a light source of a known spectral output. The detection setup calibration procedure is beyond the scope of this thesis and is described in detail elsewhere [162].

To calculate the $C_{\lambda,\mathrm{abs}}$, as defined in the Equation (4.9), the wavelength dependence of $E(\mathbf{m}_\lambda)$ should be known. Although the optical measurements on aerosolized graphene presented in Chapter 4 showed the wavelength dependence of $E(\mathbf{m}_\lambda)$, it is not clear yet if these results can be extrapolated to *in situ* measurements of flakes formed in the gas-phase. The aerosolization process changed the flake aspect ratio and could introduce chemical impurities, hence, altering the aerosol optical properties. Therefore, for the initial TiRe-LII study on as-synthesized FLG aerosols, the $E(\mathbf{m}_\lambda)$ is assumed to be wavelength independent over the detection range of interest, as is frequently done for mature soot [146,163]. Then, all wavelength-independent properties in Equation (5.2) are combined into a scaling factor C, yielding the spectral incandescence

$$J_\lambda(\lambda,T_\mathrm{p})=C\frac{2hc_0^2}{\lambda^6}\left[\exp\left(\frac{hc_0}{k_\mathrm{B}\lambda T_\mathrm{p}}-1\right)\right]^{-1}. \tag{5.3}$$

When detecting the experimental incandescence signals, J_λ^exp, at different wavelengths, the particle temperature (maximum likelihood estimate) is inferred using weighted least-squares minimization

$$\left(T_\mathrm{p},C\right)=\underset{T_\mathrm{p},\mathrm{C}}{\mathrm{argmin}}\left\{\sum_i\left(\frac{J_{\lambda,\mathrm{i}}^\mathrm{exp}-J_{\lambda,\mathrm{i}}^\mathrm{mod}(T_\mathrm{p},C)}{\sigma_\mathrm{i}}\right)^2\right\}, \tag{5.4}$$

where C is the scaling factor, and σ_i is the standard deviation of the mean of $J_{\lambda,i}^\mathrm{exp}$ for the i^th channel. The $J_{\lambda,i}^\mathrm{mod}$ is the modeled incandescence calculated following the Equation (5.3).

The next part of the analysis involves modeling the heat transfer mechanisms to reproduce flake heating and cooling, and then use this model to infer the quantities-of-interest. The main heat transfer mechanisms were schematically shown in Figure 5.1.

The laser absorption is responsible for nanoparticle heat-up to high temperatures, leading to incandescence. In its basic form, the laser absorption term is given as

$$q_\mathrm{abs}=C_{\mathrm{abs},\lambda_\mathrm{l}}F_0, \tag{5.5}$$

where λ_l is the laser wavelength and F_0 is the laser fluence. In the case of particles in the Rayleigh regime, the laser absorption term is

$$q_\mathrm{abs}=\frac{\pi d_\mathrm{p,eff}^3}{\lambda_\mathrm{l}}E\left(\mathbf{m}_{\lambda_\mathrm{l}}\right)F_0. \tag{5.6}$$

Here, the absorption function $E(\mathbf{m}_\lambda)$ shows which fraction of the laser energy is absorbed by the flake and transferred into its internal energy.

Although radiative emission, q_{rad}, represents the detected incandescence signal and underlies the principle of the measurement, it is generally negligible compared to conduction and evaporation except at very low pressures [145].

Heat conduction represents the energy transfer by collisions of gas molecules with the flake surface. The nature of conductive cooling depends on the conduction regime as defined by the Knudsen number, $Kn = \lambda_g/L$, where λ_g is the mean free path in the gas, and L is the flake characteristic length. When $Kn > 1$, the conduction heat transfer occurs in the free-molecular regime, within which gas molecules travel ballistically between the equilibrium gas and the nanoparticle surface. Accordingly, the conduction heat rate can be written as

$$q_{\mathrm{cond}} = -\alpha A_{\mathrm{cond}} N''_{\mathrm{g}} k_{\mathrm{B}} \left(2 + \frac{\zeta_{\mathrm{rot}}}{2}\right)\left(T_{\mathrm{p}} - T_{\mathrm{g}}\right), \tag{5.7}$$

where

$$N''_{\mathrm{g}} = \frac{n_{\mathrm{g}} c_{\mathrm{g}}}{4} = \frac{p_{\mathrm{g}} c_{\mathrm{g}}}{4 k_{\mathrm{B}} T_{\mathrm{g}}} \tag{5.8}$$

is the incident number flux of gas molecules per elementary area, k_{B} is the Boltzmann constant, α is the thermal accommodation coefficient, which represents the collision energy transfer efficiency, A_{cond} is the surface area available for conductive heat transfer, ζ_{rot} is the number of rotational degrees of freedom of the gas molecules (zero for monoatomic Ar used here), T_{g} and p_{g} are the gas temperature and pressure, n_{g} is the molecular number density, m_{p} is the flake mass, c_p is the flake heat capacity at constant pressure, and $c_{\mathrm{g}} = [8k_{\mathrm{B}} T_{\mathrm{g}}/(\pi m_{\mathrm{g}})]^{1/2}$ is the mean thermal speed of the gas molecules.

The evaporation term, q_{evap}, becomes significant when a nanoparticle or a flake reaches high temperatures, i.e., at high laser pulse fluences. The transition temperature (energy) value depends on the heat transfer model applied and the particle absorption efficiency at the excitation wavelength, generally, for mature soot irradiated with 1064 nm radiation the evaporation term becomes dominant at temperatures 3200–3800 K and laser fluences 1.5-2 mJ/mm^2 [145,164,165]. The LII evaporation sub-model depends on the particle temperature, its surface area, and the latent heat of vaporization (i.e., the energy required to sublime one carbon atom from the nanoparticle) [145]

$$q_{\mathrm{evap}} = \frac{\Delta H_{\mathrm{V}}}{M_{\mathrm{V}}} \frac{\mathrm{d}m_{\mathrm{p}}}{\mathrm{d}t}, \tag{5.9}$$

where ΔH_{V} is the molar heat of vaporization, M_{V} is the vapor molar mass, and $\mathrm{d}m_{\mathrm{p}}/\mathrm{d}t$ is the rate of the particle mass loss that occurs in the free-molecular regime [145,166,167]

$$\frac{\mathrm{d}m_{\mathrm{p}}}{\mathrm{d}t} = -m_{\mathrm{V}} \pi d^2_{\mathrm{p,eff}} \frac{p_{\mathrm{V}} c_{\mathrm{V}}}{4 k_{\mathrm{B}} T_{\mathrm{p}}}, \tag{5.10}$$

where m_V is the vapor species mass, p_V is the vapor pressure given by the Clausius-Clapeyron equation, and c_V is the mean thermal speed of the vapor.

Some LII models consider additional phenomena, including oxidation, thermionic emission, and annealing [145,168,169]. These cooling mechanisms are only applicable to specific materials or experimental conditions and neglected in other cases. In the context of this thesis, investigated graphene flakes were shown to be almost fully graphitized (XPS analysis, Section 2.3.3), had no oxygen incorporation, and contained no oxide surface layer (TEM, XPS, Raman, UV-Vis, Sections 3.3 and 4.2.2), hence, no annealing and oxidation terms were considered. Thermionic emission, i.e., loss of energy by emitting electrons, was shown to be negligible for carbonaceous materials experiencing laser fluences below 10 mJ/mm^2 [145,170]. Therefore, the heat transfer model applied throughout this work is limited to absorption, conduction, and evaporation.

5.2 Experimental setup and results

Three sets of TiRe-LII experiments were carried out throughout this thesis. First, the general applicability of the method to crumpled FLG aerosols was studied and the TiRe-LII response of flakes was qualitatively compared to that of mature soot. Second, the synthesized FLG powder was aerosolized to measure flake mass concentrations (volume fraction) with a commercial LII setup (LII 300, Artium Inc.). Finally, TiRe-LII was applied in the gas-phase reactor to probe crumpled FLG morphology *in situ,* measuring the specific surface area (SSA). Hence, three measurement setups are consecutively described in this section.

5.2.1 Aerosol experiments in a flow-through test cell

The first set of TiRe-LII measurements was conducted on an aerosol pneumatically extracted downstream of the plasma reactor and continuously transported via a 12.7-mm diameter, 15-m long pipe through the LII test cell (Artium Inc.). The excitation setup is shown in Figure 5.2. The cell pressure was maintained at 400 mbar and monitored with a pressure transducer (VD8, Thyracont GmbH). FLG flakes were heated using a pulsed 1064 nm Nd:YAG laser (Powerlite 7000, Continuum) operating at 10 Hz with a pulse duration of 10 ns full-width half-maximum (FWHM). The laser beam profile was analyzed with a beam viewer (LaserCam-HR, Coherent Inc.). The most

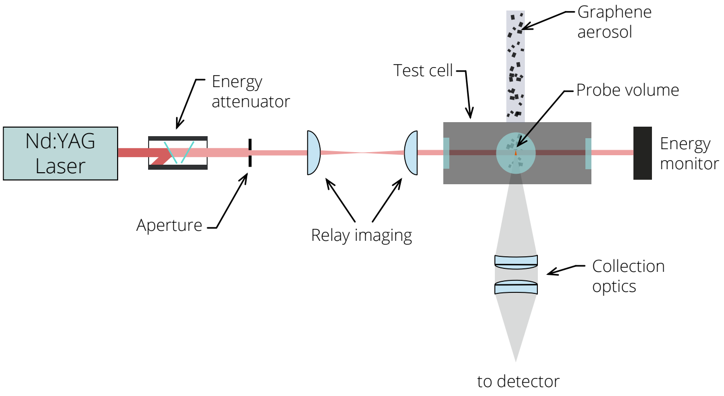

Figure 5.2 Laser-induced incandescence excitation setup attached to the flow-through test cell, side-view. Collection optics are oriented perpendicular to the drawing plane.

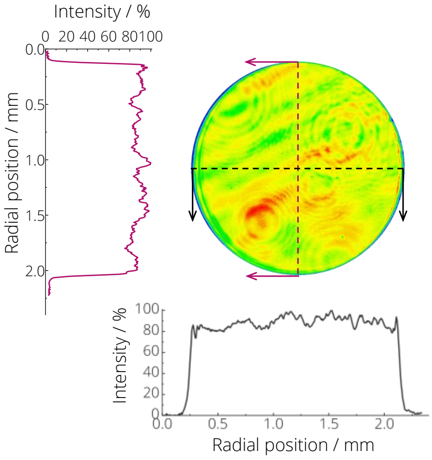

Figure 5.3 Averaged laser pulse energy profile in the probe volume when using the Continuum: Powerlite 7000 laser, 2-mm aperture, and relay imaging with two lenses. The resulting profile is close to top-hat.

homogeneous part of the beam was selected using a 2 mm diameter aperture that was relay-imaged to the measurement location using a 1:1 telescope. The resulting spatial beam profile was analyzed before each series of experiments and found to be stable and close to top-hat (Figure 5.3). The temporal spread over the 2-mm diameter laser beam is less than 600 ps and hence neglected [171]. The laser energy was controlled by an angle-dependent optical attenuator and measured using an energy meter (Coherent J-50MB-YAG sensor and FieldMax II-TOP meter).

Figure 5.4 shows the two detection systems used in these experiments: The first one consisted of four photomultiplier tubes (PMTs); the second one consisted of a spectrometer connected to a streak unit and a charge-coupled device (CCD) camera, which combined comprise the streak-camera setup. Both systems were triggered by a pulse generator (Stanford Research Systems, DG645, pulse jitter below 50 ps) at a fixed delay relative to the laser pulse. In the PMT setup, two 50.8 mm diameter achromatic doublets with focal lengths of 100 and 150 mm collected and focused the incandescence from the heated nanoparticles onto a 1000-µm core-diameter fiber (Thorlabs Inc.). The collected light was collimated and guided through three dichroic mirrors (Semrock FF740-Di01, FF605-

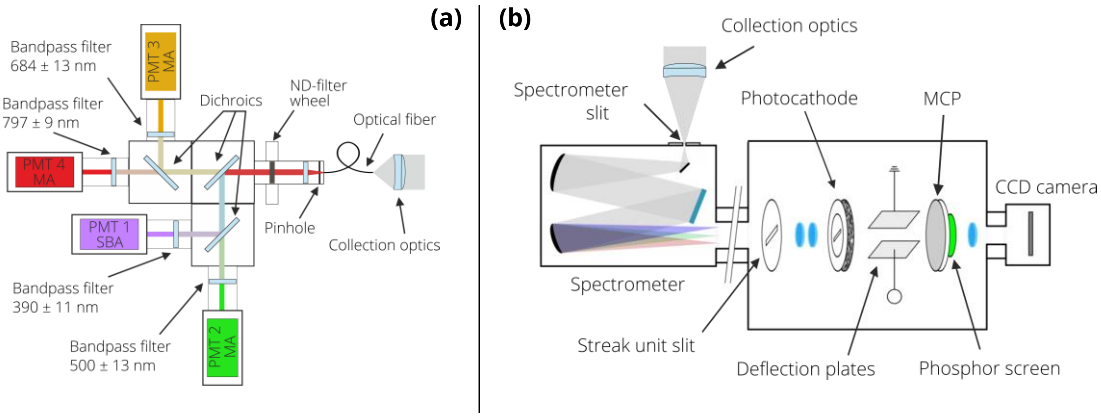

Figure 5.4 TiRe-LII detection setups, top-view: (a) four-color PMTs system; (b) streak camera system. PMT: photomultiplier tube; MA: multi-alkali photocathode; SBA: super bi-alkali photocathode; ND: neutral density; MCP: micro-channel plate.

Di02, and FF458-Di01) and then focused on four gated PMTs: three with a multi-alkali (MA) photocathode (Hamamatsu H11526-20) and one with a super bi-alkali (SBA) photocathode (Hamamatsu H11526-110). Each PMT was equipped with a unique bandpass filter: 390±11 nm (Semrock FF01-390/18-25), 500 ± 13 nm (Semrock FF01-500/24), 684 ± 13 nm (Semrock FF02-684/24), and 797 ± 9 nm (Semrock FF01-800/12). A set of neutral density filters was also incorporated (79, 50, and 10 % transmission) to ensure that the PMTs were operated in their linear regime [172]. The spectral transmission of the bandpass and neutral density filters was calibrated using a stable broadband light source (LDLS EQ-99X) and a spectrometer (Ocean Optics USB-4000). A relative PMT sensitivity calibration was done using a halogen-tungsten light source mounted in an integrating sphere (LOT KW-150W), which was calibrated at the external testing service (opto.cal GmbH). A more detailed description of the PMT setup components and the calibration procedures is given elsewhere [162]. Signals were collected with a 500 MHz oscilloscope (PicoScope 6404C) with an 8-bit vertical resolution and 0.8 ns sampling intervals. The oscilloscope was triggered with a fast photodiode (Thorlabs DET10A) by detecting scattered laser light. TiRe-LII signal data acquisition, post-processing, and parts of the analysis were done using LIISim 3.0.7 software [173].

In the streak-camera setup, incandescence was collected using two 50.8-mm diameter achromatic doublets with focal lengths of 250 and 150 mm, and then focused onto the 500-µm-wide entrance slit of a spectrometer (Acton SpectraPro SP 2300, 50 grooves/mm grating blazed for 600 nm), connected to a Hamamatsu C10910 streak unit (100 µm-wide slit). A 16-bit Hamamatsu C10600 CCD camera (1344 × 1024 pixels) was attached to the streak unit to record spectrally- and temporally-resolved data. Wavelength calibration of the spectrometer was performed using a Hg/Ar calibration light source (LOT-QuantumDesign). The spectral efficiency of the setup was calibrated using the same halogen lamps mounted in an integrating sphere as was used for the PMT system calibration. An instrument response function was determined by comparing the laser pulse duration measured by the streak camera with that by a fast photodiode (Thorlabs DET10A) and found to be ~3 ns. The detection wavelength range was set to 350–820 nm.

Figure 5.5 shows typical TiRe-LII signals obtained from FLG flakes in the test cell, confirming that crumpled FLG flakes absorb energy at 1064 nm, heat up, and consequently emit broadband thermal radiation. Time-resolved signals shown in Figure 5.5 a were obtained with the four-color PMT system at a fluence of

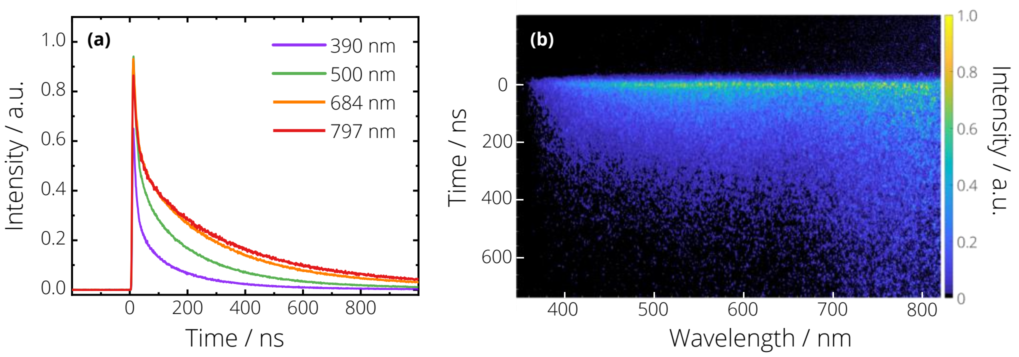

Figure 5.5 Typical TiRe-LII signals of an FLG aerosol pneumatically sampled from the reactor and measured with: (a) four-color PMT system; (b) streak camera system. Laser fluence: 1.35±0.06 mJ/mm^2. Streak camera data consist of two non-scaled overlapping spectra (350–620 and 550–820 nm).

1.35 ± 0.06 mJ/mm^2 and averaged over 200 laser shots. Figure 5.5 b shows a typical temporally- and spectrally-resolved signal collected with the streak camera at the same laser fluence and averaged over 2000 laser shots. When using a streak camera, signal accumulation for a large number of laser shots is necessary to improve the otherwise low signal-to-noise ratio. In both systems, the "0 ns" time stamp approximately (within 1—2 ns) corresponds to the moment the laser fires a pulse. The laser fluence choice was dictated by the LII signal intensity and the detection setup sensitivity. Ideally, the laser fluence should be sufficiently high to achieve a good signal-to-noise ratio, but below the sublimation regime, which could indicate that the laser is causing changes in particle morphology.

Despite the lower spectral sensitivity of the streak camera compared to the PMTs, its deployment was justified as it resolves signals temporally and spectrally, thus, visualizing potential signal interferences, e.g., from C_2^* Swan bands. TiRe-LII data are usually analyzed assuming that the measured signals are solely due to incandescence of the thermally excited nanoparticles, but this is not always true. In the case of soot, for example, under certain measurement conditions, the LII data collected over the detection wavelength range may become contaminated with emissions from polyaromatic hydrocarbons (PAHs) and other volatile compounds [174,175], as well as emissions from evaporated carbon clusters [176,177]. The detected signal may also be affected by absorption of incandescence by PAHs and other gaseous compounds present in the aerosol.

To verify that the signals detected here came solely from the incandescing FLG flakes, a series of test experiments were carried out. A membrane filter was installed upstream of the test cell, filtering out the flakes and allowing only volatile components to pass and reach the test cell. No LII signal was detected with this configuration, neither using PMTs nor with streak camera. That proves that there were no gaseous species in the aerosol absorbing 1064 nm laser radiation. Line-of-sight attenuation (LOSA) measurements were carried out with the same setup configuration (filter upstream the test cell) using a broadband light source with a diffuser plate (LDLS EQ-99X, Energetiq Technology Inc.). The light from the light source was guided through the test cell with and without the gas stream present and detected using a combination of a CCD camera and a spectrometer (Andor iXon DV887—Acton SP-150, Oxford Instruments). No absorption in the range of 350–820 nm was detected, which is the indication that there were no gaseous species in the aerosol that absorb, and hence emit, radiation in the detection range.

Figure 5.6 shows spectrally-resolved signals collected with the four-color PMT and streak camera systems at the moment of peak incandescence, 20, and 100 ns after the peak signal. Solid lines correspond to the spectral incandescence fits calculated using Equation (5.3), and symbols represent measured data. Each streak-camera signal consists of two spectra measured at different grating angles (350–620 and 550–820 nm) that are merged without rescaling. Data were truncated to 390 nm due to low detection sensitivity at lower wavelengths and smoothed in the spectral dimension using a moving average filter with a window width of 25 pixels (10 nm).

Figure 5.6 highlights that the temperatures inferred from the streak camera signals are consistently lower than those inferred from the PMTs signals. This may be attributed to the finite slit widths of the spectrometer and streak unit (500 and 100 μm, respectively) since the signal produced by a row of elements on the CCD chip corresponding to a particular moment in time is a convolution of the incident intensity entering the spectrometer from a few nanoseconds before and after the measurement time. That results in temporal blurring, which can be seen in Figure 5.5 b, where the streak camera "detects" the emitted intensity even before the laser pulse, i.e., earlier than the "0 ns" timestamp. Unfortunately, temporally-deconvolving the streak camera signal is an ill-posed problem and correcting for this effect is non-trivial and beyond the scope of this thesis. The PMT data, on the other hand,

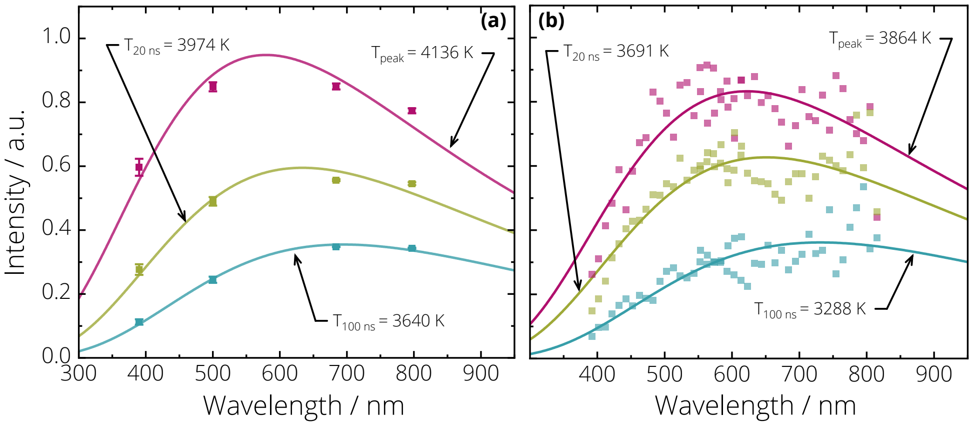

Figure 5.6 LII signals of an FLG aerosol pneumatically sampled from the reactor at three time instants: the moment of peak incandescence, 20 ns, and 100 ns after the peak signal. Signals measured with: (a) four-color PMT system; (b) streak camera system. Laser fluence: 1.35 ± 0.06 mJ/mm^2. Streak camera data consist of two non-scaled overlapping spectra (350–620 and 550–820 nm). Solid lines denote spectral fits to the data and the symbols are the measured data. Error bars in the PMT data denote one standard deviation of the mean.

are not susceptible to this problem and provide higher signal-to-noise ratios. Consequently, all quantitative analysis in this work is done using the PMTs data.

The LII response of crumpled FLG aerosols was compared to that of soot aerosols. TiRe-LII measurements were conducted on soot nanoaggregates synthesized in the same reactor using vaporized toluene as a precursor instead of ethanol (Case 2). The *ex situ* characterization of produced soot particles was presented in Chapter 3. Experimental conditions during the TiRe-LII measurements, including laser fluence and gas pressure, were identical to those during the measurements on the FLG aerosols. The same spectral model established above for the FLG (Rayleigh limit of Mie theory, $E(\mathbf{m}_\lambda)$ independent of wavelength) was used to interpret the soot measurements.

Figure 5.7 shows the evolution of temperature and normalized incandescence signals at 797 nm for soot nanoaggregates and FLG flakes obtained at a fluence of 1.35 ± 0.06 mJ/mm^2. Although the laser fluence was the

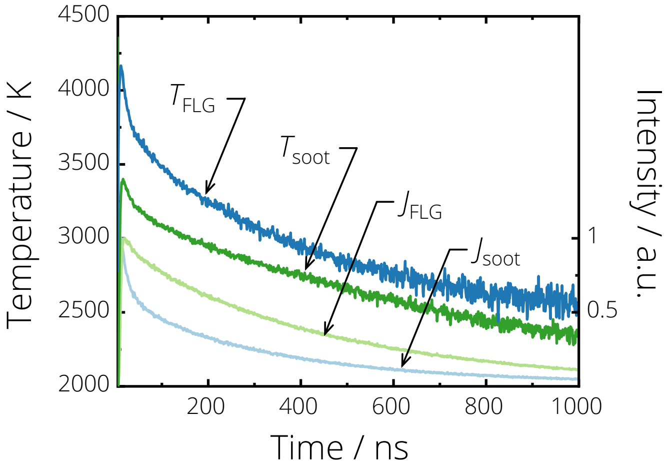

Figure 5.7 Temporal evolution of incandescence signals at 797 nm (denoted as J) and temperatures (T) of FLG and soot aerosols. Laser fluence: 1.35 ± 0.06 mJ/mm^2. The FLG aerosol heats up to higher temperatures than soot.

same in both experiments, the FLG flakes appear to reach a higher peak temperature (4135 K) than the soot particles (3400 K). Moreover, compared to soot, FLG flakes demonstrate faster incandescence signal decay, which corresponds to a faster aerosol cooldown. Both observations indicate different material properties that could be probed with TiRe-LII.

The cooling rate is defined by evaporation and conduction terms, as per Equation (5.1). For laser-heated mature graphitized soot below 3800 K, evaporative cooling is negligible, so the observed temperature decay is largely due to conductive cooling with the surrounding bath gas [165]. The outer shells of soot particles synthesized in this work (Figure 3.4 g,h) consisted of graphitized layers, same as the FLG flakes, hence, the enthalpy of vaporization of both materials is expected to be similar. In that case, the temperature decay for FLG, when below 3800 K, should also be dominated by conductive cooling. Figure 5.7 shows that the FLG flakes reach 3800 K approximately 50 ns after the incandescence peak due to evaporation and conduction and then continues to drop mainly due to conduction. As established in Equation (5.7), the conduction cooling rate depends on several materials and process parameters, including the particle/flake SSA. If folded or crumpled, the SSA of the flake reduces, which decreases the conduction cooling rate.

To avoid repetition, the quantitative conduction analysis is moved to Section 5.2.3, where it is presented together with the *in situ* TiRe-LII measurements carried out at different heights above the nozzle. The focus of the *in situ* measurements was to infer the evolution of graphene SSA while it forms and experiences morphology changes inside the reactor. The SSA values of FLG flakes and soot powders synthesized in the plasma reactor were also measured with BET analysis, which yielded $\mathrm{SSA_{FLG}} \approx 290\text{–}340\ \mathrm{m^2/g}$ and $\mathrm{SSA_{soot}} \approx 100\text{–}130\ \mathrm{m^2/g}$. Two–threefold difference in materials SSA explains different conduction cooling rates. Hence, TiRe-LII can potentially be used to estimate the level of graphene crumpledness, which has a significant influence on the characteristics of FLG in applications [30,144].

The analysis of peak temperatures and incandescence signals is usually made using fluence curves, which show how the two parameters change with laser fluence. Figure 5.8 a depicts FLG and soot temperature and incandescence (797 nm channel) fluence curves. The fluence was varied between $0.36\text{–}9.95\ \mathrm{mJ/mm^2}$ covering three distinct regimes, as defined by Sipkens et al. [178]: The low fluence/linear regime shown as a green shaded area, the moderate fluence/transition regime shown in yellow, and the high fluence/plateau (i.e., evaporation or sublimation) regime shown in red.

In the low-fluence regime (Figure 5.8 b), the evaporation term is assumed to be negligible over the laser pulse duration. Thus, the laser energy absorbed by the nanoparticles is equal to the change in sensible heat. Assuming the Rayleigh regime and that the majority of laser energy is absorbed by the time the particle/flake reaches its peak temperature [145,178]

$$q_{\mathrm{abs}} = \frac{\pi d_{\mathrm{p,eff}}^{3}}{\lambda_{\mathrm{l}}} E\left(\mathrm{m}_{\lambda_{\mathrm{l}}}\right) F_{0} = \left(T_{\mathrm{peak}} - T_{\mathrm{g}}\right) \rho c_{\mathrm{p}} \frac{\pi d_{\mathrm{p,eff}}^{3}}{6}, \tag{5.11}$$

where λ_{l} is the laser wavelength, $F0$ is the laser fluence, and T_{peak} is the particle peak temperature, which shows that the peak temperature increases nearly linearly with increasing fluence. The nanoparticle/flake volume appears on both sides of the Equation (5.11) and therefore any particle-size influence cancels out.

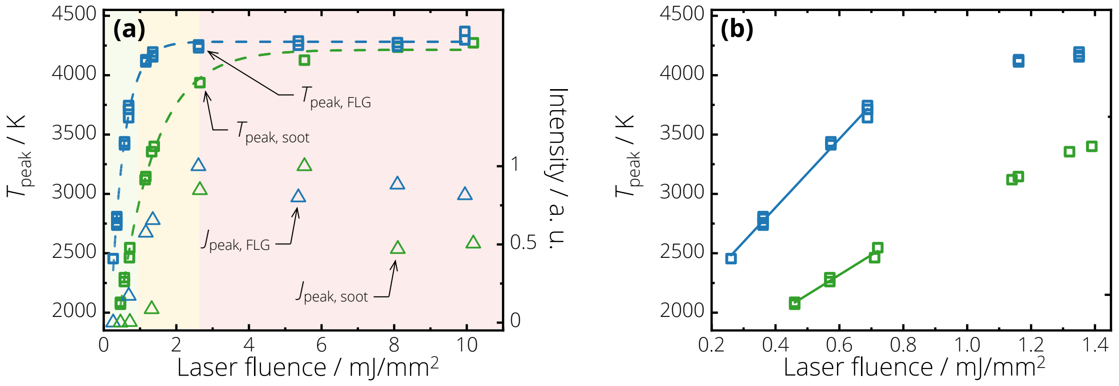

Figure 5.8 Peak temperatures and peak incandescence of FLG and soot at 797 nm versus laser fluence. (a) fluence curves between 0.36–9.95 mJ/mm^2. Shaded green area denotes the low fluence/linear regime, yellow: moderate fluence/transition regime, red: high fluence/plateau regime; (b) low fluence/linear regime (<1 mJ/mm^2), enlarged. FLG flakes heat up to higher temperatures than soot particles at the same laser fluence and reach the sublimation regime at 2–2.5 mJ/mm^2 opposed to 5 mJ/mm^2 for soot, indicating a larger $E(\mathbf{m}_{1064})$. Dashed lines are to guide the eye.

When comparing the experiments for soot and FLG conducted at the same low laser fluence below 1.0 mJ/mm^2 (Figure 5.8 b), FLG reaches higher peak temperatures. By analyzing the Equation (5.11), it is noted that the gas temperature was the same for the soot and FLG experiments. Theoretical calculations and experiments show that at temperatures above 100 K the specific heat capacity of graphene matches that of graphite [5,179], where the latter is being commonly used as reference material for soot LII [145,167].

Therefore, the higher peak temperatures of FLG compared to soot at the same low laser fluence indicates that either: (i) FLG absorbs radiation at 1064 nm more efficiently than soot, i.e., having larger $E(\mathbf{m}_{1064})$; or (ii) the assumptions used to derive the spectroscopic model, i.e., the Rayleigh approximation and a spectrally-uniform $E(\mathbf{m}_{\lambda})$ are faulty. The Rayleigh approximation for crumpled FLG flakes was shown to be valid using the RDG and DDA simulations in Chapter 4. The $E(\mathbf{m}_{\lambda})$ approximation is less obvious. Several studies reported a nearly-uniform $E(\mathbf{m}_{\lambda})$ of flat graphene between 400 and 800 nm [126,128,180–182], although, admittedly, the refractive index of crumpled FLG may behave differently from flat graphene sheets. Experiments with aerosolized crumpled FLG flakes presented in Chapter 3 showed $E(\mathbf{m}_{\lambda}) \propto \lambda^{0.45}$ in the λ range of 370–950 nm. However, it was unclear if that effect was caused by the material alteration due to the aerosolization. Even so, when calculating a temperature trace assuming $E(\mathbf{m}_{\lambda}) \propto \lambda^{0.45}$, the peak temperature is 4475 K (Figure 5.9), which is even higher than if assuming $E(\mathbf{m}_{\lambda}) = \text{const}$ (4135 K). Hence, a wavelength-dependent $E(\mathbf{m}_{\lambda})$ would enhance the discrepancy between the peak temperatures of crumpled FLG and soot.

The only explanation left that could explain the different peak temperatures is the larger $E(\mathbf{m}_{1064})$ of crumpled FLG flakes compared to that of soot particles. In Chapter 4, it was shown that the aerosolized crumpled FGL absorbs visible light more efficiently than soot, though, the effect of the aerosolization process was uncertain. In this chapter, the crumpled FLG aerosols were probed by sampling them pneumatically downstream of the reactor,

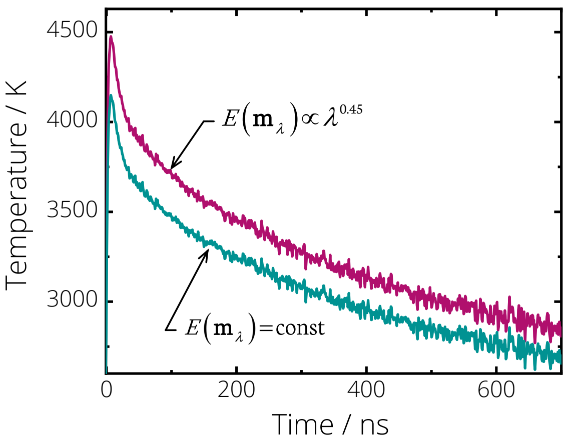

Figure 5.9 Temperature traces of an FLG aerosol calculated using different $E(\mathbf{m}_\lambda)$. Laser fluence: 1.35 ± 0.06 mJ/mm^2. Wavelength-dependent $E(\mathbf{m}_\lambda)$ of aerosolized crumpled FLG flakes was measured with an aethalometer, as presented in Chapter 4, and resulted in a higher peak temperature compared to $E(\mathbf{m}_\lambda)$ = const.

i.e., without external aerosolization, and the same effect of more efficient light absorption (at 1064 nm) was observed. To conclude, the crumpled FLG flakes have a larger $E(\mathbf{m}_{1064})$ compared to soot, and thus heat up to higher peak temperatures at the same laser fluence.

In the high fluence regime (red in Figure 5.8), the LII signal reaches its maximum intensity after which it drops due to the reduced nanoparticle mass caused by evaporation. The laser-induced evaporation threshold, i.e., the ablation threshold, is an important materials parameter in different applications, including laser lithography, laser machining, and laser sputtering. For crumpled FLG fakes, the incandescence signal peaks at approximately 2–2.5 mJ/mm^2, while for soot aerosol the incandescence signal reaches its maximum at about 5 mJ/mm^2. The pyrometric temperature increases at a much slower rate at high fluences also due to evaporation, and eventually "plateaus" at the temperature of around 4250 K for both materials. For FLG, this transition occurs at a laser fluence of approximately 2–2.5 mJ/mm^2, while for soot particles it occurs at approximately 5 mJ/mm^2. This observation again suggests larger $E(\mathbf{m}_{1064})$ of crumpled FLG flakes at 1064 nm compared to soot.

Overall, the distinct response of laser-heated FLG flakes and soot nanoparticles suggests a mechanism for classifying carbonaceous nanoparticle types within the aerosol phase. The distinction can be assessed by comparing key LII characteristics: The conduction cooling rates that are related to the particle SSA, and the laser fluence curves that are linked to the material absorption cross-section at the laser wavelength. The ability to distinguish FLG from other carbonaceous nanomaterials is particularly important for the gas-phase synthesis routes since a range of particle types are possible within the reactor depending on the local stoichiometry and operating conditions.

5.2.2 Mass and volume fraction measurements

The second set of LII measurements was carried out at the Metrology Lab of the National Research Council (NRC) in Ottawa using the apparatus shown in Figure 5.10. The FLG powder synthesized in the plasma reactor was dispersed in pure ethanol (≥ 99.5% purity) and ultrasonicated for 15 minutes to form a nanocolloid. The graphene

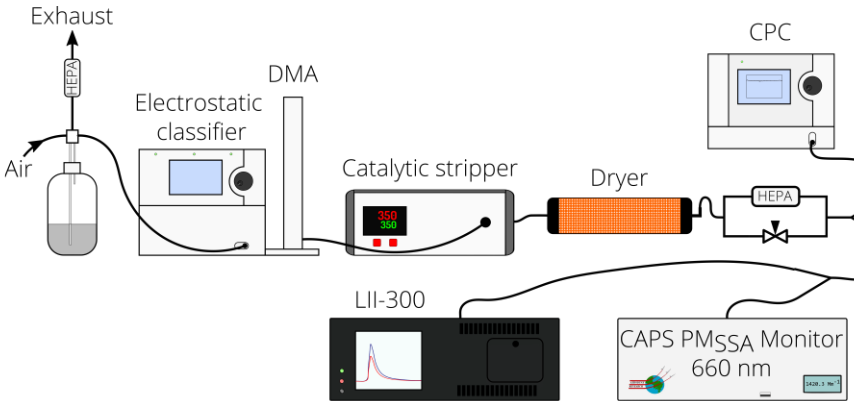

Figure 5.10 Experimental setup used to measure FGL aerosol mass concentration (volume fraction). HEPA: high-efficiency particulate air filter, CPC: condensation particle counter, CAPS PM$_{\text{SSA}}$ monitor: Cavity Attenuation Phase Shift Particulate Matter Single Scattering Albedo monitor, LII-300: commercial laser-induced incandescence measurements device.

nanocolloid was then nebulized using a Collison nebulizer (Model 3076, TSI Inc.) in recirculation mode, with filtered air at a pressure of 241 kPa as the motive gas. The nebulizer output was split between a sampling line and an exhaust line at atmospheric pressure equipped with a high-efficiency particulate air (HEPA) filter.

The FLG–ethanol aerosol was passed through an electrostatic classifier (TSI model 3080, TSI Inc.) equipped with a long differential mobility analyzer column (DMA) used as a dilution system as suggested by Owen et al [86]. The sample flow of 1.5 standard liters per minute (slm) was diluted with 1.5 slm of sheath air flow. The DMA size selection was centered at 200 nm (for aerosol size classification, see Section 4.1), but, because of the small sheath-to-sample flow rate ratio, flakes of a relatively wide mobility diameter range may pass through the DMA. The diluted FLG aerosol then went through a catalytic stripper (CS 10, Catalytic Instruments) operated at 350 °C, followed by a diffusion dryer to remove semi-volatile particulate matter, ethanol, and water from the aerosol. The dried graphene aerosol then passed through a HEPA filter bridge, which was used to control the flake number concentration, and thus the mass and volume fraction of the aerosol.

The aerosol flow was subsequently split between a condensation particle counter (CPC, TSI model 3776, TSI Inc.) operated at 0.33 slm, an LII-300 instrument (Artium Inc.) operated at 0.94 slm, and a cavity attenuation phase shift particulate matter single scattering albedo monitor (CAPS PM$_{\text{SSA}}$ 660 nm, Aerodyne Inc.) operated at 0.94 slm. The CPC measures particle number concentrations by laser-light scattering and the CAPS PM$_{\text{SSA}}$ monitor measures the absorption coefficient of the nanoparticle, which is taken to be proportional to the mass concentration in the Rayleigh regime [103,183]. Hence, the CAPS PM$_{\text{SSA}}$ monitor provides an independent way of measuring the flake mass fraction. Both devices were described in more detail in the aerosol characterization study in Chapter 4.

The Artium LII-300 system uses an Nd:YAG, 1064 nm, 15 ns FWHM laser operated at 10 Hz for particle heating. An aperture and a relay imaging system shape the laser beam into a 2.85 mm^2 square top-hat profile at the probe volume, as shown in Figure 5.11. The incandescence signals were detected by two photomultipliers equipped with bandpass filters centered at 442 and 716 nm with 46 and 40 nm FWHM respectively.

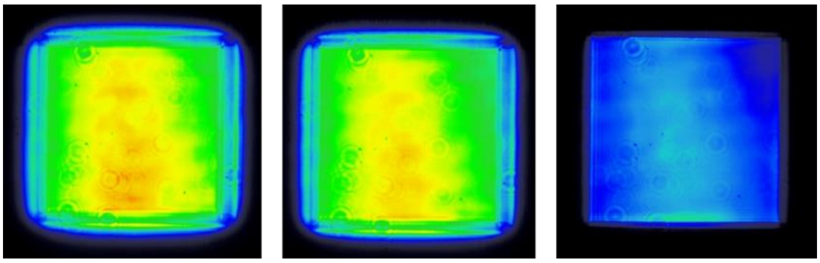

Figure 5.11 Averaged laser energy distributions at different fluences in the probe volume when using the LII-300 instrument (Artium Inc). The resulting profiles are close to top-hat.

All instrument flows were verified using a Gilibrator-2 flow standard (Sensidyne) and corrected for the temperature and pressure. The devices were connected using electrically conductive carbon-impregnated silicone tubing to avoid electrostatic particle losses.

Figure 5.12 shows the magnitudes of the LII signals at two detection wavelengths and absorption coefficients in inverse meters measured with the CAPS PM_{SSA} monitor versus an absolute number of flakes per cubic centimeter measured with the CPC. The laser fluence of 2.04 mJ/mm^2 was chosen so that it is close to the peak temperature plateau regime (Figure 5.8), as in this regime the LII signal intensity remains relatively insensitive to small fluctuations in the laser energy [146]. The error bars in both directions, which correspond to the standard deviation of the mean, are too small to be seen in the figure.

Figure 5.12 shows that the inferred absorption coefficient, $b_{\mathrm{abs,660\,nm}}$, varies in linear proportion to the flakes loading in the aerosol. The peak incandescence also varies in proportion to both the CPC-derived number density and the absorption coefficient. This highlights the potential for LII to provide highly spatially (~1 mm) and temporally (~20 Hz) resolved measurements of graphene aerosol mass and volume fraction. However, one must note that for quantitative measurements, the setup needs to be calibrated by either using a system with a known parti-

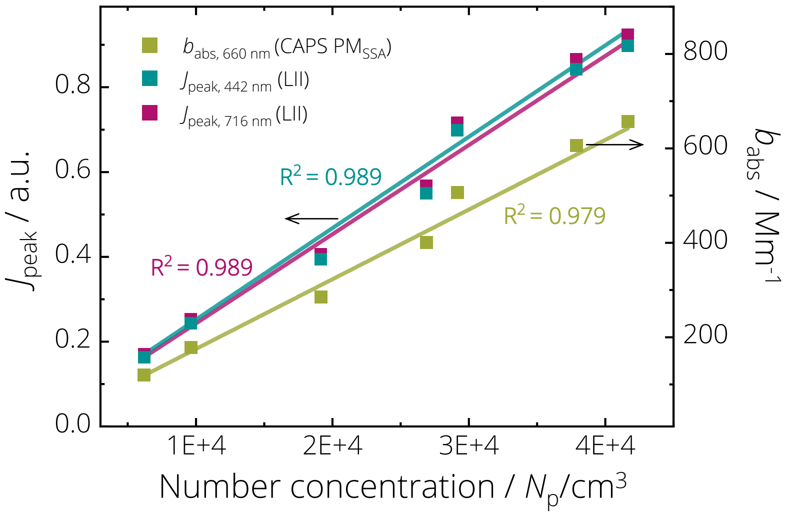

Figure 5.12 Magnitude of the incandescence signals (LII) and absorption coefficients (CAPS PM_{SSA}) at different flake concentration levels. The solid lines are the linear fits to the data. Error bars, which denote the standard deviation of the mean, are too small to be seen.

cle volume fraction, e.g., target flames and aerosol generators, or with an independent concentration measurement, e.g., using the CPC as shown here. A calibration-independent volume fraction measurements are also possible by measuring the absolute LII signal and comparing it to the theoretical incandescence per particle, which has been done for soot [146]. In the case of FLG aerosols, that would require a comprehensive spectroscopic model that quantitatively connects the spectral absorption cross-section of flakes with their morphology, such as lateral size, thickness, crumpledness, etc.

5.2.3 *In situ* measurements of the specific surface area

The third set of TiRe-LII experiments on crumpled FLG aerosols has been carried out *in situ* in the microwave-plasma reactor at various heights above the nozzle (HAN), as shown in Figure 5.13. The spatially-resolved measurements in the post-plasma region enable probing the evolution of flake morphology, in particular, specific surface area (SSA). The SSA is a general material property defined as the surface area per unit of mass (m^2/g). In the context of TiRe-LII, the SSA is the surface area of a particle/flake available for conductive heat transfer, A_{cond}, per unit of mass.

An ideal defect-free single-layer graphene has an SSA of 2630 m^2/g [3]. However, in practice, flakes may consist of several graphene layers and be partially crumpled, which decreases the SSA. Hence, the SSA of graphene can be a marker of flake thickness and level of crumpledness, all of which demonstrated a significant influence on FLG performance in multiple applications [30,78,80,144]. Since the SSA is a key performance metric for graphene, a quick and reliable technique for measuring this parameter is desired. Moreover, there is still no detailed understanding of the dynamics of graphene crumpling within gas-phase reactors, e.g., it is not clear if the crumpling occurs in the gas-phase or after the flakes were sampled on a filter surface.

Various techniques are available to measure the SSA, e.g., BET and TEM. However, BET is an *ex situ* technique and requires hundreds of milligrams of a sample. TEM is also an *ex situ* and time-consuming analysis; moreover, it can only be used to determine the projected surface area and not the crumpledness of the particle.

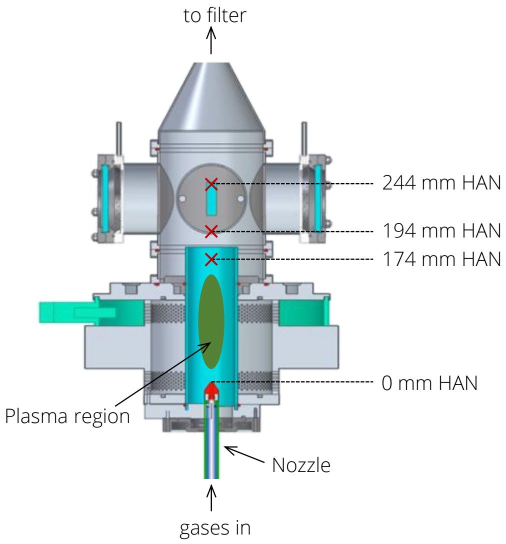

Figure 5.13 Half section of the gas-phase microwave plasma reactor with the TiRe-LII measurement positions shown as red crosses at different heights above the nozzle (HAN).

TiRe-LII can measure the SSA of the nanoparticle online and *in situ*. The flake SSA can be estimated based on the inferred conduction cooling rate, due to gas molecules scattering on the accessible flake surface. When folded or crumpled, the SSA of the flake reduces, which decreases the conduction cooling rate.

Two aerosols were investigated: FLG flakes synthesized using 164 sccm of ethanol, and soot particles formed using 74 sccm of toluene. The synthesis principle and the selection of precursors and operating conditions are explained in Chapter 3. In both cases, the microwave power was set to 1.6 kW and the pressure inside the reactor to 700 mbar, which gives an acceptable tradeoff between particle torch stability (Figure 3.2, inset) and the TiRe-LII signal-to-noise ratio. The TiRe-LII measurements were carried out at three HAN: 174, 194, and 244 mm (Figure 5.13). The choice of measurement positions was intended to cover the range of flake morphologies as they form and grow downstream of the plasma but was also dictated by the limitations of optical access. The lowest position that permits optical access was 174 mm HAN. The TiRe-LII excitation and detection setups used here were the same as in Section 5.2.1 (Figure 5.2 and Figure 5.4) except the flakes were probed inside the gas-phase reactor and not in the test cell. For each experimental run, 200 signals, i.e., signals within 20 s, were collected.

The conduction regime depends on the Knudsen number, $Kn = \lambda_{\mathrm{g}}/L$. Considering the process gas flow rates (45 slm of Ar, 1 slm of H_2), here, the atmosphere was modeled as consisting entirely of Ar. The mean free path of Ar is ~800 nm when adapting an expression for an ideal gas at the experimental conditions used here [165], and the characteristic flake size is ~300 nm (Figure 3.7). Hence, $Kn > 1$, which means that the conduction heat transfer occurs in the free-molecular regime. In that case, if the conduction is the dominant heat transfer mechanism, the particle energy balance can be written, as per Equations (5.7) and (5.8):

$$q_{\mathrm{cond}} = -\alpha A_{\mathrm{cond}} \frac{p_{\mathrm{g}} c_{\mathrm{g}}}{2T_{\mathrm{g}}} \left(T_{\mathrm{p}} - T_{\mathrm{g}}\right) = m_{\mathrm{p}} c_{p} \frac{\mathrm{d}T_{\mathrm{p}}}{\mathrm{d}t}\ , \tag{5.12}$$

where gas properties were taken for Ar; p_{g} = 700 mbar; gas temperatures, T_{g}, were taken to be pyrometrically determined pyrometrically-determined particle temperatures before the laser pulse. The same TiRe-LII detection setup was employed to collect the incandescence from particles before the laser pulse. The SSA is then found as

$$\mathrm{SSA} = \frac{A_{\mathrm{cond}}}{m_{\mathrm{p}}} = -\frac{\mathrm{d}\left[\ln\left(T_{\mathrm{p}} - T_{\mathrm{g}}\right)\right]}{\mathrm{d}t} \frac{c_{p} 2T_{\mathrm{g}}}{\alpha p_{\mathrm{g}} \sqrt{8 k_{\mathrm{B}} T_{\mathrm{g}} / (\pi m_{\mathrm{g}})}}\ , \tag{5.13}$$

where the $\mathrm{d}[\ln(T_{\mathrm{p}} - T_{\mathrm{g}})]/\mathrm{d}t$ term is determined by linear regression of the corresponding temperature decay (Figure 5.14) after Liu et al. [184] and Daun et al. [185]. The α value is expected to be 0.41 ± 0.05 for both graphene and soot in Ar, based on the experimental and molecular dynamics studies of Ar–graphene interaction [185–187]. The specific heat capacities of soot and graphene were evaluated from the Fried and Howard correlations for graphite [188] assuming ± 10 % uncertainty.

The TiRe-LII signals were analyzed in the timespan of 150–400 ns after the peak incandescence to avoid any evaporation cooling and signal contamination from non-thermal types of emission [177,189], which typically occur in the first tens of nanoseconds after the laser pulse. Thus, the studied time region of 150–400 ns after the peak incandescence relates to the effective temperature curve driven solely by the conduction heat transfer.

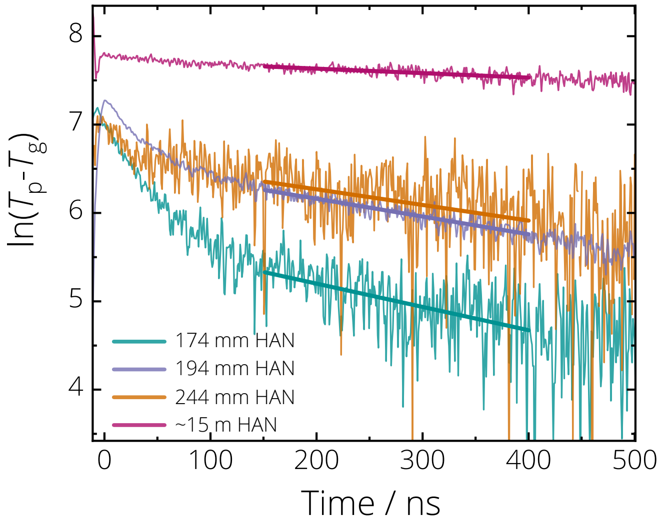

Figure 5.14 Mean temperatures of crumpled FLG flakes inferred with the TiRe-LII, semilog-scale. Measurements were conducted at different heights above the nozzle representing different flake morphology. Zero timestamp corresponds to the peak incandescence. The 150–400 ns part of the curves was linearly fitted to yield $d[\ln(T_p - T_g)]/dt$ values required for the SSA calculation.

In addition to three experiments conducted inside the reactor, a further experiment was carried out at a distance of approximately 15 m from the reactor in a measurement cell, as described in Section 5.2.1. The aerosol was synthesized in an identical manner and was transferred through a 15-meter vacuum-tight tube to the cell where it was probed with TiRe-LII. That experiment was conducted at 400 mbar pressure in Ar atmosphere and Tg = 298 K, which results in a free-molecular conduction regime. Some of the experimental parameters and corresponding SSA values are listed in Table 5.1. The errors denote the standard deviation of the mean. The SSA lower and upper bounds (LB, UB) were found by calculating the SSA values for all the experiments with the standard deviations of the mean propagated from Equation (5.13) and taking the lowest and highest obtained values.

Figure 5.15 shows that the SSA of FLG flakes is consistently larger than that of soot particles and that for both aerosols, the SSA decreases with HAN. For graphene, larger SSA compared to soot is expected since it is a 2D material with a high surface-to-mass ratio. The decrease of SSA with HAN can be explained by the increasing number of graphene layers and flake crumpledness. When crumpled, the surface area of a flake available for conductive heat transfer decreases, while its mass remains the same, i.e., the SSA decreases. When the flake grows in

Table 5.1 The experimental parameters and corresponding SSA values of FLG flakes and soot particles as calculated from Equation (5.13). LB and UB denote the lower and upper SSA bounds.

HAN / mm	**T_g / K**		**p_g / mbar**		**Mean SSA (LB, UB) / m²/g**	
	FLG	soot	FLG	soot	FLG	soot
174	2050 ± 50	1650 ± 50	700	700	800 (616, 997)	335 (248, 473)
194	1900 ± 50	1500 ± 50	700	700	720 (488, 894)	236 (122, 351)
244	1750 ± 100	1200 ± 200	700	700	350 (219, 568)	195 (147, 241)
15000	298 ± 5	298 ± 5	400	400	86 (65, 120)	111 (62, 172)

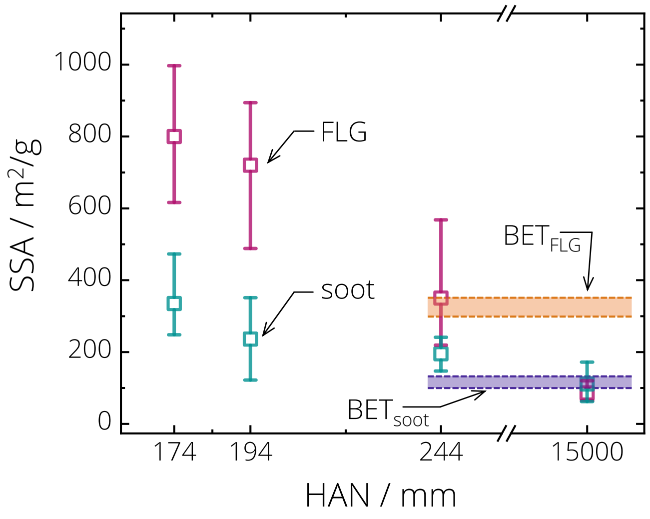

Figure 5.15 Specific surface areas of FLG flakes and soot particles probed with TiRe-LII at different heights above the nozzle (HAN). Shaded areas denote the BET analysis of powders sampled from the filter. HAN 15000 mm represents an experiment in which the aerosol was pneumatically sampled from the reactor to a measurement cell through a ~15-m tube. The error bars denote the lower and upper bounds of SSA.

thickness, i.e., the number of graphene layers increases, the flake mass increases, while the active surface area remains the same, i.e., again, the SSA decreases. For example, an ideal defect-free single-layer graphene has an SSA of 2630 m^2/g [3], which is approximately three times larger than what was measured here at 174 mm HAN. A flat flake should consist of 3 layers to have the SSA of 877 m^2/g, which is within the range of what was measured. However, another flake with the same SSA can consist of less than 3 layers and be crumpled. The TiRe-LII diagnostic is not able to distinguish between two such flakes.

To decouple the influence of thickness and crumpledness on graphene SSA, thermophoretic sampling at different HAN was carried out. The sampling procedure and detailed TEM analysis are beyond the scope of this thesis and are described elsewhere [190]. Here, thermophoretic TEM sampling was used as a tool complementary to TiRe-LII. Flakes collected at HAN = 124, 144, 194, and 244 mm and analyzed with TEM are shown in Figure 5.16, upper row. The images show that initially, at the lower HAN, flat and thin graphene sheets are formed. However, due to thermal vibrations, defects, and edge instabilities, the freestanding flat graphene sheets become unstable and tend to crumple [136], which is depicted here in samples collected at HAN above 124 mm. The number of observed flakes that are entirely flat drastically decreases with increasing HAN. Regarding the thickness of the sheet, no significant change was observed in samples between 144–244 mm HAN. Therefore, the decrease of graphene SSA measured with TiRe-LII between HAN = 174–244 mm (and further to ~15 m) should be mainly explained by flakes getting more crumpled. That observation also suggests that the flakes crumple in the gas phase while moving downstream of the post-plasma region, and not on the surface of the membrane filter or TEM grid, upon which the flakes are deposited. Overall, these results demonstrate that TiRe-LII can measure graphene SSA *in situ*, which can be an indication of flake crumpledness when independent data on flake thickness are available.

For soot aggregates consisting of spherical primary particles, initial nuclei are formed through the clustering of moderate-size polyaromatic hydrocarbons into curved structures [191]. That early stage of soot formation cannot be probed with TiRe-LII and TEM. Further surface and mass growth can be explained by the H-abstraction

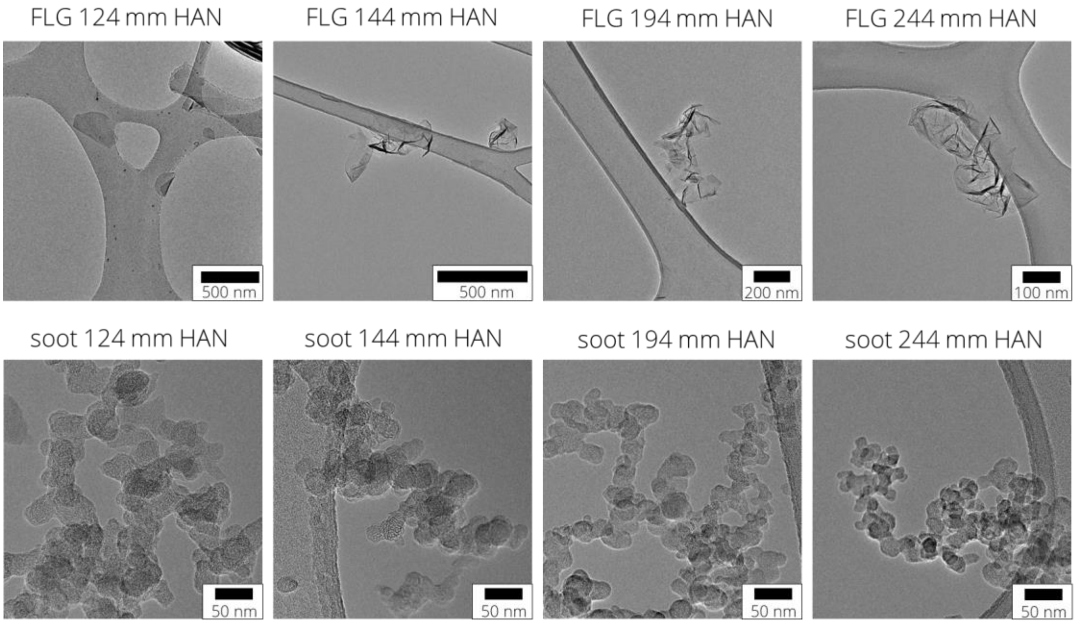

Figure 5.16 TEM images of FLG flakes and soot particles sampled thermophoretically inside the plasma reactor at different HAN. Graphene flakes initially form as flat sheets and then crumple downstream the gas flow. Soot particles slightly grow in diameter and additionally coalesce and aggregate with HAN.

C_2H_2-addition (HACA) mechanism, sedimentation of other gaseous species on the particle surface, coalescence, oxidation, and aggregation [191]. The growth of a primary spherical soot particle causes its surface area and mass to increase with diameter, $SA_p \propto d_p^2$, $m_p \propto d_p^3$. Hence, the $SSA = SA_p/m_p \propto d_p^{-1}$. Analysis of TEM images (Figure 5.16, lower row) shows that soot particles slightly grow in diameter [190], although not enough to explain the decreasing SSA trend. The decrease of soot SSA with HAN shown in Figure 5.15 is much steeper than d_p^{-1}. This effect is attributed to particle coalescence and aggregation, which lead to merging and shielding effects, hence further shrinking of the SSA. As is the case with the FLG flakes, TiRe-LII cannot differentiate between the primary particle growth and merging/shielding effects. In general, the combined TiRe-LII and TEM analysis revealed that primary soot particles grow and experience coalescence and aggregation throughout the whole measurement region.

Figure 5.15 also shows the SSA values of FLG and soot powders measured with BET (shaded areas). The BET analysis was performed several times for powders synthesized at 700 and 1000 mbar and yielded $SSA_{FLG} \approx 290$–$340\ m^2/g$ and $SSA_{soot} \approx 100$–$130\ m^2/g$. Since the BET measurements were performed on the powders, i.e., flakes/particles in their final morphological state, it is reasonable to compare the results with TiRe-LII measurements performed either at HAN ~15 m or HAN = 244 mm, and not at lower heights inside the reactor where aerosols still experienced morphology changes, as shown in Figure 5.16. Nevertheless, the comparison between the two methods is not straightforward.

The fundamental difference between BET and TiRe-LII is that the BET-measured surface area includes pores, while TiRe-LII measures only the active surface area, which can be “reached” by surrounding gas molecules. Considering that the FLG flakes and soot particles synthesized in this work appear to have a porous structure with parts of surface area that likely do not participate in the conductive heat exchange, the BET SSA could be larger than that of TiRe-LII. Apart from that, the flakes and particles at HAN = 244 mm, although visually similar to what was sampled further downstream with the electrostatic precipitator (Figure 3.7), could still go through subsequent morphology changes when cooling down from elevated gas temperatures to room temperature. In that case, it would be logical to compare BET results with TiRe-LII at ~15 m. However, while being transferred from the reactor to the test cell at HAN ~15 m, the smaller flakes and particles likely diffused to the pipe walls [192], leaving larger particles with smaller SSA in the aerosol, which were subsequently probed with TiRe-LII. Unfortunately, no electrostatic precipitation sampling was carried out at HAN ~15 m, which could help resolve morphology uncertainties discussed here.

Keeping in mind the discussed issues, Figure 5.15 shows a reasonable SSA agreement between the BET and TiRe-LII for soot. Between HAN = 244–15000 mm, TiRe-LII SSA_{soot} was estimated to be 111–195 m^2/g, while BET $SSA_{soot} \approx$ 100–130 m^2/g. In the case of FLG flakes, the BET $SSA_{FLG} \approx$ 290–340 m^2/g was closer to the one probed with TiRe-LII at HAN = 244 mm (mean of 337 m^2/g), while overestimating the TiRe-LII results at HAN ~15 m (mean of 86 m^2/g) by 3–4 times. Such a significant drop of SSA_{FLG} between HAN = 244 mm and ~15 m likely occurred due to the discussed above flakes losses in the 15-m long transfer line.

5.3 Conclusions

This chapter showed how the TiRe-LII technique can be used to characterize FLG aerosols. First, it was demonstrated that crumpled FLG flakes absorb laser light at 1064 nm and emit broadband thermal radiation. Further, the LII signal magnitude was found to be linearly dependent on the FLG flake number concentration, suggesting the use of the technique for quantitative mass and volume fraction measurements. Finally, using TiRe-LII, the evolution of FLG flakes morphologies was analyzed through *in situ* SSA measurements, which can be translated into the estimate of flake crumpledness. In the context of gas-phase graphene synthesis, the graphene sheets, while initially flat, lose their mechanical stability and crumple in the gas flow before being sampled on a filter or TEM grid for further analysis.

Additionally, graphene LII response was compared to that of soot aggregates. Pyrometric temperatures were obtained from the temporally- and spectrally-resolved LII signals, and the differences in temperature evolutions between FLG and soot were attributed to the larger $E(\mathbf{m}_{1064})$ and SSA of FLG. These results are consistent with the other diagnostics used in this thesis. The BET analysis confirmed a larger SSA of FLG compared to soot. The aerosol optical properties measurements presented in Chapter 4 showed that $MAC_{FLG,\lambda}$ is larger than $MAC_{soot,\lambda}$ between 370–950 nm. Consequently, the results presented in this chapter demonstrate the potential for TiRe-LII to differentiate graphene flakes from soot particles online.

Chapter 6
FTIR diagnostics

This chapter presents the use of Fourier-transform infrared (FTIR) spectroscopy as an *in situ* line-of-sight absorption technique to investigate graphene synthesis in the microwave plasma. While TiRe-LII focuses on the particle phase, FTIR spectroscopy allows identifying and quantifying gaseous species involved in the synthesis, thus providing insight into the process kinetics.

The FTIR absorption spectroscopy involves an IR-light source that shines radiation through a sample at multiple frequencies simultaneously using a Michelsen interferometer. Different species that are present in the sample or along the line-of-sight absorb IR radiation at frequencies that induce their characteristic rovibrational states and hence, different transmission spectra are produced, which are recorded with an IR detector. The absorption peak positions in the recorded spectra provide information on the sample's chemical composition while the intensity and FWHM of peaks allow for measuring species concentrations and temperatures. In this work, the IR beam is guided through the synthesis reactor, where graphene and multiple gaseous by-products are formed, thus allowing to obtain information on the process kinetics *in situ*.

Earlier attempts were made to use FTIR in the context of gas-phase graphene synthesis [55–57,63,193], however, these studies focused on measurements in the reactor off-gas. Here, spectrally-resolved line-of-sight absorption is measured in the reactor zone where, presumably, the graphene flakes nucleate and grow. Measurements in the reactor zone are combined with measurements across the graphene-containing product aerosol in the reactor off-gas. Toman et al. [56] used an FTIR to investigate the influence of ethanol flow rate and delivered microwave power on the formation of gaseous species. Results presented in this chapter expand on that study by examining different precursors that lead to the formation of either soot particles or crumpled FLG flakes and analyzing the correlation between particle morphology and FTIR results. A comprehensive parametric study of precursor chemical composition, i.e., C/H/O atomic ratio, precursor flow rate, and delivered microwave power is also carried out. Results are compared with chemical kinetics simulations and mass spectrometry measurements. The quantitative FTIR data presented in this chapter reveal the factors responsible for reaction shift from soot particles toward FLG flakes; this information provides a foundation for controlling the particle morphology. The findings of this study may also be useful for the validation and development of graphene formation mechanisms.

6.1 FTIR apparatus

Figure 6.1 shows the schematics of a setup used for the *in situ* line-of-sight FTIR absorption measurements. Measurements were done in two positions in the reactor, regarded here as “upper” and “lower” measurement positions (although not simultaneously). The lower position was located 26 cm downstream of the nozzle, i.e., 17 cm downstream of the plasma zone, and the optical access was achieved with nitrogen-flushed KBr windows installed as a

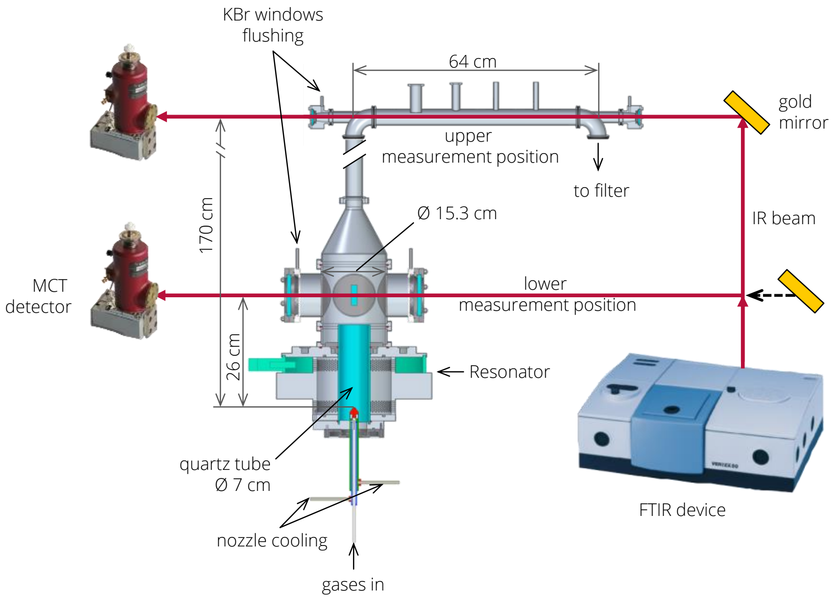

Figure 6.1 Sketch of the plasma reactor and schematics of the *in situ* Fourier-transform infrared absorption measurement. Measurements were performed in two positions in the reactor: 26 cm (denoted as "lower") and 170–234 cm (denoted as "upper") downstream of the nozzle. The absorption paths were 15.3 and 64 cm for the lower and upper measurement positions, respectively. A liquid-nitrogen cooled mercury cadmium telluride (MCT) detector was used.

cross-piece to the reactor housing. The extended cross-piece parts were shielded from the inner tube with a metal plate leaving a 5 cm × 1.5 cm open rectangle for the optical beam passage (Figure 3.2), thus limiting the absorption pathlength to the inner tube diameter of 15.3 cm. In the upper position, the synthesized particles and the gaseous species pass through a 64 cm-long horizontal tube located 170 cm downstream of the nozzle, which is also equipped with nitrogen-flushed KBr windows on both ends.

In both measurement positions, the mid-infrared beam from the FTIR spectrometer (Bruker Vertex 80) was guided with gold mirrors (Thorlabs Inc.) through the reactor and then focused with an off-axis parabolic gold mirror (Thorlabs Inc.) on a liquid-nitrogen cooled mercury cadmium telluride (MCT) detector (Bruker). Background spectra for the particle-free case were recorded at the same pressure and temperature as the measurements by flowing Ar, H_2, and N_2 through the reactor and turning the plasma on. No IR-absorbing or emitting species were observed during the background scans in the 400-8000 cm^{-1} range. Thus, the background measurements accounted only for the atmospheric absorption by H_2O vapor and CO_2 present in the beam optical path outside of the reactor. Overall, over a timespan of a few minutes, 16 background and 16 measurement spectra were recorded and averaged. The spectral resolution was varied between 0.1 and 1 cm^{-1}.

6.2 Temperature distribution in the reactor

To determine the temperature profile along the reactor center line (direction of the gas flow), measurements were carried out via optical emission spectroscopy (OES), FTIR spectroscopy, and using thermocouples at several positions inside the reactor (Figure 6.2 a). Section 6.4.2 discusses how gas temperature at the lower and upper measurement positions change with microwave power and precursor type while this section presents only the temperature

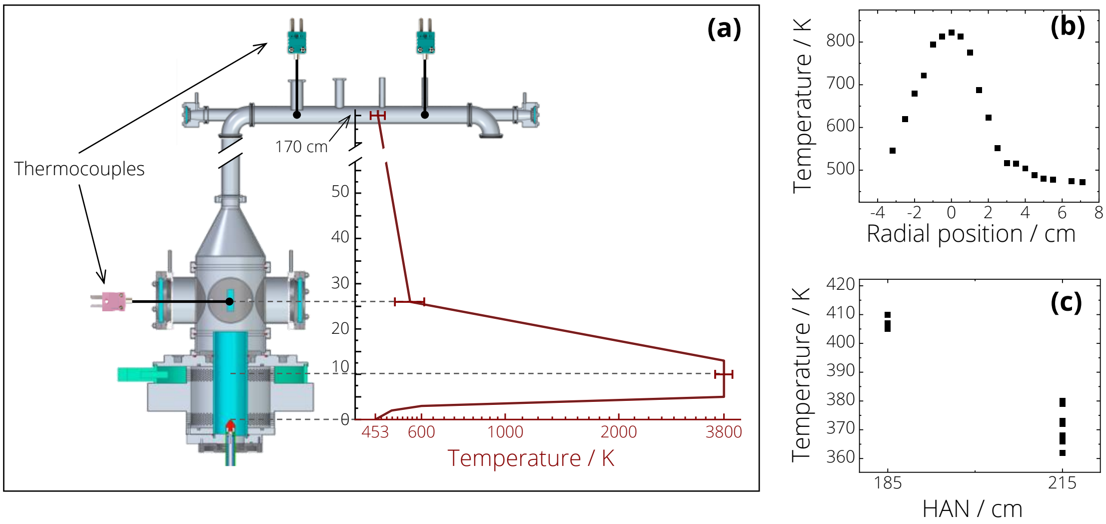

Figure 6.2 (a) Sketch of the plasma reactor and the gas temperature profile along the direction of the flow. The vertical axis shows the distance from the nozzle tip in centimeters. The reactor was operated at 1.4 kW microwave power using ethanol as a precursor. Ethanol was delivered into the reactor at 453 K. OES measurements carried out at HAN ≈ 8–10 cm yielded 3800 ± 200 K rotational temperature for the electronically excited OH* and C_2* species. FTIR measurements at HAN = 26 cm and HAN = 170–234 cm yielded 560 ± 50 and 450 ± 20 K, respectively; (b) Radial temperature distribution at HAN = 26 cm as measured with a thermocouple; (c) Temperatures at HAN = 185 and 215 cm measured with a thermocouple.

profile along the central line for Case 1 with ethanol. First, the precursor mixture was heated inside the CEM unit to 453 K and injected into the reactor through the nozzle. The gases reach the microwave resonator approximately 5 cm downstream of the nozzle tip, where the Ar/H_2 plasma is sustained. In the prior work [55], using optical emission spectroscopy, a rotational temperature of 3800 ± 200 K was determined for the electronically excited chemiluminescence species OH* and C_2* at approximately ~8–10 cm downstream of the nozzle for both ethanol and toluene precursors using microwave powers between 1.2–1.6 kW. The gas temperature was considered to equal that of the excited species in the plasma region, as plasmas at atmospheric pressures are known to be in local thermodynamic equilibrium due to high species collision rates [194]. The high-temperature plasma region was assumed to have a constant temperature over the whole length of the resonator [195], which, for this reactor, corresponds to 5–13 cm from the nozzle. After leaving the plasma zone, the gas temperature drops sharply in a manner that depends on both the precursor type and the microwave power, as measured by the FTIR following the procedure described in Section 6.4.2. The estimated gas temperature 26 cm downstream of the nozzle for the ethanol case at 1.4 kW power was 560 ± 50 K, further dropping to 450 ± 20 K at a distance of 170–234 cm from the nozzle.

The FTIR measurements were deployed in this work as a line-of-sight diagnostic. Hence, the FTIR-derived temperature corresponds to a path-averaged temperature, and the true temperature may vary considerably along the absorption path. To determine the possible temperature distributions along the absorption paths, spatially resolved thermocouple measurements were carried out at both measurement positions, and the obtained data were corrected for radiative losses as described in Appendix A. Figure 6.2 b shows the radial temperature distribution (470–820 K) in the lower measurement position. An N-type thermocouple (1 mm diameter) was inserted into the reactor and the radial profile was measured by gradually traversing the thermocouple across the reactor. In the upper measurement position (Figure 6.2 c), a K-type thermocouple (1.5 mm diameter) was alternately installed 185 and 215 cm downstream of the nozzle with the thermocouple tip located in the center of the gas flow. These measurements yielded a temperature drop of 20–40 K between the two positions depending on the precursor type and microwave power. Therefore, the gas temperature variation along the absorption path in the upper measurement position (HAN = 170–234 cm) was expected to be within 40–70 K.

6.3 Kinetics simulation of gas-phase products

Numerical simulations were carried out using Ansys Chemkin-Pro 2020 to predict potential gaseous products of the process, identify possible markers indicating FLG or soot particle formation, and compare the results with experimental findings. The reactor was modeled as a one-dimensional plug flow reactor with a constant inner diameter of 7 cm (as the quartz tube), constant pressure of 1 bar (10^5 Pa), and a fixed temperature profile, which is described in Section 6.2. All gaseous species were considered to be at the same temperature. The species concentrations were calculated by kinetically-controlled reactions. Here, the detailed chemical kinetics model from the CRECK modeling group (“TPRF HT + LT + Alcohols”, Version 2003, March 2020, [196]) was used for all precursor cases listed in Table 3.1. Plasma chemistry was excluded from the model. The gas flows used in the experiments were provided as input. Since the length of the high-temperature plasma region (8 cm) was chosen based solely on the length of the resonator and a single point OES measurement, additional numerical simulations were carried out with the reaction zone lengths varied between 2–12 cm to probe different precursor residence times. These simulations revealed no significant differences in the gaseous species concentrations, suggesting that the plasma temperature of 3800 K leads to a complete and almost instantaneous precursor decomposition.

The simulation did not account for solid carbon formation. Hence, the total concentration of carbon-containing gaseous species is overpredicted by the amount of carbon consumed in the solid phase. The overprediction can be estimated by analyzing the solid material yield. The FLG yield of 1.8 wt.% was measured when using 190 sccm of ethanol (Case 1 here) [55]. If adopting that yield to the current study, it corresponds to ~122 ppm of atomic carbon. When using C_2H_4/H_2O mixtures, the solid carbon yields were decreasing from 6.5 wt.% when no water was added (Case 3 here) to 1.5 wt.% for the highest water flowrate (Case 6) [55], which corresponds to atomic carbon concentrations of ~442 and ~102 ppm, respectively. Therefore, for the cases when FLG or FLG and soot particles mixtures were produced, the solid material formation is not considered a significant sink for carbon atoms. In the case of toluene, the yield of soot particles was more significant, up to 36 wt.% [55]. When using 54.3 sccm of toluene (Case 2), such a mass production rate corresponds to ~2448 ppm, if soot particles are assumed to consist only of carbon.

Figure 6.3 shows the evolution of main gaseous species concentrations along the reactor length for all six investigated cases (Table 3.1), each having ~6800 ppm atomic carbon input into the reactor. Five temperature regions with different gas-phase kinetics can be distinguished. First, the precursors are supplied inside the reactor at 453 K. Second, the precursors approach the plasma zone and fully decompose even before the maximum temperature is reached. Within that short time and space, multiple gaseous species are formed. Third, the gases reach the plasma region with the maximum temperature of 3800 K, where all species but stable CO either fully or partially decompose. Fourth, the remaining gases and decomposition products leave the plasma zone, upon which time the temperature decays exponentially with downstream distance, and multiple stable gaseous species are

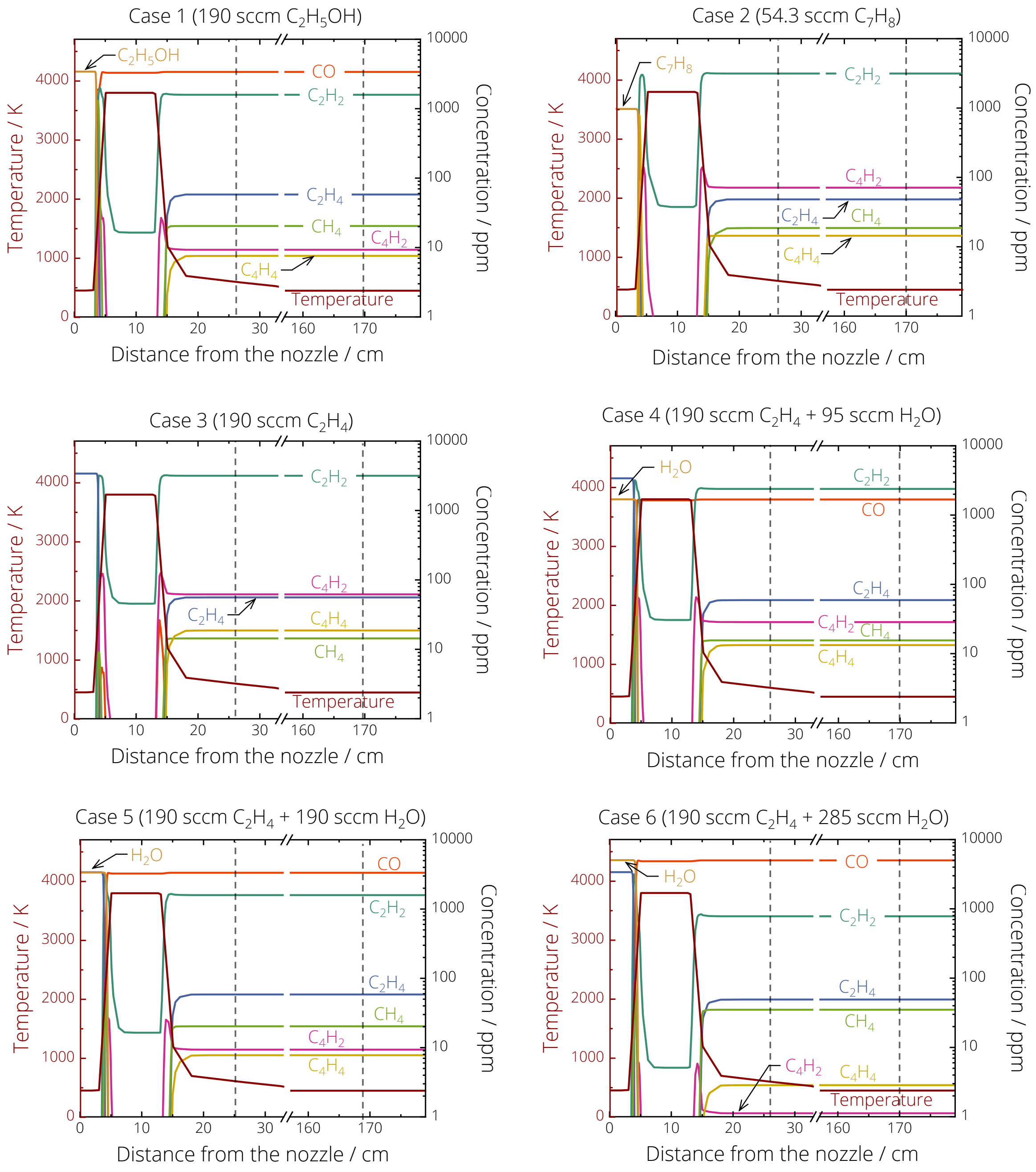

Figure 6.3 Numerical simulations of the reaction progress based on imposed temperature profiles (Figure 6.2 a) showing the evolution of the main gaseous species along the reactor. A universal temperature profile was provided as a simulation input. Dashed vertical lines denote the lower and upper FTIR measurement positions at HAN = 26 and 170 cm downstream of the nozzle, respectively.

formed. The simulations suggest that no intermediate species or radicals are present outside of the reaction zone, as well as no changes in stable species concentrations, suggesting that the gas-phase reactions are confined to the reaction region. The kinetic process of solid carbon growth likely occurs in the colder, fifth temperature region, i.e., the assembly zone, which is located further downstream [63,64], in this case, ~13 cm and further. The FTIR measurements were performed in two positions, both downstream of the reaction zone, as shown in Figure 6.3 with dashed vertical lines.

In cases where oxygen was present in the precursor molecule, e.g., ethanol and C_2H_4/H_2O mixtures, 99–99.5 % of the oxygen atoms were predicted to be consumed to form stable CO molecules. Therefore, other oxygen-containing species, such as H_2O and CO_2, were predicted to be present only at trace amounts.

In total, five stable hydrocarbon species were predicted to be present at sizable concentrations in all investigated cases: C_2H_2, CH_4, C_2H_4, C_4H_2, and C_4H_4. Simulations show that after CO is formed, up to 95 % of the remaining carbon atoms are bound as C_2H_2 molecules. In cases with oxygen-containing precursors, C_2H_2 concentrations were lower than in the case of oxygen-free precursors, as otherwise some of the carbon was oxidized into CO, leaving less available carbon to form other species. Higher concentrations of acetylene led to higher concentrations of diacetylene (C_4H_2) and 1-buten-3-yne (C_4H_4), which are both produced from the dimerization of acetylene. However, the simulations suggested similar concentrations of CH_4 and C_2H_4 for all investigated cases with no apparent dependence on the precursor chemistry. Overall, based solely on predicted evolutions of gaseous by-products, different carbonaceous aerosols could not be classified.

6.4 FTIR measurements

Measured intensities were converted to absorbance, $A_\nu = \ln(I_{\nu,0}/I_\nu)$, where $I_{\nu,0}$ is the incident intensity and I_ν is the transmitted light intensity across the gas. No light emission was detected in background scans and negligible levels of IR light-induced emission are expected at the irradiation levels provided by the FTIR system. The incandescence signal from the hot particles observed in the lower measurement position, after the Fourier transformation, resulted in the noisy spectrum shown in Figure 6.4, with the intensity averaging around zero level. Hence, no corrections for gas or particle emission were applied.

Figure 6.5 shows an FTIR absorbance spectrum obtained in the upper measurement position for Case 1 (190 sccm of ethanol, microwave power: 1.4 kW). At these conditions, pure FLG was produced. However, qualitatively similar spectra were obtained in other investigated cases, including the lower measurement position. No absorption bands attributable to the precursor species were detected, suggesting their full decomposition. Instead,

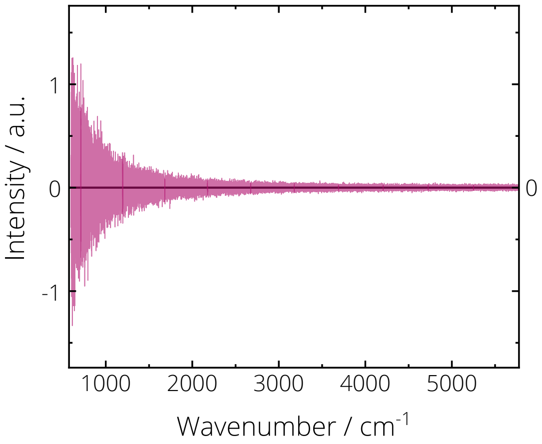

Figure 6.4 Background spectrum obtained from glowing FLG flakes 26 cm downstream of the nozzle. The intensity averages around the zero level with no apparent spectral features. Hence, no correction for the background emission was applied to the measured absorbance spectra.

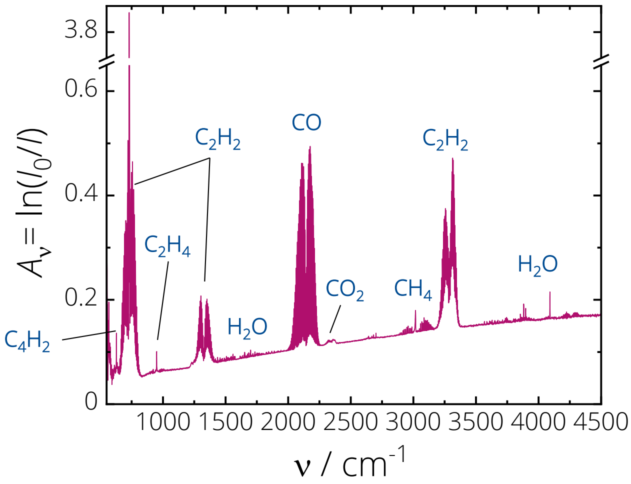

Figure 6.5 FTIR absorbance spectrum for Case 1: 190 sccm of ethanol at 1.4 kW, i.e., FLG synthesis conditions. Multiple gas-phase species are identified. Weak absorbance of H_2O and CO_2 caused by unstable concentrations of these species in the background.

multiple gaseous decomposition products were identified. The most prominent rovibrational bands of acetylene (C_2H_2) were detected at 660–820, 1240–1420, and 3200–3380 cm^{-1}. The absorption band between 2020–2250 cm^{-1} corresponds to CO, while the one between 2850 and 3200 cm^{-1} corresponds to CH_4. The peaks at 628 and 949 cm^{-1} were assigned to C_4H_2 and C_2H_4, respectively. Weak absorbance signals of H_2O and CO_2 were caused by unstable concentrations of these species in the background, which, in some experiments, also resulted in negative absorbance signals. Moreover, a detailed analysis of high-resolution spectra (0.1 cm^{-1}) showed no evidence of H_2O and CO_2 inside the reactor. The list of experimentally detected species matches the one predicted by simulations in Section 6.3 except for C_4H_4 (1-butene-3-yne), which IR bands [197] were not observed in the spectra.

Since measurement positions were located before the particle filter, the resulting spectra should be affected not only by gases, but also solid particles present in the flow. The non-zero baseline of the absorbance curve in Figure 6.5 indicates the presence of solid material with broadband absorption, e.g., FLG. However, no IR bands of intermediate species or initial particle formation blocks, such as poly-aromatic hydrocarbons (PAHs) and dehydrogenated PAHs, were detected., which is consistent with the Chemkin simulations.

To verify the species detected with FTIR, part of the reactor off-gas was directed to a quadrupole mass spectrometer (QMS, Hidden Analytical HALO 301) that classifies species by their mass-to-charge ratio (m/z). The system sampled gas behind the particle filter more than 250 cm downstream of the nozzle; thus, only stable gas-phase species were expected to be detected. The setup schematics and a typical mass spectrum (ethanol 190 sccm, 1.4 kW power) are shown in Figure 6.6. The species identified with QMS matched those found using the FTIR, and neither the FTIR nor the QMS detected C_4H_4. The mass detection range was up to 300 atomic units per single charge; however, no large-mass species, such as PAHs, were observed. In fact, atmospheric pressure microwave plasmas are expected to produce small and simple molecules due to the high number of collisions between electrons and gas molecules resulting in fragmentation [198].

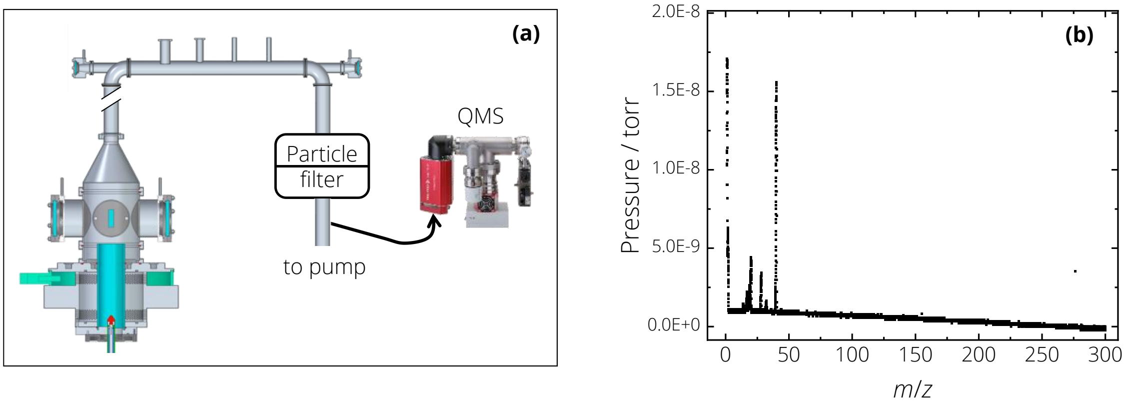

Figure 6.6 (a) Schematics of the quadrupole mass-spectrometry (QMS) measurement setup; (b) Typical mass spectrum for Case 1 (190 sccm ethanol at 1.4 kW power). No species with $m/z > 40$ were detected.

Overall, the gas-phase species detected with FTIR and QMS agreed with those predicted by numerical simulations. The same species were previously reported in the FTIR and mass spectrometry studies on ethanol decomposition in plasmas [56–58].

6.4.1 Quantitative interpretation of absorption spectra

The absorbance spectra were interpreted quantitatively using the HITRAN database [199] and fitting was performed using PGOPHER software [200]. The absorption path in the upper measurement position is known (64 cm) and the gases were considered to be homogeneously mixed based on the non-steady flow conditions, distant location of the measurement position from the gas inlet, and the negligible temperature variation along the absorption path (Figure 6.2 c). Hence, the absolute gas concentrations were calculated and reported here in parts per million (ppm) by assuming the ideal gas behavior. In the lower measurement position, the gas temperature along the absorption path varies between 470–820 K (Figure 6.2 b). Therefore, the gases are present at a range of temperatures, which implies their non-homogeneous distribution. The absorbance of each gas species is then defined as:

$$A_\nu = \ln\frac{I_{\nu,0}}{I_\nu} = \int_0^L \kappa_\nu(s)\,\mathrm{d}s = \int_0^L N(s)\,C_{\mathrm{abs},\nu}\left[T(s)\right]\mathrm{d}s = L\cdot\bar{N}C_{\mathrm{abs},\nu}\left(\bar{T}\right), \tag{6.1}$$

where L is the total absorption path, κ_ν is the spectral absorption coefficient, N is the gas species concentration, $C_{\mathrm{abs},\nu}$ is the absorption cross-section, T is the gas temperature, and $\bar{T}$ and $\bar{N}$ are the effective gas species temperature and concentration assuming homogeneous mixing and thermal equilibrium along the absorption path.

Figure 6.7 shows the measured and simulated absorbance spectra and the fit residual for 190 sccm of ethanol at 1.4 kW (Case 1) in the upper measurement position.

The fit procedure involves several pre-processing steps. Only the main isotopes of each species were considered in the simulations, with abundances of 97.7 % and higher. The 660–820 and 1240–1420 cm^{-1} bands of C_2H_2 were excluded from the fit due to signal saturation and overlap with water absorption bands, respectively. The low-resolution spectra (1 cm^{-1}) yielded inconsistent results when compared with the high-resolution spectra (0.1 cm^{-1}), suggesting inadequate resolution to resolve the line structure of the investigated species. Hence, unless stated otherwise, the high-resolution absorbance spectra were used to provide gas temperatures and species concentrations.

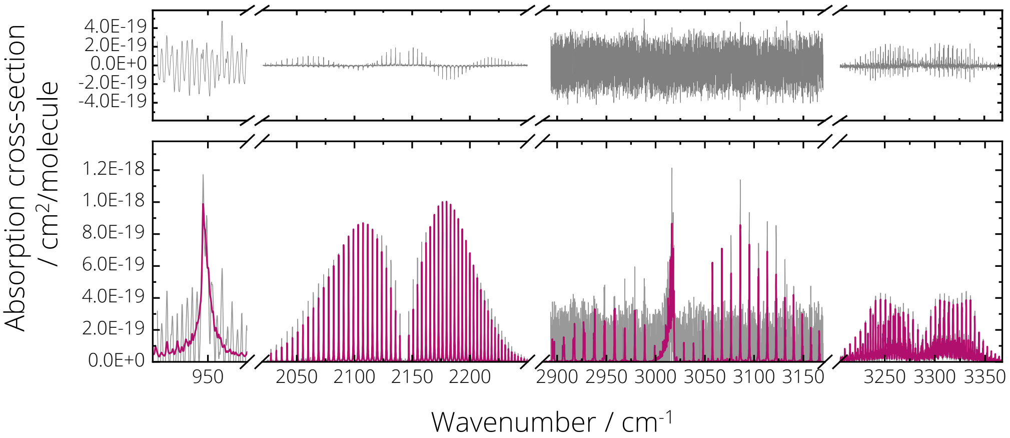

Figure 6.7 Simulated (pink) and measured (grey) absorbance spectra of C_2H_4, CO, CH_4, and C_2H_2. The upper graph shows the respective fit residuals. The spectrum was obtained in the upper measurement position for Case 1: 190 sccm ethanol at 1.4 kW power. The simulation yielded the following species concentrations: C_2H_4: 67 ppm; CO: 2520 ppm; CH_4: 55 ppm; C_2H_2: 1189 ppm; and a temperature of 476 K.

Finally, before feeding the spectra into PGOPHER, the baseline associated with solid phase absorbance (Figure 6.5) was subtracted.

The data were fitted by accounting for line broadening and treating species concentration and mixture temperature as fitting variables. A Lorentzian line shape was used, as pressure broadening is expected to be dominant at atmospheric pressure and relatively low temperatures in the measurement positions. All peaks of each species were simulated with the same line broadening.

To estimate the concentration measurement uncertainty, reference measurements were conducted at room temperature using Ar/CO mixtures with known CO concentrations (Figure 6.8). The CO content varied between 50 and 1000 ppm, and the IR spectra were recorded at 0.1 and 1 cm^{-1} resolution. The true CO concentration error was estimated as ±5 % based on the concentration variation in the gas cylinder (as per supplier) and the calibration of the mass flow controllers used. The resulting concentration uncertainty during the reference measurements

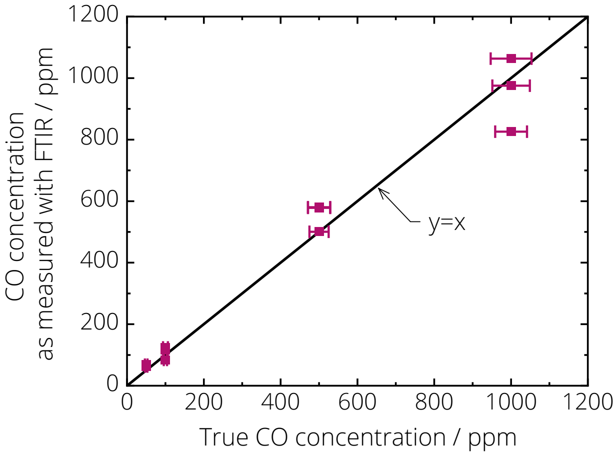

Figure 6.8 Reference concentration measurements conducted using Ar/CO mixtures with known CO concentrations. The true CO concentration error was estimated as ±5 %. The measurement uncertainty of ±20 % was determined.

was estimated to be ±20 %. The concentration measurements are sensitive to the molecular absorption cross-section, and hence, the uncertainty is species- and temperature-dependent. However, for the lack of reference measurements with other gases, the same ±20 % uncertainty was applied to all species. It is difficult to estimate the temperature uncertainty as no reference measurements were done at temperatures other than room temperature, in which case the deviation was found to be less than 2 %.

6.4.2 Temperature measurements

Figure 6.9 shows gas temperatures measured in two positions in the reactor for different precursors versus microwave power. Temperatures were estimated with three approaches. The FTIR absorbance spectra were fitted with temperature as a fitting parameter (Figure 6.9 a–c). The Boltzmann plots were calculated using the 2020–2250 cm^{-1} rovibrational band of CO (Figure 6.9 d), for the calculation details see Appendix B. In the third approach (Figure 6.9 a), a K-type thermocouple was inserted in the center of the gas flow 185 cm downstream of the nozzle.

Figure 6.9 a shows that gas temperatures in the upper measurement position increase with microwave power. This observation applies to both the ethanol and toluene, suggesting that increasing temperatures in the plasma zone elevates the temperature of the gases downstream. Thermocouple measurements at 185 cm HAN were consistently lower than the FTIR-derived ones by 30–50 K, even after correcting for radiative losses (see Appendix A). The discrepancy could be caused by neglecting conductive heat transfer losses along the thermocouple wires [201]

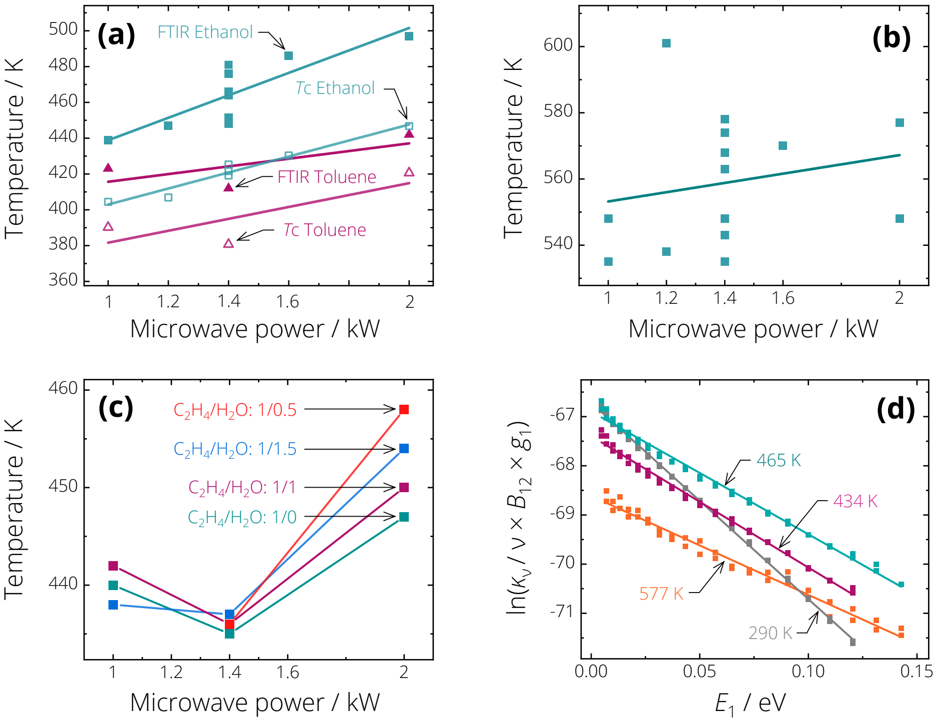

Figure 6.9 Gas temperatures versus microwave power. (a) Case 1 (190 sccm ethanol) and Case 2 (54.3 sccm toluene) in the upper measurement position; (b) Case 1 (190 sccm ethanol) in the lower measurement position; (c) Cases 3-6 (C_2H_4/H_2O mixtures) in the upper measurement position; (d) typical Boltzmann plots calculated for the 2020-2250 cm^{-1} rovibrational band of CO. E_1: lower state energy; κ_ν: integrated spectral absorption coefficient; ν: wavenumber; B_{12}: Einstein coefficient; g_1: lower-state statistical weight.

and the temperature variation along the tube, which was estimated to be less than 70 K, as determined in Section 6.2. Additional calculations confirmed that the 70 K temperature deviation has an insignificant effect on species concentrations compared to the experimental uncertainty. It can also be seen that gas temperatures were higher when ethanol was used as a precursor compared to toluene. This is attributed to the large differences in radiative heat losses, i.e., different particulate volume fractions produced in the ethanol and toluene cases, which is implied by mass rate productions of FLG (0.2–0.4 g/h) and soot (2 g/h).

Figure 6.9 b shows gas temperatures versus microwave power at the lower measurement position, where the unsteady flow environment resulted in a large scatter of derived temperatures. However, linear regression reveals a slight temperature increase with increasing microwave power as one may expect [59]. Figure 6.9 c shows gas temperatures increasing with microwave power for Cases 3–6, C_2H_4/H_2O mixtures with different ratios of H_2O. Adding water to the reactants did not affect the gas temperature, which is consistent with the prior work [55].

Figure 6.9 d shows CO Boltzmann plots calculated for some typical measurements: room temperature validation (290 K), Case 1 upper position at 1.4 kW (465 K), Case 5 upper position at 1.4 kW (434 K), and Case 1 lower position at 1.2 kW (577 K). The CO temperatures were in excellent agreement with the FTIR-derived ones, obtained by fitting the multiple species spectra simultaneously (Figure 6.9 a–c). Overall, the FTIR absorbance spectra yielded reliable temperatures as confirmed by thermocouple measurements.

6.4.3 Gas-phase species concentrations as a function of the precursor flow rate

Figure 6.10 shows the changes in gas temperature and species concentrations in the upper measurement position versus the ethanol flow rate (Case 1). All experiments were done at a microwave power of 1.4 kW. The shaded areas denote the experimental concentration uncertainty of ±20 % determined from reference measurements as described in Section 6.4.1.

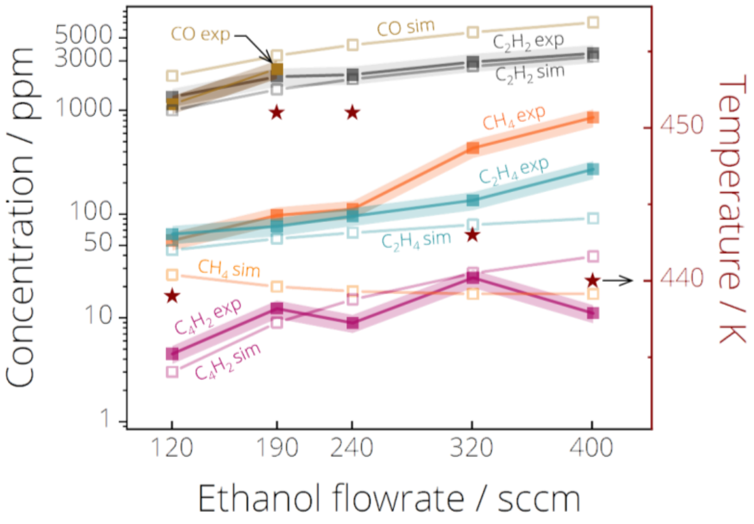

Figure 6.10 Species concentrations and gas temperature versus the ethanol flow rate (Case 1). All experiments were done at 1.4 kW microwave power. Solid symbols: FTIR measurements; shaded areas: experimental uncertainty; open symbols: numerical simulations. The gas temperature (dark red stars) shows no significant dependence on the ethanol flow rate.

No ethanol was detected or predicted, even at the highest ethanol flow rate, indicating its complete decomposition. Consequently, as the amount of ethanol supplied to the reactor increases, there is a corresponding increase in ethanol decomposition products measured with FTIR. The gas temperature of 440–450 K, on the other hand, was found to be independent of the ethanol flow rate. This is expected since the enthalpy of the products is dominated by the sensible energy of the inert co-flow gases of Ar and N_2, which contribute to > 99 % of the mass of the gas flow. Toman et al. [56] reported similar observations, although operating the reactor at smaller microwave powers and smaller precursor flows. The CO absorption signal was saturated at ethanol flow rates higher than 190 sccm (> 3000 ppm), which resulted in a poor fit, so these data were excluded from further quantitative analysis. No CO_2 or H_2O were detected or predicted in sizeable quantities at any investigated conditions.

The measured product species concentrations were compared with the simulations (Figure 6.10, open symbols). Similar to the experimental data, the simulations predicted a linear increase in concentrations of CO, C_2H_2, C_2H_4, and C_4H_2 with increasing ethanol flow rate. However, the CH_4 concentration was predicted to decrease with the ethanol flow rate, while the opposite trend was observed in the measurements.

6.4.4 Gas-phase species concentrations from experiments with ethanol and toluene as a function of microwave power

The absorbance in the lower measurement position was calculated as per Equation (6.1), $A_{\nu,\text{lower position}} = L \times [\bar{N} \times C_{\text{abs},\nu}(\bar{T})]$, assuming a constant effective temperature along the absorption path. Simulations and the FTIR measurements suggest that the gas-phase reactions are confined in the region upstream of the lower measurement position, i.e., lower than HAN = 26 cm. Therefore, the gas species concentrations in the lower and upper positions were expected to be equal. When considering the homogeneous species distribution along the absorption path at the lower position, $L = 15.3$ cm, the species concentrations between the lower and upper measurement positions differ by less than 15 %, which is smaller than the experimental uncertainty. Hence, the assumption of homogeneous mixing is justified even when acknowledging some temperature variation along the absorption path.

Figure 6.11 shows measured and simulated species concentrations at the upper measurement position versus microwave power for Case 1 (190 sccm ethanol, FLG synthesis) and Case 2 (54.3 sccm toluene, soot particle synthesis). Figure 6.12 shows concentrations at the lower position for Case 1. The shaded areas denote the experimental uncertainty. Since the measurements in the lower position were conducted in a noisy environment of a flickering plasma afterglow, only three species had absorbance signal-to-noise ratios large enough for concentrations to be quantified. Measured concentrations were compared with the numerical simulation performed for the 1.4 kW power experiment (Figure 6.3).

Figure 6.11 a and Figure 6.12 a show that CO concentrations increase with microwave power at both measurement positions. This suggests that with increasing power, more oxygen from oxygen-containing reactants (C_2H_5OH, H_2O) is consumed to form CO, thus leaving fewer carbon atoms to form solid carbonaceous particles and less free oxygen that could potentially bind to the particles. Assuming that every oxygen atom attached to the ethanol molecule is converted to CO, one would expect a CO concentration of 3415 ppm. The numerical simulation predicts 99.1 % of oxygen atoms convert to CO molecules, resulting in 3384 ppm of CO, which is in good agreement with the measured CO concentration. Figure 6.12 a, however, shows that some of the measurements showed CO concentrations higher than that, which is the result of the experimental uncertainty of ±20 %. The possibility of the reactor leak is ruled out since in that case the CO concentrations in the upper measurement position would be

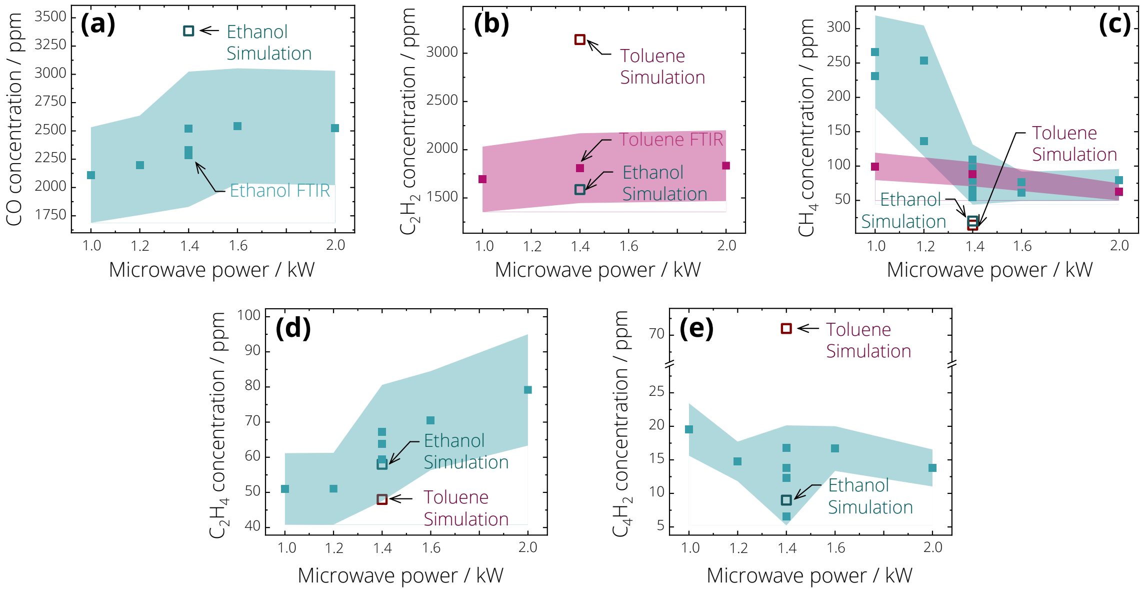

Figure 6.11 Measured and simulated species concentrations in the upper position (170–234 cm downstream of the nozzle) versus microwave power for Case 1 (190 sccm ethanol, blue color data) and Case 2 (54.3 sccm toluene, pink color data). (a) CO; (b) C_2H_2; (c) CH_4; (d) C_2H_4; (e) C_4H_2. Shaded areas denote the experimental uncertainty. Simulations were performed using the temperature profile corresponding to 1.4 kW power.

affected as well, which is not the case (Figure 6.11 a). Still, the trend of CO concentrations increasing with microwave power is clear in both measurement positions.

Figure 6.11 b and Figure 6.12 b show how the C_2H_2 concentrations vary with microwave power. For ethanol in the upper measurement position, the experimental data showed a dependence on the time the measurements were taken and hence was excluded from the analysis as not reliable. In the lower position, C_2H_2 concentrations increased with power. The simulated acetylene concentration agrees well with the measurements. In the case of toluene, C_2H_2 concentrations also increase with increasing power, while the simulated concentration expectedly overestimates the experimental data due to the non-accounted effect of solid particles formation, as discussed in Section 6.3.

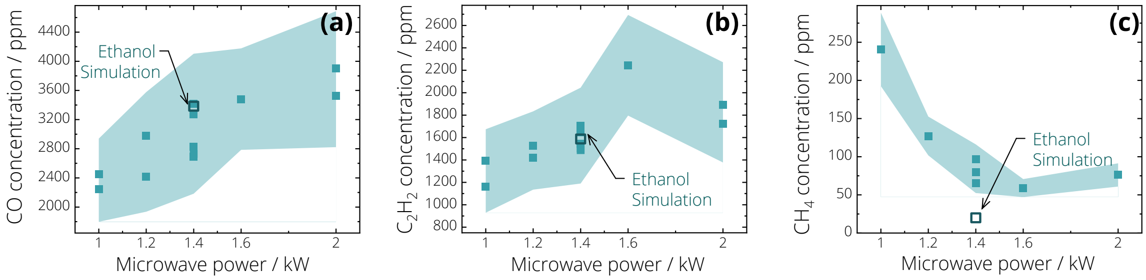

Figure 6.12 Measured and simulated species concentrations in the lower position (26 cm downstream of the nozzle) versus microwave power for Case 1 (190 sccm ethanol). (a) CO; (b) C_2H_2; (c) CH_4. Shaded areas denote the experimental uncertainty. Simulations were performed using the temperature profile corresponding to 1.4 kW power.

CH_4 concentrations decrease with increasing microwave power in both measurement positions for both ethanol and toluene precursors (Figure 6.11 c and Figure 6.12 c). The numerical simulations also predict concentrations that are consistent with the experimental data. Jiménez et al. [198] investigated gaseous products of ethanol plasma decomposition and found that methane and acetylene concentrations are inversely related. Hence, when CH_4 concentrations decrease, an increase in C_2H_2 concentrations is expected. This agrees with the observations presented here.

Overall, as predicted by the simulations, the trends and absolute concentrations of CO, C_2H_2, and CH_4 agree between the two measurement positions, which implies that the gas-phase reactions are constrained in the high-temperature plasma region upstream in the reactor.

Figure 6.11 d,e shows that C_2H_4 concentrations rise with microwave power while C_4H_2 concentrations are insensitive to microwave power. Based on the simulations, both species are expected to follow the trend of C_2H_2 increasing with microwave power. In the case of C_4H_2, the concentrations could only be quantified using low-resolution absorbance spectra (1 cm^{-1}) due to a better signal-to-noise ratio, and hence no firm conclusions should be drawn since low-resolution data were shown to yield inconsistent results (Section 6.4.1). In the case of toluene, no low-resolution spectra were recorded, which explains why neither C_2H_4 nor C_4H_2 were detected, even though the simulations predicted the formation of these species.

In general, the FTIR results do not provide a clear way to distinguish between the formation of soot particles and FLG flakes *in situ*. The same conclusion was made based on the numerical simulations. Correlations between microwave power, species concentrations, and particle morphology are addressed in Section 6.5.

6.4.5 Gas-phase species concentrations from experiments with C_2H_4/H_2O as a function of the microwave power

Figure 6.13 shows measured and simulated species concentrations in the upper measurement position versus microwave power for Cases 3–6 (C_2H_4/H_2O mixtures). Measurements were performed at 1.0, 1.4, and 2.0 kW powers. Shaded areas denote the experimental uncertainty.

The concentration trends were similar to the ones observed in the experiments with ethanol (Case 1): CO and C_2H_2 concentrations increase with microwave power, while CH_4 concentrations decrease. As established in the previous section, this could be indicative of the reaction shift toward graphene formation. Another observation is that as more H_2O is supplied into the system, the higher CO concentrations were measured. Unlike in the experiments with ethanol, here, not all oxygen atoms were consumed in CO formation. Independent of the H_2O content, the measured CO concentrations account for approximately half of the oxygen atoms present in the system. It is currently not understood, what oxygenates are formed from the atomic oxygen that remains in the system. Neither H_2O nor CO_2 were detected with FTIR or QMS, and no O_2 was detected with QMS. Furthermore, x-ray photoelectron spectroscopy did not reveal increasing graphene oxygenation with water addition [55]. Further experimental studies are necessary to track down the oxygen species, for example, using high sensitivity gas chromatography–mass spectrometry [56]. The numerical simulations, however, predicted that almost all the available oxygen atoms form CO molecules, hence overpredicting CO concentrations by a factor of ~2. That resulted in other species concentrations being significantly underpredicted, except for Case 3, where no oxygen was present in the system ($C_2H_4/H_2O = 1/0$) and numerical results were relatively close to the FTIR-measured values. The discrepan-

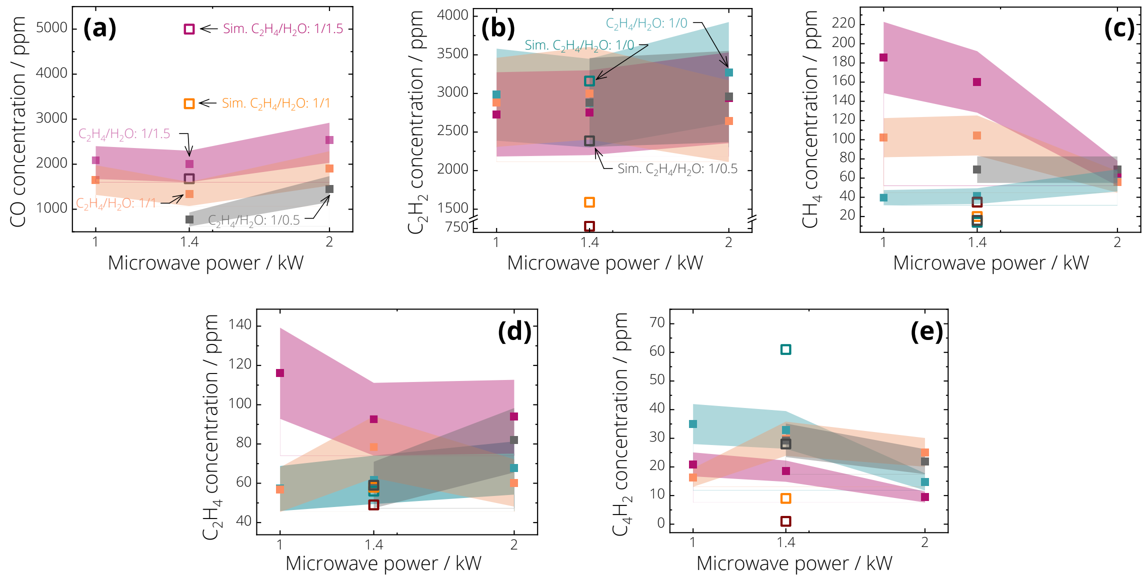

Figure 6.13 Measured and simulated species concentrations in the upper position (170 cm downstream of the nozzle) versus microwave power for Cases 3–6 (C_2H_4/H_2O mixtures). Shaded areas denote the measurement uncertainty. Simulations were performed using the temperature profile corresponding to 1.4 kW power.

cies between the numerical simulations and the experiments highlight the complexity of the precursor's decomposition in a plasma environment, which, in certain cases, e.g., for C_2H_4/H_2O mixtures, cannot be approximated as high-temperature pyrolysis.

6.5 Discussion

Measurements and simulations show that the hydrocarbon precursors supplied into the system are completely dissociated by the plasma, which results in approximately ~6800 ppm of carbon atoms within the reaction zone. That carbon either forms flakes and particles or carbon-containing gaseous species. For example, in the case of ethanol at 1 kW power, a mixture of FLG and soot particles was produced. Figure 6.12 shows that under these conditions, due to low concentrations of CO and C_2H_2, a low amount of carbon was consumed in the formation of gaseous species, hence, a high amount of carbon remained in the system available for the solid-phase formation. On the other hand, at microwave powers of 1.4 kW and higher, pure FLG flakes without soot particles were synthesized. At these conditions, high concentrations of CO and C_2H_2 were measured, leaving less carbon for the solid carbon growth.

Figure 6.14 shows the concentrations of carbon available for the solid-phase growth after carbon-containing gaseous species were formed versus microwave power. The shaded areas denote ranges of experimental uncertainty (±20 %). In all cases, similar carbon concentrations were initially delivered to the system as carbon-containing precursors, ~6800 ppm.

Several correlations with particle morphology can be seen. In Case 2, in which toluene is the feedstock, only soot particles were observed, with no FLG flakes, regardless of the microwave power; this case is also the one with the largest concentration of carbon available for solid particulate growth. In Case 1, in which 190 sccm of ethanol

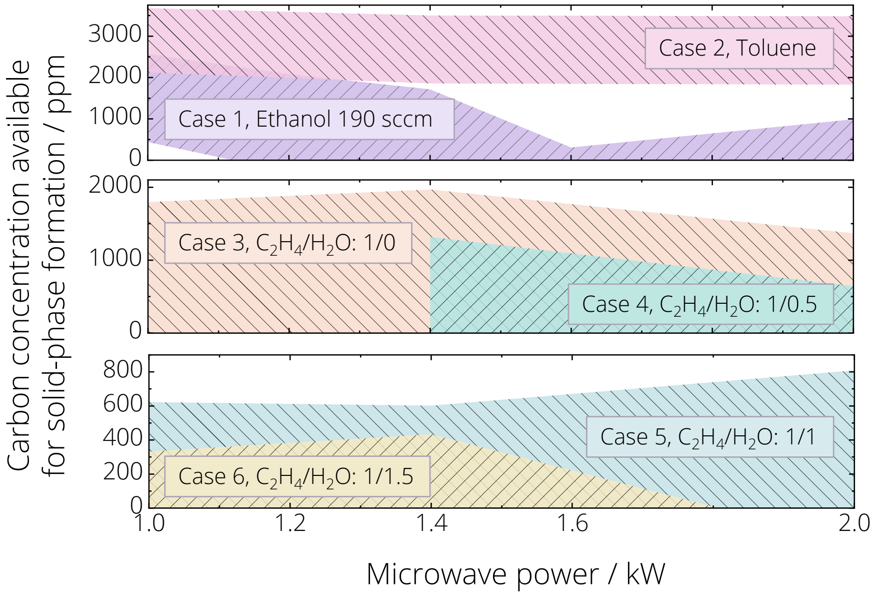

Figure 6.14 Carbon concentrations available in the system for solid-phase formation, i.e., the total amount of carbon delivered into the system minus carbon contained within gaseous species, versus microwave power. Zero values are the result of the measurement uncertainty.

is supplied to the reactor, an FLG/soot particles mixture was realized using 1 kW microwave power, and pure FLG was produced at 1.4 kW and higher. That aligns with the overall decrease in carbon concentration vs. microwave power. The same trend can be observed for Cases 3–6 with C_2H_4/H_2O mixtures, although to a lesser extent and shifted toward higher microwave powers, i.e., available carbon concentrations do not change significantly from 1 to 1.4 kW and only start to decrease after 1.4 kW power.

Figure 6.14 also visualizes the effect of water addition. Adding water to ethylene decreases solid carbon yield while shifting the reaction toward FLG formation: From C_2H_4/H_2O: 1/0 with 6.5 wt.% yield of mostly soot particles to C_2H_4/H_2O: 1/1.5 with as little as 1.5 wt.% pure FLG production [55]. It was hypothesized that larger fractions of water result in higher concentrations of elemental oxygen leading to the formation of CO, thereby reducing the amount of carbon available to form particulate matter, and hence favoring formation of graphene over amorphous 3D structures. This hypothesis was further strengthened by the observation that methanol, a precursor with a ratio of C:O = 1, yielded no solid material, as all carbon was consumed in CO formation [55,61]. The experimental quantitative data presented here suggests that not only the formation of CO molecules reduces the available carbon in the system, but the formation of other carbon-containing gaseous species as well, e.g., hydrocarbons. That could explain why adding H2 to the reactant mixture reduces the solid carbon yield and shifts the process towards graphene formation [67,202]. Indeed, the off-gas FTIR study by Toman et al. [56] showed an increase in gaseous hydrocarbons concentrations when adding H_2 and the same effect was predicted by a model of Tsyganov et al. [63].

The abundance of free carbon in the reaction zone correlates directly with the types of particulate matter that may form. Large concentrations of carbon enable a higher density of nucleation centers that collide and bond with each other and hence form 3D non-structured shapes, which eventually bend to spheres to minimize the free surface energy [203]. Low amounts of carbon, on the other hand, result in a lower density of nucleation centers that consequently favors the growth of planar structures through gradual carbon atoms and molecules addition rather than collisions with other nucleation centers. This is supported by the recent work of Fortugno et al. [55] as well as the findings of Bundaleska et al. [195], which concluded on lower fractions of carbon shifting the solid-phase formation from spherical soot particles toward graphene.

However, the abundance of carbon nucleation centers does not fully define the particle morphology, i.e., there is no strict carbon concentration threshold, by exceeding which spherical particles start to form. For example, Figure 6.14 shows that in Case 5 (C_2H_4/H_2O = 1:1), the carbon concentration available for solid phase formation was similar to or lower than that in Case 1 (C_2H_5OH; pure FLG), but some soot particles were nevertheless formed. The atomic C:O:H ratio in the precursor, largely discussed in the literature as one of the main factors defining the particle morphology [55,60,61], also cannot explicitly explain the product differences between Cases 1 and 5, where this ratio was equal, C:O:H = 2:1:6.

Several studies emphasized the importance of H-atoms in carbon particulate production in plasma environments [204–206]. The H2 addition to the precursor mixture was found to strongly suppress the formation of soot particles but also inhibit the total solid carbon yield [56,63,206]. Hence, it was assumed that the H-atoms terminate the dangling carbon bonds at the edges of the growing graphene sheets, effectively preventing their further planar growth (inhibiting yield) but also curling (suppressing the formation of soot particles).

Table 6.1 shows the initial H-concentrations supplied to the reactor in precursors, H-atoms consumed in hydrocarbons formation (as measured with FTIR), and the remaining H-concentration in the post-plasma region. A clear correlation between the particle morphology and the H-abundancy in the post-plasma zone can be seen. The lowest H-concentration in Case 2 (toluene) combined with the highest C-concentrations (Figure 6.14) resulted in pure soot particle formation. Pure FLG was produced only in Cases 1 and 6, where the highest H-concentrations and the lowest C-concentrations were calculated. The H-atoms supposedly only terminate free bonds at the graphene edges, hence, no significant H-content is expected in the produced powder, which was confirmed with the x-ray photoelectron spectroscopy analysis [55].

Therefore, it should be emphasized that it is not the precursor's C:O:H ratio or the carbon nuclei abundance that defines the particle morphology but rather the atomic C:H ratio in the post-plasma zone. Unfortunately, due to the large FTIR measurements uncertainty (± 20%), this study cannot firmly define the C:H ratio in the post-

Table 6.1 H-atom concentrations supplied to reactor in precursor, consumed in hydrocarbons formation (as measured with FTIR), and remaining in the post-plasma region.

Case	Precursor	Flow rate / sccm	H-concentration in precursor / ppm	H-concentration consumed in hydrocarbons / ppm	Remaining H-concentration / ppm
1	Ethanol	190	20400	2800–4900	15500–17600
2	Toluene	54.3	7800	3200–4800	3000–4600
3	Ethylene	190	13600	5000–7500	6100–8600
4	Ethylene	190	17000	5000–7600	9400–12000
5	Ethylene	190	20400	5400–8100	12300–15000
6	Ethylene	190	23800	5200–7800	16000–18600

plasma region. *In situ* gas species measurements with reduced uncertainty would allow establishing the "goldilocks" C:H ratio for pure graphene production. Alternatively, comprehensive kinetics studies of precursors decomposition at high temperatures in a plasma environment are necessary to understand the formation of gas species and to predict the final C:H ratio in the post-plasma region.

The effect of microwave power (i.e., gas temperature) on the kinetics of ethanol decomposition in plasmas was investigated by Toman et al. [56]. Using FTIR and time-of-flight mass spectrometry the authors showed that when increasing the microwave power, the concentrations of hydrocarbons with an odd number of carbon atoms ($C_{2n+1}H_x$) are suppressed several times more than that of hydrocarbons with an even number of carbon atoms ($C_{2n}H_x$). Since they also observed the reaction shift toward graphene formation with increasing microwave power, Toman et al. concluded that $C_{2n}H_x$ species are important for graphene growth while $C_{2n+1}H_x$ species are probably responsible for graphene defects, such as 5- and 7-member rings. In this work, the decrease of $C_{2n+1}H_x$ species (CH_4) was also correlated with the reaction shift toward graphene formation, while concentrations of $C_{2n}H_x$ species (C_2H_2, C_2H_4) that are supposedly responsible for graphene growth were shown to increase with microwave power.

6.6 Conclusions and future work

Gas-phase microwave plasma synthesis of freestanding graphene is yet to be improved in production rate and yield. One of the main obstacles to progress is a lack of comprehensive understanding of gas-phase kinetics. Although experimentalists have invested significant efforts into process investigation, for the most part, these works were focused on parametric studies and *ex situ* characterization.

This chapter presented the use of gas-phase FTIR spectroscopy as a tool to investigate the gas-phase formation of graphene *in situ*. Multiple gaseous by-products were detected, and their concentrations were measured in the post-plasma and exhaust regions. The results were compared with chemical kinetics simulations and mass spectrometry measurements to yield a detailed picture of the gas-phase species involved in graphene synthesis. The FTIR measurements enabled the calculation of the elemental carbon concentrations in the post-plasma region available for solid-phase formation. It was quantitatively proven that lower carbon and higher hydrogen concentrations (lower C:H ratio) shift the reaction toward the formation of graphene flakes rather than amorphous soot particles. That was previously assumed based on qualitative *ex situ* analysis with transmission electron microscopy and Raman spectroscopy, as described in Chapter 3. Ways to reduce and control the C:H ratio in the post-plasma region were investigated, specifically by using lower precursor flow rates, higher microwave powers, and oxygen/hydrogen-containing precursors or additives.

The natural progression of this work would include experiments conducted closer to the plasma zone with the goal of detecting gaseous intermediate species and initial graphene formation blocks, e.g., dehydrogenated polyaromatic hydrocarbons. This would require a specific design of the reactor to allow optical access to the plasma zone. Moreover, the measurement sensitivity should be improved, which could be achieved by minimization of the signal's uncertainty, i.e., stabilizing the particle torch, and increasing the absorption pathlength, e.g., implementing multiple-path by using highly reflective mirrors.

Chapter 7
Conclusions

The goal of this thesis was to investigate *in situ* the gas-phase microwave-plasma synthesis of graphene. The gas-phase approach was chosen because of its scalability, high variability, and ability to produce high-quality graphene in a continuous manner. However, the physical and chemical processes underlying the synthesis, e.g., the kinetics of graphene formation and growth and evolution of flakes morphology in the aerosol phase, are currently little understood. Knowledge of these processes is vital to learn how to control the synthesis, increase yield, and ultimately develop industrial-scale processes. Accordingly, there is a need for *in situ* diagnostics that can probe graphene formation kinetics and its morphology dynamics, as well as monitor the quality of graphene flakes during production.

In this work, two *in situ* optical diagnostics were applied to gas-phase synthesized graphene for the first time. Time-resolved laser-induced incandescence (TiRe-LII) was used to probe the formation, growth, and evolution of flakes morphology by measuring graphene volume fraction and specific surface area (SSA). Line-of-sight Fourier-transform infrared (FTIR) absorption was used to investigate the gas-phase kinetics by identifying and quantifying gaseous species involved in the synthesis. In the context of this work, the parametric study was carried out and various graphene materials were produced under a number of synthesis conditions. The synthesis process and the obtained materials were extensively characterized using the aforementioned *in situ* diagnostics, inline aerosol measurement tools, and *ex situ* powder characterization.

The *ex situ* study combined with *in situ* line-of-sight FTIR measurements revealed that the product morphology strongly correlates with the elemental carbon and hydrogen concentrations (C:H ratio) in the post-plasma region of the reactor. Excessive carbon and low hydrogen concentrations led to the formation of spherical soot particles while lower carbon and higher hydrogen concentrations were shown to suppress particle formation and shift the reaction towards graphene structures. Several ways to reduce and control the C:H ratio in the reactor were found, specifically by using lower precursor flow rates (lower precursor concentration), higher microwave power, and oxygen/hydrogen-containing precursors or additives. The latter, as shown with FTIR measurements and chemical kinetics simulations, increases elemental hydrogen concentration in the post-plasma region and leads to formation of gaseous species with carbon bonded to oxygen (CO) or hydrogen (C_2H_2, CH_4, C_2H_4, C_4H_2), which effectively reduces the concentration of elemental carbon in the reactor. The increasing amount of applied microwave power was also shown to increase concentrations of carbon-containing gases, hence, lowering the concentration of elemental carbon in the system. Under appropriate process conditions, chemically pure crumpled FLG flakes were obtained, as proven with electron microscopy, Raman spectroscopy, and x-ray photoelectron spectroscopy.

Before applying TiRe-LII to crumpled graphene aerosols, the complex morphology and optical properties of the flakes must be characterized. Moreover, in the case of graphene materials, properties and potential health threats are correlated with the flake morphology, which is not well-characterized in the case of crumpled FLG. A suite of inline aerosol diagnostics was applied to measure crumpled flake lateral size, aspect ratio, mobility and aerodynamic diameter distributions. Regarding the optical properties, it was demonstrated that crumpled FLG flakes have larger spectral mass absorption cross-sections between 370–950 nm than soot, i.e., crumpled FLG absorbs visible light more strongly than soot. The origin of that phenomenon is yet to be understood. One possibility is the presence of organic impurities in the aerosol, although great care was taken to dry and purify the aerosol before the measurements.

It was proven that the optical properties and flake morphology are connected. Using the established metrics on exfoliated graphene flakes, UV-Vis spectra of graphene suspension in ethanol were correlated with the mean graphene layer number and mean lateral size, which showed a close agreement with the electron microscopy analysis. Furthermore, the crumpled FLG flakes were tomographically-reconstructed to investigate how complex morphology affects graphene optical properties. For that, discrete dipole approximation (DDA) simulations were carried out. It was shown that the flake orientation has no impact on the normalized absorption efficiency, and the simple Rayleigh–Debye–Gans theory yields spectral cross-sections that are in close agreement with thorough DDA calculations. These measurements and observations allowed for building the spectroscopic model required for the TiRe-LII analysis.

The crumpled FLG aerosol was shown to absorb laser light at 1064 nm and incandesce, hence, enabling the TiRe-LII. The comparison of TiRe-LII responses between crumpled FLG flakes and soot particles suggested that FLG flakes have a larger absorption function at 1064 nm and larger SSA, which aligns with the other diagnostics applied in this thesis. Different TiRe-LII responses between FLG and soot can be utilized to differentiate the two aerosols online and assess the quality of the produced aerosol. TiRe-LII was also used to measure FLG volume fraction and SSA *in situ*, demonstrating that the method can probe flake formation, growth, and morphology. When combined with thermophoretic TEM sampling, TiRe-LII results showed that the gas-phase formation of graphene starts with a flat sheet consisting of a few graphene layers, which then folds and crumples in the gas phase to form a mechanically-stable crumpled FLG flake.

In conclusion, this work investigated the gas-phase microwave-plasma synthesis of graphene using two *in situ* optical diagnostics: TiRe-LII and line-of-sight FTIR absorption. The obtained data elucidated processes underlying gas-phase graphene formation, revealed factors affecting the product morphology, and helped find and explain the ways to control the synthesis. The results of this study and the developed *in situ* diagnostics enable further research, which is discussed in the next chapter.

Chapter 8
Ongoing and future work

This chapter reviews the questions raised by the results obtained in this work and outlines several ongoing and promising research directions including those enabled by the developed here laser-optical *in situ* diagnostics.

Arguably the largest knowledge gap not covered in this thesis is the plasma physics involved in the gas-phase microwave-assisted synthesis of graphene. Except for the optical emission spectroscopy (OES), all *in situ* optical measurements were conducted in the post-plasma zone. In part, plasma diagnostics was outside of the scope of this thesis, and in part, its avoidance was caused by the reactor's design limitation. Future research should seek to include the plasma species and effects in the process investigation. The work in that direction can start with relatively straightforward experiments, such as measurements of electron concentrations and temperatures (e.g., OES, electrostatic probes), measurements of spatial and temporal distributions of key plasma species including ions and neutrals (e.g., laser-induced fluorescence, FTIR) [207].

The comprehensive dataset on the physicochemical and optical properties of crumpled graphene presented in Chapters 3 and 4 has several outcomes that are beyond the ones already discussed here. First, the aerosol properties may be used in toxicological and atmospheric studies to predict the potential adverse health effects of crumpled graphene and its environmental impact. Second, the morphology data of crumpled graphene powders and aerosols would also be useful when establishing new standards and safety regulations.

Chapters 3 and 4 involve either graphene sampling using TEM grids or nebulization, i.e., wet aerosolization, which might introduce impurities and morphology changes, e.g., extra crumpling, as shown in Figure 4.3. Hence, further morphological and optical characterization of crumpled FLG suspensions and freshly produced aerosols without sampling or nebulization is required, e.g., using developed here laser-optical diagnostics. Such studies would elucidate how graphene morphology and chemical composition change when interacting with solvents or when collected on the TEM grid surface.

The research presented in Chapter 5 explores how the specific surface area of graphene changes with height above the nozzle (HAN) by analyzing the incandescence signals from the flakes. Chapter 6 shows how gaseous species evolve in the reactor using line-of-sight FTIR absorption spectroscopy. However, both studies suffer from the current reactor design that does not allow optical access to the plasma zone, with the lowest achievable HAN $\approx$ 174 mm. The modified design would enable probing flakes and gaseous species that are much closer to the nozzle. In terms of the flake morphology, this is especially promising, as the thermophoretic TEM sampling (Figure 5.16) showed that graphene flakes are likely to originate from flat sheets that start folding and crumpling at relatively low HAN $\approx$ 120–150 mm [190]. But thermophoretic sampling has several drawbacks, including the lack of SSA quantification, low spatial resolution, and required flakes deposition on a TEM grid, which leaves a chance of flakes morphology change when sampled on a grid's surface. The TiRe-LII measurements could, in turn, quantify the SSA and provide high spatial resolution measurements with no sampling involved. Such measurements have the potential to be the first-ever TiRe-LII experiments carried out on truly flat nanoobjects. In terms of gaseous species, line-of-sight FTIR measurements in the proximity of the plasma zone may detect what this study aimed to: intermediate species and initial graphene formation blocks, such as dehydrogenated polyaromatic hydrocarbons. When available, that information would advance the current understanding of graphene gas-phase kinetics and ultimately allow for better synthesis control. Moreover, *in situ* data on carbonaceous precursors pyrolysis are useful for validating and updating the existing kinetics models.

Limited FTIR setup sensitivity (Chapter 6) and unsteady gas flow conditions translated into the measurement error of ± 20 % for all species concentrations. This complicated calculating the "goldilocks" C:H ratio in the post-plasma zone that would lead to the formation of pure graphene. The measurement sensitivity could be improved in the future by stabilizing the particle torch and increasing the light absorption pathlength, e.g., by implementing multiple-path absorption when using highly reflective mirrors. If the critical role of hydrogen in the graphene synthesis is confirmed, in the industrial setting, H_2 could be filtered out from the exhaust gases and reused in the process and/or stored as an energy source, thus, substantially reducing the graphene synthesis cost.

Regarding the LII, the ongoing study seeks to measure the evolution of FLG volume fraction with HAN. Identifying a zone where graphene starts to form (detection of LII signals), grows in volume (increasing LII magnitudes), and reaches its final volume fraction (maximum LII magnitude), would allow for a better understanding of the process. For example, if the correlation between reactor geometry, temperature profile, and the graphene volume fraction is defined, the corresponding parameters could be tuned to achieve a higher yield.

TiRe-LII is also currently being applied to graphene aerosols to detect any non-incandescent emissions, analogous to the soot studies in flames [176,177,189]. Although some test measurements have been carried out (Section 5.2.1), they were limited to the excitation wavelength of 1064 nm, laser fluences up to ~5 mJ/mm^2, and HAN above 200 mm. When using 532/266 nm laser wavelengths, higher fluences, or lower HAN, additional emission features could appear. Of particular interest is the detection of laser-induced fluorescence from polyaromatic hydrocarbons present in the flow, induced emission of C_2^* and C_3^* clusters evaporated from graphene surface, and detection of co-present LII signals if the evaporated carbon clusters condense back and form new particles/flakes [208]. Apart from the fundamental value of such measurements, the obtained data will be important for practitioners to avoid potential temporal and spectral interferences when deploying TiRe-LII to graphene.

Besides the additional TiRe-LII experiments, laser-induced breakdown spectroscopy (LIBS) could be used to examine the FLG chemical composition and evaporation parameters, and to narrow down the uncertainties through the Bayesian data inference with the TiRe-LII results incorporated, as previously demonstrated by Menser et al. for Si and Ge nanoparticles [152,209]. LIBS involves a high-power laser pulse, which vaporizes and ionizes the sample. The resulting plasma emission comes from electronically-excited ions, atoms, and molecules, and can be correlated with the particle chemical composition and concentrations of the species present in the sample.

LIBS, TiRe-LII, and FTIR can be combined to characterize graphene doping and functionalization efficiency. FTIR can identify gas-phase intermediate and stable species and correlate them with flake morphology measured with TiRe-LII. And LIBS can detect and quantify the doping species that are present in graphene structure. This information may potentially indicate ways to improve the quality of existing functionalized graphene materials and create new ones, leading to novel applications.

Several unresolved questions arose throughout this study. Chapter 4 and Chapter 5 showed that crumpled FLG flakes have larger MAC$_\lambda$ values between 370–950 nm and higher $E(\mathbf{m})$ at 1064 nm compared to those of soot particles. So far it is unclear, which mechanism is responsible for the enhanced absorption cross-section of crumpled graphene and whether we can be certain that this is not caused by chemical impurities obtained during the wet aerosolization of flakes. To answer these questions, additional experimental and theoretical investigations are required, in part using the diagnostics tools developed in this thesis.

Another promising direction for future research is the modeling of graphene folding and crumpling in the gas phase. Here, the TiRe-LII and TEM measurements at various HAN, especially in the region close to plasma, can provide the data required for model validation. The motivation for such studies lies in the properties of graphene materials that strongly depend on morphology, e.g., crumpledness. Several experimental and molecular dynamics studies have investigated the crumpling behavior of graphene sheets when wet-aerosolized with subsequent droplet drying [81,82,210–212]. The results showed that crumpling is influenced by evaporation temperature and initial flake geometry. However, there are no studies on truly freestanding graphene that is synthesized and crumpled in the gas phase, such as in this work. Ideally, when the underlying flake deformation processes are understood, the high variability of gas-phase synthesis would allow controlling the graphene level of crumpledness, thickness, and lateral size.

Appendix A

Correction of thermocouple measurement to account for radiation

Thermocouple measurements conducted in high-temperature reactive flows need to be corrected for radiative losses from the thermocouple to cooler surroundings. The correction is usually performed using the following equation:

$$T_{\mathrm{g}} = T_{\mathrm{Tc}} + \varepsilon_{\mathrm{Tc}} \sigma \left(T_{\mathrm{Tc}}^4 - T_{\mathrm{w}}^4 \right) \frac{d}{k \cdot Nu}, \tag{A.1}$$

where g refers to the gas, T_{Tc} to the thermocouple, w to the wall, $\varepsilon_{\mathrm{Tc}}$ is the emissivity of the thermocouple bead material, σ is the Stefan-Boltzmann constant, d is the thermocouple bead diameter, k is the thermal conductivity of the gas, and Nu is the Nusselt number. The wall temperature was measured with a thermocouple connected to the outer reactor wall. The Nusselt number was calculated following the Collis and Williams correlation for a cylinder in crossflow with a low Reynolds number [213]. The required temperature-dependent properties, such as thermal conductivity, density, Prandtl number, and viscosity, were taken to be those of Ar [214,215].

The main uncertainty of such a correction is the $\varepsilon_{\mathrm{Tc}}$ value. In the case when toluene was used as a precursor, large soot mass production was observed and consequently, the thermocouple was covered with black soot within a couple of minutes. Therefore, $\varepsilon_{\mathrm{Tc}} = 0.95$ was applied, as for typical graphite. In the other cases, when pure graphene or mixtures of graphene and soot were produced, the thermocouple was only partially covered in particles as observed after ejecting it from the reactor and cleaning with tissue. In such cases, optical particle pyrometry measurements were performed at the same height above the nozzle as the thermocouple measurements. The incandescence signals prior to laser excitation were collected with the 4-color TiRe-LII detection setup described in Chapter 5. The particle temperature was calculated using the Equation (5.4) and considered to be equal to the nearby gas temperature as the experiments were conducted at atmospheric pressure, and therefore, local thermal equilibrium was expected. The spectral emissivity, $\varepsilon_{\mathrm{Tc}}$ was then adjusted to make the gas temperature from Equation (A.1) match the pyrometric temperature. This approach yielded $\varepsilon_{\mathrm{Tc}} = 0.53$, which is consistent with the hypothesis that the thermocouple bead is partially covered with particles (thermocouple fully covered in black particles should yield $\varepsilon_{\mathrm{Tc}} = 0.95$, while an N-type thermocouple free of particles has $\varepsilon_{\mathrm{Tc}} = 0.1$–$0.25$). This emissivity value was used in to correct the thermocouple measurements when pure graphene or mixtures of graphene and soot were produced.

It should be noted that the temperature derived from the optical pyrometry is biased towards the hottest particles that are present in the field of view. If the hottest particles are outside of the TiRe-LII probe volume, which is approximately in the center of the reactor, then optical pyrometry correction would overestimate the $\varepsilon_{\mathrm{Tc}}$

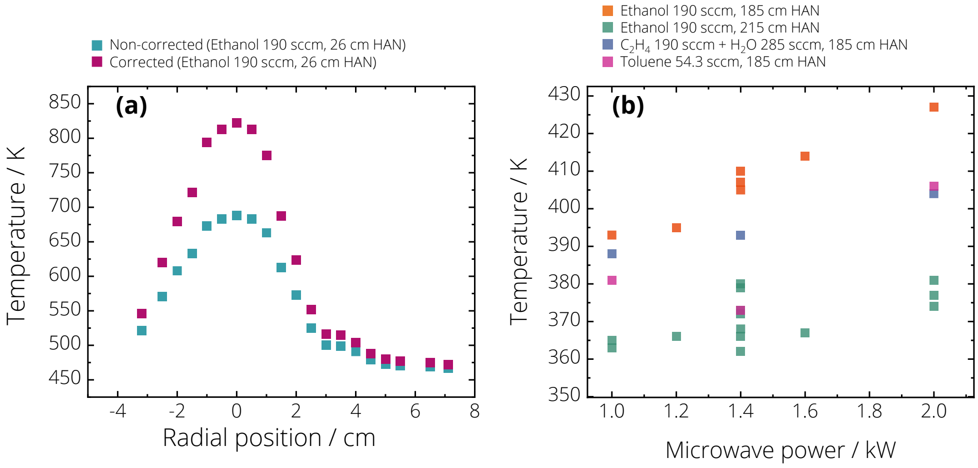

Figure A.1 Gas temperatures as measured with thermocouples at different heights above the nozzle (HAN). (a) HAN = 26 cm, before and after correction with respect to radial position. (b) HAN = 185 and 215 cm for different precursors with respect to microwave power.

value. However, Figure A.1 a shows that the radial gas temperature profile is close to symmetrical with the highest temperature in the center of the reactor, where the TiRe-LII probe volume is located.

Figure A.1 a shows the radial temperature profile at HAN = 26 cm, non-corrected and corrected, while Figure A.1 b shows the corrected measurements at HAN = 185 and 215 cm with respect to microwave power.

Appendix B
Boltzmann plot calculation

In local thermal equilibrium, the population of species in the ground and excited states follows a Boltzmann distribution, which can be used to calculate species temperature using a “Boltzmann plot”. In this work (Chapter 6), the absorption rovibrational band of CO (2020–2250 cm^{-1}) was analyzed.

$$\ln\left(\frac{\kappa_\nu}{\nu B_{12} g_1}\right) = b - kx \ , \tag{B.1}$$

where

$$k = \frac{1}{k_\mathrm{B} T}, \quad x = E_1 , \tag{B.2}$$

b is constant, E_1 is the lower state energy, ν is the wavenumber, κ_ν is the integrated spectral absorption coefficient (found by integrating the corresponding spectral absorbance peaks), B_{12} is the Einstein absorption coefficient for CO that is calculated from the Einstein emission coefficient A_{12}, and g_1 is the lower-state statistical weight. For a detailed description of the steps leading to the final form of Equation (B.1) refer to Refs. [216,217]. All the required CO parameters were taken from the HITRAN database [199]. Temperature is then found from the slope of the obtained line, which is called a Boltzmann plot.

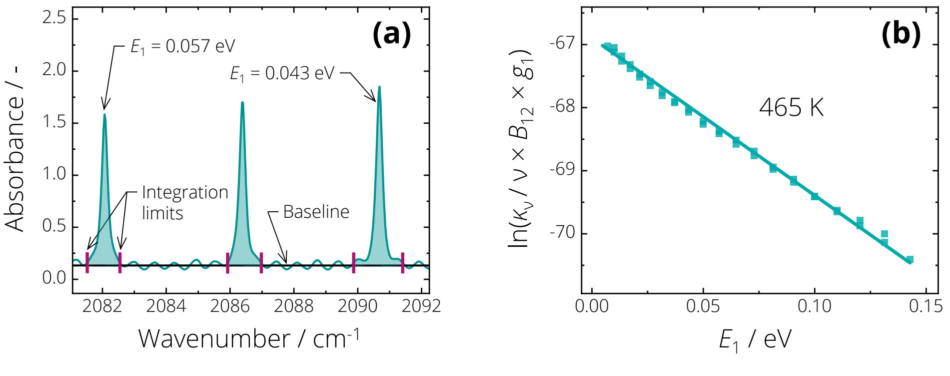

Figure B.1 (a) An example of three CO absorption peaks , which were integrated to calculate the Boltzmann plot. (b) Typical Boltzmann plot calculated for the 2020–2250 cm^{-1} rovibrational band of CO. The line slope corresponds to the gas temperature of 465 K. E_1: lower state energy; κ_ν: integrated spectral absorption coefficient; ν: wavenumber; B_{12}: Einstein coefficient; g_1: lower-state statistical weight.

Figure B.1 a shows an example of three CO absorption peaks. The baseline was subtracted, absorption peaks identified and integrated to yield κ_ν. The same procedure was applied to all the CO absorption peaks between 2020–2250 cm^{-1}, which allowed to construct the Boltzmann plot and calculate the gas temperature (Figure B.1 b).

Appendix C
Modeling graphene optical anisotropy

In order to account for graphene optical anisotropy, three different methods for assigning the direction of the refractive index were compared: (i) the plane-fit approach described below; (ii) assuming a fixed orientation for all dipoles regardless of the location of the dipole; and (iii) assuming a random orientation for each dipole.

The plane-fit approach defines a polarization tensor based on the angles formed between the incident wavefront vector and a plane fitted to the dipoles within a 7-nm radius of the wave intercept point. This method could correctly assign the direction of graphene sheets for the parts of the FLG consist of only a single layer of graphene. However, it fails to find the polarizability tensor for the regions where multiple graphene sheets intersect. At these regions, the direction of graphene sheets was chosen randomly. The final FLG flakes #1, #2, and #3 (cf., Figure 4.11) have volume equivalent diameters, d_V, of 16.2, 13.8, and 17.6 nm, respectively. Due to the random orientation of flakes in the aerosol or suspension, the average spectral cross-sections were calculated over 343 directions at each wavelength. For each of the methods, the absolute and normalized absorption efficiencies of Flake #1 in the air (refractive index of the medium $n_{\mathrm{med}} = 1$) were calculated using DDA with the refractive index from Kravets et al. [126]. Figure C.1 shows that the absolute spectral absorption cross-section depends on the method used to assign the polarizability tensor. These results also highlight that the absolute absorption cross-section depends on flake orientation, as indicated by the shaded regions. However, the normalized $Q_{\mathrm{abs},\lambda}$ spectra are almost identical, hence,

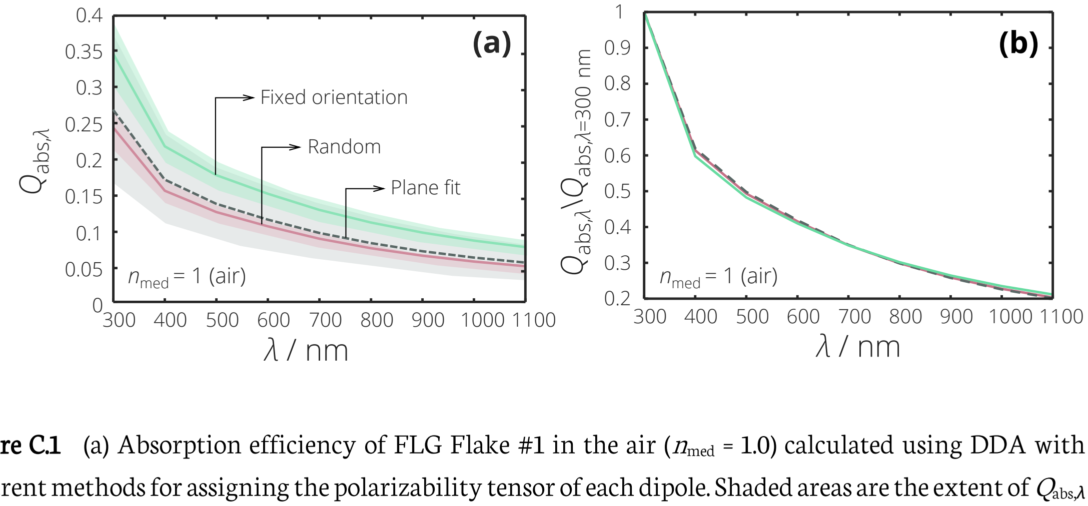

Figure C.1 (a) Absorption efficiency of FLG Flake #1 in the air ($n_{\mathrm{med}} = 1.0$) calculated using DDA with three different methods for assigning the polarizability tensor of each dipole. Shaded areas are the extent of $Q_{\mathrm{abs},\lambda}$ based on flake orientation relative to the wave vectors and its polarization. (b) The mean values of $Q_{\mathrm{abs},\lambda}$ normalized for three different methods. The mean normalized $Q_{\mathrm{abs},\lambda}$ are almost identical. Hence, no model error is expected from the plane fit approach used in this study.

the plane-fit approach was used for all DDA simulations in this study and no model error was expected for the normalized $Q_{\mathrm{abs},\lambda}$ and $Q_{\mathrm{ext},\lambda}$.

References

[1] K.S. Novoselov, A.K. Geim, S.V. Morozov, D. Jiang, Y. Zhang, S.V. Dubonos, I.V. Grigorieva, A.A. Firsov, Electric Field Effect in Atomically Thin Carbon Films, Science 306 (2004) 666–669.

[2] N.M. Julkapli, S. Bagheri, Graphene supported heterogeneous catalysts: An overview, Int. J. Hydrog. Energy 40 (2015) 948–979.

[3] M.D. Stoller, S. Park, Y. Zhu, J. An, R.S. Ruoff, Graphene-Based Ultracapacitors, Nano Lett. 8 (2008) 3498–3502.

[4] L. Dai, Functionalization of Graphene for Efficient Energy Conversion and Storage, Acc. Chem. Res. 46 (2013) 31–42.

[5] E. Pop, V. Varshney, A.K. Roy, Thermal properties of graphene: Fundamentals and applications, MRS Bull. 37 (2012) 1273–1281.

[6] R. Raccichini, A. Varzi, S. Passerini, B. Scrosati, The role of graphene for electrochemical energy storage, Nat. Mater. 14 (2015) 271–279.

[7] Z. Yan, D.L. Nika, A.A. Balandin, Thermal properties of graphene and few-layer graphene: applications in electronics, IET Circuits Devices Syst. 9 (2015) 4–12.

[8] A. King, G. Johnson, D. Engelberg, W. Ludwig, J. Marrow, Observations of Intergranular Stress Corrosion Cracking in a Grain-Mapped Polycrystal, Science 321 (2008) 382–385.

[9] J.-U. Lee, D. Yoon, H. Cheong, Estimation of Young's Modulus of Graphene by Raman Spectroscopy, Nano Lett. 12 (2012) 4444–4448.

[10] The Graphene Council: The 2020 Graphene Survey. Available at: https://www.thegraphenecouncil.org. Accessed June 21, 2022.

[11] A.P. Kauling, A.T. Seefeldt, D.P. Pisoni, R.C. Pradeep, R. Bentini, R.V.B. Oliveira, K.S. Novoselov, A.H. Castro Neto, The Worldwide Graphene Flake Production, Adv. Mater. 30 (2018) 1803784.

[12] A. Dato, Graphene synthesized in atmospheric plasmas—A review, J. Mater. Res. 34 (2019) 214–230.

[13] J.W. McClure, Diamagnetism of Graphite, Phys. Rev. 104 (1956) 666–671.

[14] P.R. Wallace, The Band Theory of Graphite, Phys. Rev. 71 (1947) 622–634.

[15] J.C. Slonczewski, P.R. Weiss, Band Structure of Graphite, Phys. Rev. 109 (1958) 272–279.

[16] H.P. Boehm, A. Clauss, G. Fischer, U. Hoffmann, Surface properties of extremely thin graphite lamellae, Proc. Fifth Conf. Carbon (1962) 73–80.

[17] H.P. Boehm., A. Clauss, G.O. Fischer, U. Hofmann, Dünnste Kohlenstoff-Folien, Z. Für Naturforschung B 17 (1962) 150–153.

[18] H.P. Boehm, R. Setton, E. Stumpp, Nomenclature and terminology of graphite intercalation compounds, Carbon 24 (1986) 241–245.

[19] R. Kumar, E. Joanni, R.K. Singh, D.P. Singh, S.A. Moshkalev, Recent advances in the synthesis and modification of carbon-based 2D materials for application in energy conversion and storage, Prog. Energy Combust. Sci. 67 (2018) 115–157.

[20] R. Kumar, S. Sahoo, E. Joanni, R.K. Singh, W.K. Tan, K.K. Kar, A. Matsuda, Recent progress in the synthesis of graphene and derived materials for next generation electrodes of high performance lithium ion batteries, Prog. Energy Combust. Sci. 75 (2019) 100786.

[21] X. Huang, Z. Yin, S. Wu, X. Qi, Q. He, Q. Zhang, Q. Yan, F. Boey, H. Zhang, Graphene-Based Materials: Synthesis, Characterization, Properties, and Applications, Small 7 (2011) 1876–1902.

[22] J. Zhao, H. Liu, Z. Yu, R. Quhe, S. Zhou, Y. Wang, C.C. Liu, H. Zhong, N. Han, J. Lu, Y. Yao, K. Wu, Rise of silicene: A competitive 2D material, Prog. Mater. Sci. 83 (2016) 24–151.

[23] N.R. Glavin, R. Rao, V. Varshney, E. Bianco, A. Apte, A. Roy, E. Ringe, P.M. Ajayan, Emerging Applications of Elemental 2D Materials, Adv. Mater. 32 (2020) 1904302.

[24] K. Khan, A.K. Tareen, M. Aslam, R. Wang, Y. Zhang, A. Mahmood, Z. Ouyang, H. Zhang, Z. Guo, Recent developments in emerging two-dimensional materials and their applications, J. Mater. Chem. C 8 (2020) 387–440.

[25] Y. Gogotsi, B. Anasori, The Rise of MXenes, ACS Nano 13 (2019) 8491–8494.

[26] L. Mao, C.C. Stoumpos, M.G. Kanatzidis, Two-Dimensional Hybrid Halide Perovskites: Principles and Promises, J. Am. Chem. Soc. 141 (2019) 1171–1190.

[27] G. Cheon, K.-A.N. Duerloo, A.D. Sendek, C. Porter, Y. Chen, E.J. Reed, Data Mining for New Two- and One-Dimensional Weakly Bonded Solids and Lattice-Commensurate Heterostructures, Nano Lett. 17 (2017) 1915–1923.

[28] J. Molina, Graphene-based fabrics and their applications: a review, RSC Adv. 6 (2016) 68261–68291.

[29] A.C. Ferrari, F. Bonaccorso, V. Fal'ko, K.S. Novoselov, S. Roche, P. Bøggild, S. Borini, F.H.L. Koppens, V. Palermo, N. Pugno, J.A. Garrido, R. Sordan, A. Bianco, L. Ballerini, M. Prato, E. Lidorikis, J. Kivioja, C. Marinelli, T. Ryhänen, A. Morpurgo, J.N. Coleman, V. Nicolosi, L. Colombo, A. Fert, M. Garcia-Hernandez, A. Bachtold, G.F. Schneider, F. Guinea, C. Dekker, M. Barbone, Z. Sun, C. Galiotis, A.N. Grigorenko, G. Konstantatos, A. Kis, M. Katsnelson, L. Vandersypen, A. Loiseau, V. Morandi, D. Neumaier, E. Treossi, V. Pellegrini, M. Polini, A. Tredicucci, G.M. Williams, B. Hee Hong, J.-H. Ahn, J. Min Kim, H. Zirath, B.J. van Wees, H. van der Zant, L. Occhipinti, A. Di Matteo, I.A. Kinloch, T. Seyller, E. Quesnel, X. Feng, K. Teo, N. Rupesinghe, P. Hakonen, S.R.T. Neil, Q. Tannock, T. Löfwander, J. Kinaret, Science and technology roadmap for graphene, related two-dimensional crystals, and hybrid systems, Nanoscale 7 (2015) 4598–4810.

[30] R. Karthick, F. Chen, Free-standing graphene paper for energy application: Progress and future scenarios, Carbon 150 (2019) 292–310.

[31] D.C. Marcano, D.V. Kosynkin, J.M. Berlin, A. Sinitskii, Z. Sun, A. Slesarev, L.B. Alemany, W. Lu, J.M. Tour, Improved Synthesis of Graphene Oxide, ACS Nano 4 (2010) 4806–4814.

[32] C. Gómez-Navarro, R.T. Weitz, A.M. Bittner, M. Scolari, A. Mews, M. Burghard, K. Kern, Electronic Transport Properties of Individual Chemically Reduced Graphene Oxide Sheets, Nano Lett. 7 (2007) 3499–3503.

[33] M. Houmad, H. Zaari, A. Benyoussef, A. El Kenz, H. Ez-Zahraouy, Optical conductivity enhancement and band gap opening with silicon doped graphene, Carbon 94 (2015) 1021–1027.

[34] A. Münzer, L. Xiao, Y.H. Sehlleier, C. Schulz, H. Wiggers, All gas-phase synthesis of graphene: Characterization and its utilization for silicon-based lithium-ion batteries, Electrochimica Acta 272 (2018) 52–59.

[35] Y. Wang, Y. Shao, D.W. Matson, J. Li, Y. Lin, Nitrogen-Doped Graphene and Its Application in Electrochemical Biosensing, ACS Nano 4 (2010) 1790–1798.

[36] The Graphene Classification Framework. Available at: https://www.thegraphenecouncil.org/page/GCF. Accessed June 17, 2022.

[37] Y. Hernandez, V. Nicolosi, M. Lotya, F.M. Blighe, Z. Sun, S. De, I.T. McGovern, B. Holland, M. Byrne, Y.K. Gun'Ko, J.J. Boland, P. Niraj, G. Duesberg, S. Krishnamurthy, R. Goodhue, J. Hutchison, V. Scardaci, A.C. Ferrari, J.N. Coleman, High-yield production of graphene by liquid-phase exfoliation of graphite, Nat. Nanotechnol. 3 (2008) 563–568.

[38] Y. Lv, L. Yu, C. Jiang, S. Chen, Z. Nie, Synthesis of graphene nanosheet powder with layer number control via a soluble salt-assisted route, RSC Adv. 4 (2014) 13350.

[39] C.-M. Seah, S.-P. Chai, A.R. Mohamed, Mechanisms of graphene growth by chemical vapour deposition on transition metals, Carbon 70 (2014) 1–21.

[40] K.V. Emtsev, A. Bostwick, K. Horn, J. Jobst, G.L. Kellogg, L. Ley, J.L. McChesney, T. Ohta, S.A. Reshanov, J. Röhrl, E. Rotenberg, A.K. Schmid, D. Waldmann, H.B. Weber, T. Seyller, Towards wafer-size graphene layers by atmospheric pressure graphitization of silicon carbide, Nat. Mater. 8 (2009) 203–207.

[41] M.J. McAllister, J.-L. Li, D.H. Adamson, H.C. Schniepp, A.A. Abdala, J. Liu, M. Herrera-Alonso, D.L. Milius, R. Car, R.K. Prud'homme, I.A. Aksay, Single Sheet Functionalized Graphene by Oxidation and Thermal Expansion of Graphite, Chem. Mater. 19 (2007) 4396–4404.

[42] A. Dato, V. Radmilovic, Z. Lee, J. Phillips, M. Frenklach, Substrate-Free Gas-Phase Synthesis of Graphene Sheets, Nano Lett. 8 (2008) 2012–2016.

[43] M. Choucair, P. Thordarson, J.A. Stride, Gram-scale production of graphene based on solvothermal synthesis and sonication, Nat. Nanotechnol. 4 (2009) 30–33.

[44] Z. Sun, Z. Yan, J. Yao, E. Beitler, Y. Zhu, J.M. Tour, Growth of graphene from solid carbon sources, Nature 468 (2010) 549–552.

[45] A. Kovtun, E. Treossi, N. Mirotta, A. Scidà, A. Liscio, M. Christian, F. Valorosi, A. Boschi, R.J. Young, C. Galiotis, I.A. Kinloch, V. Morandi, V. Palermo, Benchmarking of graphene-based materials: real commercial products versus ideal graphene, 2D Mater. 6 (2019) 025006.

[46] ISO/TS 80004-13:2017, Nanotechnologies — Vocabulary — Part 13: Graphene and related two-dimensional (2D) materials, 2017.

[47] ISO/TS 21356-1:2021, Nanotechnologies — Structural characterization of graphene — Part 1: Graphene from powders and dispersions, 2021.

[48] Graphene Flagship Standardisation. Available at: https://graphene-flagship.eu/innovation/industrialisation/standardisation. Accessed June 17, 2022.

[49] P. Wick, A.E. Louw-Gaume, M. Kucki, H.F. Krug, K. Kostarelos, B. Fadeel, K.A. Dawson, A. Salvati, E. Vázquez, L. Ballerini, M. Tretiach, F. Benfenati, E. Flahaut, L. Gauthier, M. Prato, A. Bianco, Classification Framework for Graphene-Based Materials, Angew. Chem. Int. Ed. 53 (2014) 7714–7718.

[50] B. Fadeel, C. Bussy, S. Merino, E. Vázquez, E. Flahaut, F. Mouchet, L. Evariste, L. Gauthier, A.J. Koivisto, U. Vogel, C. Martín, L.G. Delogu, T. Buerki-Thurnherr, P. Wick, D. Beloin-Saint-Pierre, R. Hischier, M. Pelin, F. Candotto Carniel, M. Tretiach, F. Cesca, F. Benfenati, D. Scaini, L. Ballerini, K. Kostarelos, M. Prato, A. Bianco, Safety Assessment of Graphene-Based Materials: Focus on Human Health and the Environment, ACS Nano 12 (2018) 10582–10620.

[51] A. Ruiz, M.A. Lucherelli, D. Murera, D. Lamon, C. Ménard-Moyon, A. Bianco, Toxicological evaluation of highly water dispersible few-layer graphene in vivo, Carbon 170 (2020) 347–360.

[52] L. Ou, B. Song, H. Liang, J. Liu, X. Feng, B. Deng, T. Sun, L. Shao, Toxicity of graphene-family nanoparticles: a general review of the origins and mechanisms, Part. Fibre Toxicol. 13 (2016).

[53] M. Ema, M. Gamo, K. Honda, A review of toxicity studies on graphene-based nanomaterials in laboratory animals, Regul. Toxicol. Pharmacol. 85 (2017) 7–24.

[54] M. Pelin, S. Sosa, M. Prato, A. Tubaro, Occupational exposure to graphene based nanomaterials: risk assessment, Nanoscale 10 (2018) 15894–15903.

[55] P. Fortugno, S. Musikhin, X. Shi, H. Wang, H. Wiggers, C. Schulz, Synthesis of freestanding few-layer graphene in microwave plasma: The role of oxygen, Carbon 186 (2022) 560–573.

[56] J. Toman, O. Jašek, M. Šnírer, D. Pavliňák, Z. Navrátil, J. Jurmanová, S. Chudják, F. Krčma, V. Kudrle, J. Michalička, On the transition of reaction pathway during microwave plasma gas-phase synthesis of graphene nanosheets: From amorphous to highly crystalline structure, Plasma Process. Polym. 18 (2021) 2100008.

[57] D. Tsyganov, N. Bundaleska, A. Dias, J. Henriques, E. Felizardo, M. Abrashev, J. Kissovski, A.M.B. do Rego, A.M. Ferraria, E. Tatarova, Microwave plasma-based direct synthesis of free-standing N-graphene, Phys. Chem. Chem. Phys. 22 (2020) 4772–4787.

[58] A. Casanova, R. Rincón, J. Muñoz, C.O. Ania, M.D. Calzada, Optimizing high-quality graphene nanoflakes production through organic (bio)-precursor plasma decomposition, Fuel Process. Technol. 212 (2021) 106630.

[59] J. Toman, O. Jasek, M. Snirer, V. Kudrle, J. Jurmanova, On the interplay between plasma discharge instability and formation of free-standing graphene nanosheets in a dual-channel microwave plasma torch at atmospheric pressure, J. Phys. Appl. Phys. 52 (2019) 265205.

[60] O. Jašek, J. Toman, M. Šnírer, J. Jurmanová, V. Kudrle, J. Michalička, D. Všianský, D. Pavliňák, Microwave plasma-based high temperature dehydrogenation of hydrocarbons and alcohols as a single route to highly efficient gas phase synthesis of freestanding graphene, Nanotechnology 32 (2021) 505608.

[61] A. Dato, M. Frenklach, Substrate-free microwave synthesis of graphene: experimental conditions and hydrocarbon precursors, New J. Phys. 12 (2010) 125013.

[62] D. Tsyganov, N. Bundaleska, E. Tatarova, C.M. Ferreira, Ethanol reforming into hydrogen-rich gas applying microwave ‘tornado’-type plasma, Int. J. Hydrog. Energy 38 (2013) 14512–14530.

[63] D. Tsyganov, N. Bundaleska, E. Tatarova, A. Dias, J. Henriques, A. Rego, A. Ferraria, M.V. Abrashev, F.M. Dias, C.C. Luhrs, J. Phillips, On the plasma-based growth of ‘flowing’ graphene sheets at atmospheric pressure conditions, Plasma Sources Sci. Technol. 25 (2016) 015013.

[64] E. Tatarova, J. Henriques, C.C. Luhrs, A. Dias, J. Phillips, M.V. Abrashev, C.M. Ferreira, Microwave plasma based single step method for free standing graphene synthesis at atmospheric conditions, Appl. Phys. Lett. 103 (2013) 134101.

[65] G. Leon, J.W. Martin, E.J. Bringley, J. Akroyd, M. Kraft, The role of oxygenated species in the growth of graphene, fullerenes and carbonaceous particles, Carbon 182 (2021) 203–213.

[66] S. Musikhin, P. Fortugno, J.C. Corbin, G.J. Smallwood, T. Dreier, K.J. Daun, C. Schulz, Characterization of few-layer graphene aerosols by laser-induced incandescence, Carbon 167 (2020) 870–880.

[67] M. Fronczak, A.M. Keszler, M. Mohai, B. Jezsó, A. Farkas, Z. Károly, Facile and continuous synthesis of graphene nanoflakes in RF thermal plasma, Carbon 193 (2022) 51–67.

[68] A. Miller, G. Frey, G. King, C. Sunderman, A Handheld Electrostatic Precipitator for Sampling Airborne Particles and Nanoparticles, Aerosol Sci. Technol. 44 (2010) 417–427.

[69] A.C. Ferrari, Raman spectroscopy of graphene and graphite: Disorder, electron–phonon coupling, doping and nonadiabatic effects, Solid State Commun. 143 (2007) 47–57.

[70] A.C. Ferrari, J.C. Meyer, V. Scardaci, C. Casiraghi, M. Lazzeri, F. Mauri, S. Piscanec, D. Jiang, K.S. Novoselov, S. Roth, A.K. Geim, Raman Spectrum of Graphene and Graphene Layers, Phys. Rev. Lett. 97 (2006).

[71] L.M. Malard, M.A. Pimenta, G. Dresselhaus, M.S. Dresselhaus, Raman spectroscopy in graphene, Phys. Rep. 473 (2009) 51–87.

[72] A. Sadezky, H. Muckenhuber, H. Grothe, R. Niessner, U. Pöschl, Raman microspectroscopy of soot and related carbonaceous materials: Spectral analysis and structural information, Carbon 43 (2005) 1731–1742.

[73] D. Briggs, Surface Analysis of Polymers by XPS and Static SIMS, Cambridge University Press, Cambridge, 1998.

[74] F. Sette, G.K. Wertheim, Y. Ma, G. Meigs, S. Modesti, C.T. Chen, Lifetime and screening of the C 1s photoemission in graphite, Phys. Rev. B 41 (1990) 9766–9770.

[75] J.C. Lascovich, S. Scaglione, Comparison among XAES, PELS and XPS techniques for evaluation of Sp2 percentage in a-C:H, Appl. Surf. Sci. 78 (1994) 17–23.

[76] B.J. Jones, J.J. Ojeda, Substrate and material transfer effects on the surface chemistry and texture of diamond-like carbon deposited by plasma-enhanced chemical vapour deposition, Surf. Interface Anal. 44 (2012) 1187–1192.

[77] B. Lesiak, L. Kövér, J. Tóth, J. Zemek, P. Jiricek, A. Kromka, N. Rangam, C sp2/sp3 hybridisations in carbon nanomaterials – XPS and (X)AES study, Appl. Surf. Sci. 452 (2018) 223–231.

[78] C.A. Clifford, E.H. Martins Ferreira, T. Fujimoto, J. Herrmann, A.R. Hight Walker, D. Koltsov, C. Punckt, L. Ren, G.J. Smallwood, A.J. Pollard, The importance of international standards for the graphene community, Nat. Rev. Phys. 3 (2021) 233–235.

[79] Sun Yangyong, Zhang Jin, Strategies for Scalable Gas-Phase Preparation of Free-Standing Graphene, CCS Chem. 3 (2020) 1058–1077.

[80] S.W. Cranford, M.J. Buehler, Packing efficiency and accessible surface area of crumpled graphene, Phys. Rev. B 84 (2011) 205451.

[81] M. Becton, L. Zhang, X. Wang, On the crumpling of polycrystalline graphene by molecular dynamics simulation, Phys. Chem. Chem. Phys. 17 (2015) 6297–6304.

[82] Y. Liao, Z. Li, Fatima, W. Xia, Size-dependent structural behaviors of crumpled graphene sheets, Carbon 174 (2021) 148–157.

[83] T.C. Bond, S.J. Doherty, D.W. Fahey, P.M. Forster, T. Berntsen, B.J. DeAngelo, M.G. Flanner, S. Ghan, B. Kärcher, D. Koch, S. Kinne, Y. Kondo, P.K. Quinn, M.C. Sarofim, M.G. Schultz, M. Schulz, C. Venkataraman, H. Zhang, S. Zhang, N. Bellouin, S.K. Guttikunda, P.K. Hopke, M.Z. Jacobson, J.W. Kaiser, Z. Klimont, U. Lohmann, J.P. Schwarz, D. Shindell, T. Storelvmo, S.G. Warren, C.S. Zender, Bounding the role of black carbon in the climate system: A scientific assessment, J. Geophys. Res. Atmospheres 118 (2013) 5380–5552.

[84] C. Mansilla Wettstein, F.P. Bonafé, M.B. Oviedo, C.G. Sánchez, Optical properties of graphene nanoflakes: Shape matters, J. Chem. Phys. 144 (2016) 224305.

[85] C.D. Zangmeister, R. You, E.M. Lunny, A.E. Jacobson, M. Okumura, M.R. Zachariah, J.G. Radney, Measured in-situ mass absorption spectra for nine forms of highly-absorbing carbonaceous aerosol, Carbon 136 (2018) 85–93.

[86] M. Owen, G. Mulholland, W. Guthrie, Condensation Particle Counter Proportionality Calibration from 1 Particle·cm^{-3} to 10^4 Particles·cm^{-3}, Aerosol Sci. Technol. 46 (2012) 444–450.

[87] A. Wiedensohler, An approximation of the bipolar charge distribution for particles in the submicron size range, J. Aerosol Sci. 19 (1988) 387–389.

[88] T.J. Johnson, M. Irwin, J.P.R. Symonds, J.S. Olfert, A.M. Boies, Measuring aerosol size distributions with the aerodynamic aerosol classifier, Aerosol Sci. Technol. 52 (2018) 655–665.

[89] J.Y. Park, P.H. McMurry, K. Park, Production of Residue-Free Nanoparticles by Atomization of Aqueous Solutions, Aerosol Sci. Technol. 46 (2012) 354–360.

[90] TSI Inc., Model 3076 Constant Output Atomizer Instruction Manual (2005).

[91] P.F. DeCarlo, J.G. Slowik, D.R. Worsnop, P. Davidovits, J.L. Jimenez, Particle Morphology and Density Characterization by Combined Mobility and Aerodynamic Diameter Measurements. Part 1: Theory, Aerosol Sci. Technol. 38 (2004) 1185–1205.

[92] B.K. Ku, P. Kulkarni, Measurement of transport properties of aerosolized nanomaterials, J. Aerosol Sci. 90 (2015) 169–181.

[93] M. Li, R. You, G.W. Mulholland, M.R. Zachariah, Evaluating the Mobility of Nanorods in Electric Fields, Aerosol Sci. Technol. 47 (2013) 1101–1107.

[94] W.C. Hinds, Aerosol technology: properties, behavior, and measurement of airborne particles, 2nd ed, Wiley, New York, 1999.

[95] Human respiratory tract model for radiological protection. A report of a Task Group of the International Commission on Radiological Protection, 1994.

[96] A. Schinwald, F.A. Murphy, A. Jones, W. MacNee, K. Donaldson, Graphene-Based Nanoplatelets: A New Risk to the Respiratory System as a Consequence of Their Unusual Aerodynamic Properties, ACS Nano 6 (2012) 736–746.

[97] W.-C. Su, B.K. Ku, P. Kulkarni, Y.S. Cheng, Deposition of graphene nanomaterial aerosols in human upper airways, J. Occup. Environ. Hyg. 13 (2016) 48–59.

[98] A. Ångström, On the Atmospheric Transmission of Sun Radiation and on Dust in the Air, Geogr. Ann. 11 (1929) 156–166.

[99] C. Liu, C.E. Chung, Y. Yin, M. Schnaiter, The absorption Ångström exponent of black carbon: from numerical aspects, Atmospheric Chem. Phys. 18 (2018) 6259–6273.

[100] A. Bescond, J. Yon, F.-X. Ouf, C. Rozé, A. Coppalle, P. Parent, D. Ferry, C. Laffon, Soot optical properties determined by analyzing extinction spectra in the visible near-UV: Toward an optical speciation according to constituents and structure, J. Aerosol Sci. 101 (2016) 118–132.

[101] T.C. Bond, Spectral dependence of visible light absorption by carbonaceous particles emitted from coal combustion, Geophys. Res. Lett. 28 (2001) 4075–4078.

[102] J.C. Corbin, H. Czech, D. Massabò, F.B. de Mongeot, G. Jakobi, F. Liu, P. Lobo, C. Mennucci, A.A. Mensah, J. Orasche, S.M. Pieber, A.S.H. Prévôt, B. Stengel, L.-L. Tay, M. Zanatta, R. Zimmermann, I. El Haddad, M. Gysel, Infrared-absorbing carbonaceous tar can dominate light absorption by marine-engine exhaust, Npj Clim. Atmospheric Sci. 2 (2019) 12.

[103] T.B. Onasch, P. Massoli, P.L. Kebabian, F.B. Hills, F.W. Bacon, A. Freedman, Single Scattering Albedo Monitor for Airborne Particulates, Aerosol Sci. Technol. 49 (2015) 267–279.

[104] R.L. Modini, J.C. Corbin, B.T. Brem, M. Irwin, M. Bertò, R.E. Pileci, P. Fetfatzis, K. Eleftheriadis, B. Henzing, M.M. Moerman, F. Liu, T. Müller, M. Gysel-Beer, Detailed characterization of the CAPS single-scattering albedo monitor (CAPS PMssa) as a field-deployable instrument for measuring aerosol light absorption with the extinction-minus-scattering method, Atmospheric Meas. Tech. 14 (2021) 819–851.

[105] W.P. Arnott, K. Hamasha, H. Moosmüller, P.J. Sheridan, J.A. Ogren, Towards Aerosol Light-Absorption Measurements with a 7-Wavelength Aethalometer: Evaluation with a Photoacoustic Instrument and 3-Wavelength Nephelometer, Aerosol Sci. Technol. 39 (2005) 17–29.

[106] E. Weingartner, H. Saathoff, M. Schnaiter, N. Streit, B. Bitnar, U. Baltensperger, Absorption of light by soot particles: determination of the absorption coefficient by means of aethalometers, J. Aerosol Sci. 34 (2003) 1445–1463.

[107] H. Rosen, T. Novakov, Optical transmission through aerosol deposits on diffusely reflective filters: a method for measuring the absorbing component of aerosol particles, Appl. Opt. 22 (1983) 1265–1267.

[108] J.C. Corbin, S.M. Pieber, H. Czech, M. Zanatta, G. Jakobi, D. Massabò, J. Orasche, I. El Haddad, A.A. Mensah, B. Stengel, L. Drinovec, G. Mocnik, R. Zimmermann, A.S.H. Prévôt, M. Gysel, Brown and Black Carbon Emitted by a Marine Engine Operated on Heavy Fuel Oil and Distillate Fuels: Optical Properties, Size Distributions, and Emission Factors, J. Geophys. Res. Atmospheres 123 (2018) 6175–6195.

[109] L. Drinovec, G. Močnik, P. Zotter, A.S.H. Prévôt, C. Ruckstuhl, E. Coz, M. Rupakheti, J. Sciare, T. Müller, A. Wiedensohler, A.D.A. Hansen, The "dual-spot" Aethalometer: an improved measurement of aerosol black carbon with real-time loading compensation, Atmospheric Meas. Tech. 8 (2015) 1965–1979.

[110] S. Uran, A. Alhani, C. Silva, Study of ultraviolet-visible light absorbance of exfoliated graphite forms, AIP Adv. 7 (2017) 035323.

[111] G. Eda, Y.-Y. Lin, C. Mattevi, H. Yamaguchi, H.-A. Chen, I.-S. Chen, C.-W. Chen, M. Chhowalla, Blue Photoluminescence from Chemically Derived Graphene Oxide, Adv. Mater. 22 (2010) 505–509.

[112] T.C. Bond, R.W. Bergstrom, Light Absorption by Carbonaceous Particles: An Investigative Review, Aerosol Sci. Technol. 40 (2006) 27–67.

[113] F. Liu, J. Yon, A. Fuentes, P. Lobo, G.J. Smallwood, J.C. Corbin, Review of recent literature on the light absorption properties of black carbon: Refractive index, mass absorption cross section, and absorption function, Aerosol Sci. Technol. 54 (2020) 33–51.

[114] C. Backes, K.R. Paton, D. Hanlon, S. Yuan, M.I. Katsnelson, J. Houston, R.J. Smith, D. McCloskey, J.F. Donegan, J.N. Coleman, Spectroscopic metrics allow in situ measurement of mean size and thickness of liquid-exfoliated few-layer graphene nanosheets, Nanoscale 8 (2016) 4311–4323.

[115] J.C. Corbin, A. Moallemi, F. Liu, S. Gagné, J.S. Olfert, G.J. Smallwood, P. Lobo, Closure between particulate matter concentrations measured ex situ by thermal–optical analysis and in situ by the CPMA–electrometer reference mass system, Aerosol Sci. Technol. 54 (2020) 1293–1309.

[116] G. Biskos, K. Reavell, N. Collings, Unipolar diffusion charging of aerosol particles in the transition regime, J. Aerosol Sci. 36 (2005) 247–265.

[117] J.P.R. Symonds, K.St.J. Reavell, J.S. Olfert, The CPMA-Electrometer System—A Suspended Particle Mass Concentration Standard, Aerosol Sci. Technol. 47 (2013) i–iv.

[118] J.C. Corbin, T.J. Johnson, F. Liu, T.A. Sipkens, M.P. Johnson, P. Lobo, G.J. Smallwood, Size-dependent mass absorption cross-section of soot particles from various sources, Carbon 192 (2022) 438–451.

[119] T.A. Sipkens, J.S. Olfert, S.N. Rogak, New approaches to calculate the transfer function of particle mass analyzers, Aerosol Sci. Technol. 54 (2020) 111–127.

[120] M. Dickau, T. J. Johnson, K. Thomson, G. Smallwood, J. S. Olfert, Demonstration of the CPMA-Electrometer System for Calibrating Black Carbon Particulate Mass Instruments, Aerosol Sci. Technol. 49 (2015) 152–158.

[121] R. Dastanpour, A. Momenimovahed, K. Thomson, J. Olfert, S. Rogak, Variation of the optical properties of soot as a function of particle mass, Carbon 124 (2017) 201–211.

[122] K.A. Fuller, W.C. Malm, S.M. Kreidenweis, Effects of mixing on extinction by carbonaceous particles, J. Geophys. Res. Atmospheres 104 (1999) 15941–15954.

[123] H. DeVoe, Optical Properties of Molecular Aggregates. I. Classical Model of Electronic Absorption and Refraction, J. Chem. Phys. 41 (1964) 393–400.

[124] Purcell, Pennypacker, Scattering and absorption of light by nonspherical dielectric grains, Astrophys. J. 186 (1973) 705–714.

[125] C.M. Sorensen, Light Scattering by Fractal Aggregates: A Review, Aerosol Sci. Technol. 35 (2001) 648–687.

[126] V.G. Kravets, A.N. Grigorenko, R.R. Nair, P. Blake, S. Anissimova, K.S. Novoselov, A.K. Geim, Spectroscopic ellipsometry of graphene and an exciton-shifted van Hove peak in absorption, Phys. Rev. B 81 (2010) 155413.

[127] L.A. Falkovsky, Optical properties of graphene and IV–VI semiconductors, Phys.-Uspekhi 51 (2008) 887–897.

[128] J.W. Weber, V.E. Calado, M.C.M. van de Sanden, Optical constants of graphene measured by spectroscopic ellipsometry, Appl. Phys. Lett. 97 (2010) 091904.

[129] G.G. Politano, C. Vena, G. Desiderio, C. Versace, Variable angle spectroscopic ellipsometry characterization of turbostratic CVD-grown bilayer and trilayer graphene, Opt. Mater. 107 (2020) 110165.

[130] E. Ochoa-Martínez, M. Gabás, L. Barrutia, A. Pesquera, A. Centeno, S. Palanco, A. Zurutuza, C. Algora, Determination of a refractive index and an extinction coefficient of standard production of CVD-graphene, Nanoscale 7 (2015) 1491–1500.

[131] Z. Pápa, J. Csontos, T. Smausz, Z. Toth, J. Budai, Spectroscopic ellipsometric investigation of graphene and thin carbon films from the point of view of depolarization effects, Appl. Surf. Sci. 421 (2017) 714–721.

[132] A.B. Djurišić, E.H. Li, Optical properties of graphite, J. Appl. Phys. 85 (1999) 7404–7410.

[133] M.R. Querry, Optical Constants, Missouri Univ., Kansas City, 1985.

[134] B.D.A. Levin, Y. Jiang, E. Padgett, S. Waldon, C. Quammen, C. Harris, U. Ayachit, M. Hanwell, P. Ercius, D.A. Muller, R. Hovden, Tutorial on the Visualization of Volumetric Data Using *tomviz*, Microsc. Today 26 (2018) 12–17.

[135] C. Pecharromán, G. Mata-Osoro, L.A. Díaz, R. Torrecillas, J.S. Moya, On the transparency of nanostructured alumina: Rayleigh-Gans model for anisotropic spheres, Opt. Express 17 (2009) 6899.

[136] S. Deng, V. Berry, Wrinkled, rippled and crumpled graphene: an overview of formation mechanism, electronic properties, and applications, Mater. Today 19 (2016) 197–212.

[137] K.-K. Bai, Y. Zhou, H. Zheng, L. Meng, H. Peng, Z. Liu, J.-C. Nie, L. He, Creating One-Dimensional Nanoscale Periodic Ripples in a Continuous Mosaic Graphene Monolayer, Phys. Rev. Lett. 113 (2014) 086102.

[138] F.J.T. Huber, S. Will, K.J. Daun, Sizing aerosolized fractal nanoparticle aggregates through Bayesian analysis of wide-angle light scattering (WALS) data, J. Quant. Spectrosc. Radiat. Transf. 184 (2016) 27–39.

[139] S. Talebi-Moghaddam, F.J. Bauer, F.J.T. Huber, S. Will, K.J. Daun, Inferring soot morphology through multi-angle light scattering using an artificial neural network, J. Quant. Spectrosc. Radiat. Transf. 251 (2020) 106957.

[140] B. Partoens, F.M. Peeters, From graphene to graphite: Electronic structure around the K point, Phys. Rev. B 74 (2006) 075404.

[141] W. Zhu, T. Low, V. Perebeinos, A.A. Bol, Y. Zhu, H. Yan, J. Tersoff, P. Avouris, Structure and Electronic Transport in Graphene Wrinkles, Nano Lett. 12 (2012) 3431–3436.

[142] E. Kim, H. Kim, B.-J. Park, Y.-H. Han, J.H. Park, J. Cho, S.-S. Lee, J.G. Son, Etching-Assisted Crumpled Graphene Wrapped Spiky Iron Oxide Particles for High-Performance Li-Ion Hybrid Supercapacitor, Small 14 (2018) 1704209.

[143] Y. Xiao, Z. Cheng, Y. Zhao, L. Qu, Highly crumpled nanocarbons as efficient metal-free electrocatalysts for zinc–air batteries, Nanoscale 10 (2018) 15706–15713.

[144] Y.S. Yun, Y.-U. Park, S.-J. Chang, B.H. Kim, J. Choi, J. Wang, D. Zhang, P.V. Braun, H.-J. Jin, K. Kang, Crumpled graphene paper for high power sodium battery anode, Carbon 99 (2016) 658–664.

[145] H.A. Michelsen, C. Schulz, G.J. Smallwood, S. Will, Laser-induced incandescence: Particulate diagnostics for combustion, atmospheric, and industrial applications, Prog. Energy Combust. Sci. 51 (2015) 2–48.

[146] D.R. Snelling, G.J. Smallwood, F. Liu, Ö.L. Gülder, W.D. Bachalo, A calibration-independent laser-induced incandescence technique for soot measurement by detecting absolute light intensity, Appl. Opt. 44 (2005) 6773.

[147] T. Sipkens, G. Joshi, K.J. Daun, Y. Murakami, Sizing of molybdenum nanoparticles using time-resolved laser-induced incandescence, J. Heat Transf. 135 (2013) 052401.

[148] S. Talebi-Moghaddam, T.A. Sipkens, K.J. Daun, Laser-induced incandescence on metal nanoparticles: validity of the Rayleigh approximation, Appl. Phys. B 125 (2019) 214.

[149] T.A. Sipkens, N.R. Singh, K.J. Daun, Time-resolved laser-induced incandescence characterization of metal nanoparticles, Appl. Phys. B 123 (2017).

[150] A.V. Eremin, E.V. Gurentsov, Sizing of Mo nanoparticles synthesised by Kr–F laser pulse photo-dissociation of Mo(CO)6, Appl. Phys. A 119 (2015) 615–622.

[151] B.F. Kock, C. Kayan, J. Knipping, H.R. Orthner, P. Roth, Comparison of LII and TEM sizing during synthesis of iron particle chains, Proc. Combust. Inst. 30 (2005) 1689–1697.

[152] J. Menser, K. Daun, T. Dreier, C. Schulz, Laser-induced incandescence from laser-heated silicon nanoparticles, Appl. Phys. B 122 (2016).

[153] T.A. Sipkens, R. Mansmann, K.J. Daun, N. Petermann, J.T. Titantah, M. Karttunen, H. Wiggers, T. Dreier, C. Schulz, In situ nanoparticle size measurements of gas-borne silicon nanoparticles by time-resolved laser-induced incandescence, Appl. Phys. B 116 (2014) 623–636.

[154] S. De Iuliis, F. Migliorini, R. Dondè, Laser-induced emission of TiO2 nanoparticles in flame spray synthesis, Appl. Phys. B 125 (2019) 219.

[155] F. Cignoli, C. Bellomunno, S. Maffi, G. Zizak, Laser-induced incandescence of titania nanoparticles synthesized in a flame, Appl. Phys. B 96 (2009) 593–599.

[156] R.L. Vander Wal, G.M. Berger, T.M. Ticich, P.D. Patel, Application of laser-induced incandescence to the detection of carbon nanotubes and carbon nanofibers, Appl. Opt. 41 (2002) 5678–5690.

[157] Y. Xu, Y. Ma, Y. Liu, S. Feng, D. He, P. Haghi-Ashtiani, A. Dichiara, L. Zimmer, J. Bai, Evolution of Nanoparticles in the Gas Phase during the Floating Chemical Vapor Deposition Synthesis of Carbon Nanotubes, J. Phys. Chem. C 122 (2018) 6437–6446.

[158] M. Cau, N. Dorval, B. Attal-Trétout, J.-L. Cochon, A. Foutel-Richard, A. Loiseau, V. Krüger, M. Tsurikov, C.D. Scott, Formation of carbon nanotubes: *In situ* optical analysis using laser-induced incandescence and laser-induced fluorescence, Phys. Rev. B 81 (2010) 165416.

[159] J.M. Mitrani, M.N. Shneider, Time-resolved laser-induced incandescence from multi-walled carbon nanotubes in air, Appl. Phys. Lett. 106 (2015) 043102.

[160] A.V. Eremin, E.V. Gurentsov, S.A. Musikhin, Temperature influence on the properties of carbon-encapsulated iron nanoparticles forming in pyrolysis of gaseous precursors, J. Alloys Compd. 727 (2017) 711–720.

[161] A.V. Eremin, E.V. Gurentsov, S.A. Musikhin, Diagnostics of carbon-encapsulated iron nanoparticles by laser heating, J. Phys. Conf. Ser. 946 (2018) 012068.

[162] R. Mansmann, T.A. Sipkens, J. Menser, K.J. Daun, T. Dreier, C. Schulz, Detector calibration and measurement issues in multi-color time-resolved laser-induced incandescence, Appl. Phys. B 125 (2019).

[163] J. Simonsson, N.-E. Olofsson, S. Török, P.-E. Bengtsson, H. Bladh, Wavelength dependence of extinction in sooting flat premixed flames in the visible and near-infrared regimes, Appl. Phys. B 119 (2015) 657–667.

[164] T.A. Sipkens, Advances in the Modeling of Time-Resolved Laser-Induced Incandescence. University of Waterloo, Waterloo, ON, Canada, 2018.

[165] F. Liu, K.J. Daun, D.R. Snelling, G.J. Smallwood, Heat conduction from a spherical nano-particle: status of modeling heat conduction in laser-induced incandescence, Appl. Phys. B 83 (2006) 355–382.

[166] T.A. Sipkens, P.J. Hadwin, S.J. Grauer, K.J. Daun, Predicting the heat of vaporization of iron at high temperatures using time-resolved laser-induced incandescence and Bayesian model selection, J. Appl. Phys. 123 (2018) 095103.

[167] H.A. Michelsen, F. Liu, B.F. Kock, H. Bladh, A. Boiarciuc, M. Charwath, T. Dreier, R. Hadef, M. Hofmann, J. Reimann, S. Will, P.-E. Bengtsson, H. Bockhorn, F. Foucher, K.-P. Geigle, C. Mounaïm-Rousselle, C. Schulz, R. Stirn, B. Tribalet, R. Suntz, Modeling laser-induced incandescence of soot: a summary and comparison of LII models, Appl. Phys. B 87 (2007) 503–521.

[168] H.A. Michelsen, Understanding and predicting the temporal response of laser-induced incandescence from carbonaceous particles, J. Chem. Phys. 118 (2003) 7012–7045.

[169] J.M. Mitrani, M.N. Shneider, B.C. Stratton, Y. Raitses, Modeling thermionic emission from laser-heated nanoparticles, Appl. Phys. Lett. 108 (2016) 054101.

[170] S. Talebi Moghaddam, K.J. Daun, Plasma emission during time-resolved laser-induced incandescence measurements of aerosolized metal nanoparticles, Appl. Phys. B 124 (2018).

[171] M.A. Dansson, M. Boisselle, M.A. Linne, H.A. Michelsen, Complications to optical measurements using a laser with an unstable resonator: a case study on laser-induced incandescence of soot, Appl. Opt. 46 (2007) 8095–8103.

[172] R. Mansmann, T. Dreier, C. Schulz, Performance of photomultipliers in the context of laser-induced incandescence, Appl. Opt. 56 (2017) 7849.

[173] R. Mansmann, T. Terheiden, P. Schmidt, J. Menser, T. Dreier, T. Endres, C. Schulz, LIISim: a modular signal processing toolbox for laser-induced incandescence measurements, Appl. Phys. B 124 (2018).

[174] P. Desgroux, X. Mercier, K.A. Thomson, Study of the formation of soot and its precursors in flames using optical diagnostics, Proc. Combust. Inst. 34 (2013) 1713–1738.

[175] S. Bejaoui, X. Mercier, P. Desgroux, E. Therssen, Laser induced fluorescence spectroscopy of aromatic species produced in atmospheric sooting flames using UV and visible excitation wavelengths, Combust. Flame 161 (2014) 2479–2491.

[176] F. Goulay, P.E. Schrader, L. Nemes, M.A. Dansson, H.A. Michelsen, Photochemical interferences for laser-induced incandescence of flame-generated soot, Proc. Combust. Inst. 32 (2009) 963–970.

[177] F. Goulay, L. Nemes, P.E. Schrader, H.A. Michelsen, Spontaneous emission from $C_2 (d^3\Pi_g)$ and $C_3 (A^1\Pi_u)$ during laser irradiation of soot particles, Mol. Phys. 108 (2010) 1013–1025.

[178] T.A. Sipkens, K.J. Daun, Defining regimes and analytical expressions for fluence curves in pulsed laser heating of aerosolized nanoparticles, Opt. Express 25 (2017) 5684.

[179] Q.-Y. Li, K. Xia, J. Zhang, Y. Zhang, Q. Li, K. Takahashi, X. Zhang, Measurement of specific heat and thermal conductivity of supported and suspended graphene by a comprehensive Raman optothermal method, Nanoscale 9 (2017) 10784–10793.

[180] F.J. Nelson, V.K. Kamineni, T. Zhang, E.S. Comfort, J.U. Lee, A.C. Diebold, Optical properties of large-area polycrystalline chemical vapor deposited graphene by spectroscopic ellipsometry, Appl. Phys. Lett. 97 (2010) 253110.

[181] A. Matković, A. Beltaos, M. Milićević, U. Ralević, B. Vasić, D. Jovanović, R. Gajić, Spectroscopic imaging ellipsometry and Fano resonance modeling of graphene, J. Appl. Phys. 112 (2012) 123523.

[182] B. Song, H. Gu, S. Zhu, H. Jiang, X. Chen, C. Zhang, S. Liu, Broadband optical properties of graphene and HOPG investigated by spectroscopic Mueller matrix ellipsometry, Appl. Surf. Sci. 439 (2018) 1079–1087.

[183] F. Liu, D.R. Snelling, K.A. Thomson, G.J. Smallwood, Estimate of scattering truncation in the cavity attenuated phase shift PM_{SSA} monitor using radiative transfer theory, Aerosol Sci. Technol. 52 (2018) 588–596.

[184] F. Liu, M. Yang, F.A. Hill, D.R. Snelling, G.J. Smallwood, Influence of polydisperse distributions of both primary particle and aggregate size on soot temperature in low-fluence LII, Appl. Phys. B 83 (2006) 383–395.

[185] K.J. Daun, G.J. Smallwood, F. Liu, Investigation of Thermal Accommodation Coefficients in Time-Resolved Laser-Induced Incandescence, J. Heat Transf. 130 (2008) 121201.

[186] K.J. Daun, G.J. Smallwood, F. Liu, Molecular dynamics simulations of translational thermal accommodation coefficients for time-resolved LII, Appl. Phys. B 94 (2009) 39–49.

[187] D.R. Snelling, F. Liu, G.J. Smallwood, Ö.L. Gülder, Determination of the soot absorption function and thermal accommodation coefficient using low-fluence LII in a laminar coflow ethylene diffusion flame, Combust. Flame 136 (2004) 180–190.

[188] L.E. Fried, W.M. Howard, Explicit Gibbs free energy equation of state applied to the carbon phase diagram, Phys. Rev. B 61 (2000) 8734–8743.

[189] S. Musikhin, R. Mansmann, G.J. Smallwood, T. Dreier, K.J. Daun, C. Schulz, Spectrally and temporally resolved LII interference emission in a laminar diffusion flame, Proc. Combust. Inst. Can. Sect. (2019).

[190] C.-F. López-Cámara, P. Fortugno, A. Muhammad, S. Musikhin, C. Prindler, H. Wiggers, T. Endres, N. Eaves, K.J. Daun, C. Schulz, Evolution of particle size and morphology in plasma synthesis of few-layer graphene and soot, Combust. Flame (submitted) (2022).

[191] H. Wang, Formation of nascent soot and other condensed-phase materials in flames, Proc. Combust. Inst. 33 (2011) 41–67.

[192] P. Kumar, P. Fennell, J. Symonds, R. Britter, Treatment of losses of ultrafine aerosol particles in long sampling tubes during ambient measurements, Atmos. Environ. 42 (2008) 8819–8826.

[193] E. Tatarova, A. Dias, J. Henriques, A.M. Botelho do Rego, A.M. Ferraria, M.V. Abrashev, C.C. Luhrs, J. Phillips, F.M. Dias, C.M. Ferreira, Microwave plasmas applied for the synthesis of free standing graphene sheets, J. Phys. Appl. Phys. 47 (2014) 385501.

[194] C. Tendero, C. Tixier, P. Tristant, J. Desmaison, P. Leprince, Atmospheric pressure plasmas: A review, Spectrochim. Acta Part B At. Spectrosc. 61 (2006) 2–30.

[195] N. Bundaleska, D. Tsyganov, A. Dias, E. Felizardo, J. Henriques, F.M. Dias, M. Abrashev, J. Kissovski, E. Tatarova, Microwave plasma enabled synthesis of free standing carbon nanostructures at atmospheric pressure conditions, Phys. Chem. Chem. Phys. 20 (2018) 13810–13824.

[196] E. Ranzi, A. Frassoldati, A. Stagni, M. Pelucci, A. Cuoci, T. Faravelli, Reduced Kinetic Schemes of Complex Reaction Systems: Fossil and Biomass-Derived Transportation Fuels, Int. J. Chem. Kinet. 46 (2014) 512–542.

[197] E. Tørneng, C.J. Nielsen, P. Klaeboe, H. Hopf, H. Priebe, The i.r., Raman and microwave spectra of 1-butene-3-yne (vinylacetylene) and 1-butene-3-yne-4d, Spectrochim. Acta Part Mol. Spectrosc. 36 (1980) 975–987.

[198] M. Jiménez, R. Rincón, A. Marinas, M.D. Calzada, Hydrogen production from ethanol decomposition by a microwave plasma: Influence of the plasma gas flow, Int. J. Hydrog. Energy 38 (2013) 8708–8719.

[199] I.E. Gordon, L.S. Rothman, C. Hill, R.V. Kochanov, Y. Tan, P.F. Bernath, M. Birk, V. Boudon, A. Campargue, K.V. Chance, B.J. Drouin, J.-M. Flaud, R.R. Gamache, J.T. Hodges, D. Jacquemart, V.I. Perevalov, A. Perrin, K.P. Shine, M.-A.H. Smith, J. Tennyson, G.C. Toon, H. Tran, V.G. Tyuterev, A. Barbe, A.G. Császár, V.M. Devi, T. Furtenbacher, J.J. Harrison, J.-M. Hartmann, A. Jolly, T.J. Johnson, T. Karman, I. Kleiner, A.A. Kyuberis, J. Loos, O.M. Lyulin, S.T. Massie, S.N. Mikhailenko, N. Moazzen-Ahmadi, H.S.P. Müller, O.V. Naumenko, A.V. Nikitin, O.L. Polyansky, M. Rey, M. Rotger, S.W. Sharpe, K. Sung, E. Starikova, S.A. Tashkun, J.V. Auwera, G. Wagner, J. Wilzewski, P. Wcisło, S. Yu, E.J. Zak, The HITRAN2016 molecular spectroscopic database, J. Quant. Spectrosc. Radiat. Transf. 203 (2017) 3–69.

[200] C.M. Western, PGOPHER: A program for simulating rotational, vibrational and electronic spectra, J. Quant. Spectrosc. Radiat. Transf. 186 (2017) 221–242.

[201] C.R. Shaddix, A new method to compute the radiant correction of bare-wire thermocouples (2017).

[202] M. Singh, A. Sengupta, K. Zeller, G. Skoptsov, R.L. Vander Wal, Effect of hydrogen concentration on graphene synthesis using microwave-driven plasma-mediated methane cracking, Carbon 143 (2019) 802–813.

[203] Johansson K. O., Head-Gordon M. P., Schrader P. E., Wilson K. R., Michelsen H. A., Resonance-stabilized hydrocarbon-radical chain reactions may explain soot inception and growth, Science 361 (2018) 997–1000.

[204] C. Wang, L. Sun, X. Dai, D. Li, X. Chen, W. Xia, W. Xia, Continuous synthesis of graphene nano-flakes by a magnetically rotating arc at atmospheric pressure, Carbon 148 (2019) 394–402.

[205] C. Wang, M. Song, X. Chen, D. Li, W. Xia, Synthesis of few-layer graphene flakes by magnetically rotating arc plasma: effects of input power and feedstock injection position, Appl. Phys. A 126 (2020) 210.

[206] X.K. Wang, X.W. Lin, M. Mesleh, M.F. Jarrold, V.P. Dravid, J.B. Ketterson, R.P.H. Chang, The effect of hydrogen on the formation of carbon nanotubes and fullerenes, J. Mater. Res. 10 (1995) 1977–1983.

[207] M. Snirer, V. Kudrle, J. Toman, O. Jašek, J. Jurmanová, Structure of microwave plasma-torch discharge during graphene synthesis from ethanol, Plasma Sources Sci. Technol. 30 (2021) 065020.

[208] H.A. Michelsen, A.V. Tivanski, M.K. Gilles, L.H. van Poppel, M.A. Dansson, P.R. Buseck, Particle formation from pulsed laser irradiation of soot aggregates studied with a scanning mobility particle sizer, a transmission electron microscope, and a scanning transmission x-ray microscope, Appl. Opt. 46 (2007) 959–977.

[209] J. Menser, Optical characterization of metallic nanoparticles: Light attenuation, laser-induced emission, data synthesis. University of Duisburg-Essen, Duisburg, Germany, 2019.

[210] X. Ma, M.R. Zachariah, C.D. Zangmeister, Crumpled Nanopaper from Graphene Oxide, Nano Lett. 12 (2012) 486–489.

[211] M. Becton, L. Zhang, X. Wang, Mechanics of graphyne crumpling, Phys Chem Chem Phys 16 (2014) 18233–18240.

[212] W.-N. Wang, Y. Jiang, P. Biswas, Evaporation-Induced Crumpling of Graphene Oxide Nanosheets in Aerosolized Droplets: Confinement Force Relationship, J. Phys. Chem. Lett. 3 (2012) 3228–3233.

[213] D.C. Collis, M.J. Williams, Two-dimensional convection from heated wires at low Reynolds numbers, J. Fluid Mech. 6 (1959) 357–384.

[214] Marcia Huber, Allan Harvey, Thermal Conductivity of Gases, CRC-Press, Boca Raton, FL, 2011.

[215] R.B. Stewart, R.T. Jacobsen, Thermodynamic Properties of Argon from the Triple Point to 1200 K with Pressures to 1000 MPa, J. Phys. Chem. Ref. Data 18 (1989) 639–798.

[216] E. Tognoni, G. Cristoforetti, S. Legnaioli, V. Palleschi, A. Salvetti, M. Mueller, U. Panne, I. Gornushkin, A numerical study of expected accuracy and precision in Calibration-Free Laser-Induced Breakdown Spectroscopy in the assumption of ideal analytical plasma, Spectrochim. Acta Part B At. Spectrosc. 62 (2007) 1287–1302.

[217] N. Ohno, M.A. Razzak, H. Ukai, S. Takamura, Y. Uesugi, Validity of Electron Temperature Measurement by Using Boltzmann Plot Method in Radio Frequency Inductive Discharge in the Atmospheric Pressure Range, Plasma Fusion Res. 1 (2006) 028–028.